SINGLE CRYSTAL RAMAN SPECTROSCOPY OF SELECTED ARSENITE, ANTIMONITE AND HYDROXYANTIMONATE MINERALS

Silmarilly Bahfenne

B.App.Sci (Chem.)

Chemistry Discipline

This thesis is submitted as part of the assessment requirements of Master of Applied Science Degree at QUT

February 2011

KEYWORDS

Raman, infrared, IR, spectroscopy, synthesis, synthetic, natural, X-ray diffraction, XRD, scanning electron microscopy, SEM, arsenite, antimonate, hydroxyantimonate, hydrated antimonate, minerals, crystal, point group, factor group, symmetry, leiteite, schafarzikite, apuanite, trippkeite, paulmooreite, finnemanite.

ABSTRACT

This thesis concentrates on the characterisation of selected arsenite, antimonite, and hydroxyantimonate minerals based on their vibrational spectra. A number of natural arsenite and antimonite minerals were studied by single crystal Raman spectroscopy in order to determine the contribution of bridging and terminal oxygen atoms to the vibrational spectra. A series of natural hydrated antimonate minerals was also compared and contrasted using single crystal Raman spectroscopy to determine the contribution of the isolated antimonate ion.

The single crystal data allows each band in the spectrum to be assigned to a symmetry species. The contribution of bridging and terminal oxygen atoms in the case of the arsenite and antimonite minerals was determined by factor group analysis, the results of which are correlated with the observed symmetry species.

In certain cases, synthetic analogues of a mineral and/or synthetic compounds isostructural or related to the mineral of interest were also prepared. These synthetic compounds are studied by non-oriented Raman spectroscopy to further aid band assignments of the minerals of interest. Other characterisation techniques include IR spectroscopy, SEM and XRD.

From the single crystal data, it was found that good separation between different symmetry species is observed for the minerals studied.

TABLE OF CONTENTS

LIST OF FIGURES

LIST OF TABLES

LIST OF APPENDICES

LIST OF PUBLICATIONS

The following is a list of publications written in relation to material covered in this body of work:

Cejka, J., **Bahfenne, S.**, Frost, R. L. and Sejkora J. (2010) Raman spectroscopic study of the arsenite mineral vajdakite $[(Mo^{6+}O_2)_2(H_2O)_2As^{3+}{}_2O_5]\cdot 6H_2O$. J. Raman Spectrosc., IF: 3.147, 41(1): 74 – 77

Bahfenne, S. and Frost, R. L. (2010) A Review of the Vibrational Spectroscopic Studies of Arsenite, Antimonite, and Antimonate Minerals. App. Spec. Rev. IF: 3.243, 45(2): 101 – 129

Bahfenne, S., Rintoul, L. and Frost, R. L. (2010) Single-crystal Raman spectroscopy of natural leiteite ($ZnAs_2O_4$) and comparison with the synthesised mineral. J. Raman Spectrosc., published online 20 Jul.
DOI: 10.1002/jrs.2751

Frost, R. L., Cejka, J., Sejkora, J., Ozdin, D., **Bahfenne, S.** and Keeffe, E. C. (2009) Raman spectroscopic study of the antimonate mineral brandholzite $Mg[Sb_2(OH)_{12}]\cdot 6H_2O$. J. Raman Spectrosc. IF: 3.147, 40(12): 1907 – 1910

Frost, R. L. and **Bahfenne, S.** (2010) Raman spectroscopic study of the arsenite minerals leiteite $ZnAs_2O_4$, reinerite $Zn_3(AsO_3)_2$ and cafarsite $Ca_5(Ti,Fe,Mn)_7(AsO_3)_{12}]\cdot 4H_2O$. J. Raman Spectrosc. IF: 3.147, 41(3): 325 – 328

Rintoul, L., **Bahfenne, S**. and Frost, R. L. (2010) Single-crystal Raman spectroscopy of brandholzite $Mg[Sb(OH)_6]_2\bullet 6H_2O$ and bottinoite $Ni[Sb(OH)_6]_2\bullet 6H_2O$ and the polycrystalline Raman spectrum of mopungite $Na[Sb(OH)_6]$. J. Raman Spectrosc., published online 27 Sep.
DOI: 10.1002/jrs.2804

STATEMENT OF ORIGINALITY

The work contained in this thesis has not been previously submitted to meet requirements for any award at this or any other higher education institution. To the best of my knowledge and belief, the thesis contains no material previously published or written by another person except where due reference is made

Signed .... *Date* / /

Silmarilly Bahfenne

ACKNOWLEDGMENTS

I would like to take this opportunity to thank the following people

- *My principal supervisor Prof. Ray Frost for the opportunity to undertake my degree and the positive words*
- *Dr. Llew Rintoul for teaching me almost everything I know about Raman, and for patiently going through factor group analysis repeatedly*
- *The financial and infrastructure support of the Queensland University of Technology, Inorganic Materials Research Program is gratefully acknowledged. The Australian Research Council (ARC) is thanked for funding the instrumentation*
- *My parents for putting me through undergrad and supporting me always, and my brother Falouthy*
- *Dr. Wayde Martens for your encouragement and much valued advice*
- *Mr. Tony Raftery for your help with XRD*
- *Long time friend Mr. Tri Nguyen for Friday lunches and helping with XRD sample prep*
- *Dr. Peter Hines for your help with SEM*
- *Fellow post-grads and office mates Jean, Vanita, Blain and Elle and lab mates Matt, Ashley, James and Henry for your stories, advice and lessons*
- *My dear Mohsin, for believing in me always.*
- *And finally all my lecturers, friends, and anyone else who has ever taught me anything, thank you!*

This thesis is dedicated to my

parents Nurdiah & Fachri

Chapter 1

Introduction

and

Literature Review

1.1 INTRODUCTION

Arsenic and antimony are found throughout the earth's crust as a variety of minerals, although not particularly abundant. It has been estimated that there are 2 grams of arsenic and 0.2 grams of antimony in every tonne of crustal rocks [1]. Many arsenic-bearing minerals associated with sulfides have been identified, such as arsenopyrite FeAsS, orpiment As_2S_3, and realgar α-As_4S_4. When these ores are oxidised, As_2O_3 is obtained as a by-product. Antimony also occurs with sulfur, Sb_2S_3 being the principal source. Many oxides have also been identified; valentinite Sb_2O_3 and cervantite $Sb^{3+}Sb^{5+}O_4$. Similar to As_2O_3, Sb_2O_3 is obtained during oxidation of sulfide ores [1–3].

A significant number of literature reports the synthesis of arsenite [4-10] and antimonite compounds [11-15], but few works on their vibrational spectroscopy are published. The majority of vibrational spectroscopic studies concentrate on the arsenite and antimonite species present in aqueous solutions [16-22]. In solution the cations are found in ortho, pyro, or meta configurations with the oxygen atoms [17]. These configurations also apply to salts. In ortho salts the cation is found in an isolated configuration with three oxygen atoms forming a $[XO_3]^{3-}$ group. When two such groups are connected through a common bridging oxygen, a dimer or $[X_2O_5]^{4-}$ group is formed which is a constituent of pyro salts. When an infinite number of $[XO_3]^{3-}$groups are connected, a meta salt is formed. Each of these groups appears in arsenite minerals e.g. reinerite $Zn_3(AsO_3)_2$ [23] and finnemanite $Pb_5(AsO_3)_3Cl$ [24] have ortho groups, pyro groups are found in paulmooreite $Pb_2As_2O_5$ [25] and vajdakite $[(MoO_2)_2(H_2O)_2(As_2O_5)]\bullet(H_2O)$ [26], and leiteite $ZnAs_2O_4$ [27] and trippkeite $CuAs_2O_4$ [28] possess meta groups. However to date naturally occurring antimonite minerals have been found to possess only the meta group, as exemplified by schafarzikite $FeSb_2O_4$ [29] and apuanite $Fe^{2+}Fe_4^{3+}Sb_4O_{12}S$ [29].

On the other hand a great number of vibrational spectroscopic studies on antimonate compounds have been published, mainly concerning synthetic anhydrous antimonates with rutile [30], trirutile [31,32], ilmenite [33,34], and pyrochlore structures [35]. All anhydrous antimonates contain $[SbO_6]_n^{n-}$ octahedra sharing edges to form a polymer. Hydrated antimonate minerals, however, show no polymerisation between the $[Sb(OH)_6]^-$ octahedra. The hydrated antimonate minerals had been studied mainly with infrared spectroscopy [36,37], with no Raman spectroscopic studies to date.

1.2 GENERAL DESCRIPTION OF COMMON MINERALS

1.2.1 Arsenic Trioxide

Arsenic trioxide is the most important compound of arsenic. When dissolved in neutral or acidic solutions it forms unstable arsenious acid, whose formula had been subject to much debate and is discussed later [1]. Salts are categorised into ortho-, pyro-, and meta-arsenious acids or H_3AsO_3, $H_4As_2O_5$, and $HAsO_2$ [3]. The alkali arsenites are soluble in water; those of alkaline earth metals are less soluble and those of heavy metals are insoluble [1].

The structure of arsenic trioxide consists of As_4O_6 units in the solid, liquid, and vapour forms below 800°C, whereas vapour at 1800°C consists of As_2O_3 molecules [2]. Arsenic trioxide crystallises either as arsenolite (cubic) or claudetite (monoclinic) which dissolve slowly in water [38]. X ray analysis showed arsenolite having a molecular lattice of As_4O_6 units forming a structure that has been described as an adamantanoid cage (Fig. 1.1) [39].

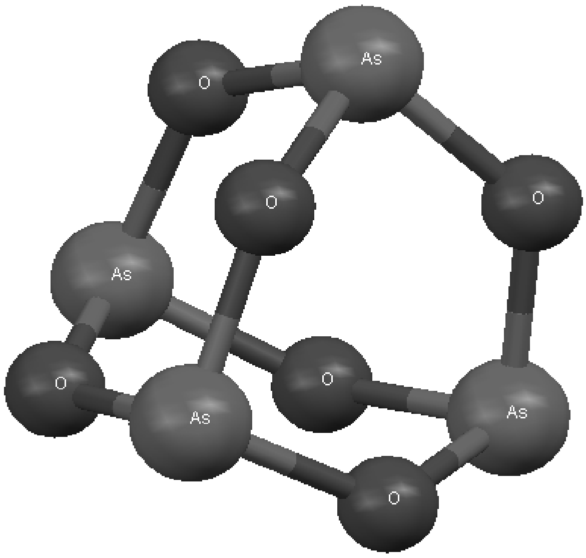

Fig. 1.1 – As_4O_6 units in arsenolite

Claudetite possesses alternating As and O atoms linked into sheets (Fig. 1.2) [2]. Claudetite is the thermodynamically stable form but conversion of arsenolite to claudetite is slow. Conversion tends to be faster in the presence of heat or higher pH. Water also catalyses the conversion; it is thought that As-O bonds are protonated. It has been shown that the conversion from arsenolite to claudetite occurs at 125°C and greater [40]. It was thought that claudetite is less stable than arsenolite at temperatures below 50°C, however a more recent solubility study showed claudetite to be less soluble and therefore more stable than arsenolite at temperatures up to 250°C [19]. The glassy form of As_2O_3 has a similar structure to claudetite, but its macromolecular structure is less regular [2].

1.2.2 Antimony Trioxide

Antimony trioxide exists as two crystalline forms which are insoluble in water, dilute nitric acid, and dilute sulfuric acid but soluble in hydrochloric and organic acids and alkali solutions. Salts can theoretically be categorised into ortho-, pyro-, and meta-antimonious acids or H_3SbO_3, $H_4Sb_2O_5$, and $HSbO_2$, although only the first form had been isolated [3].

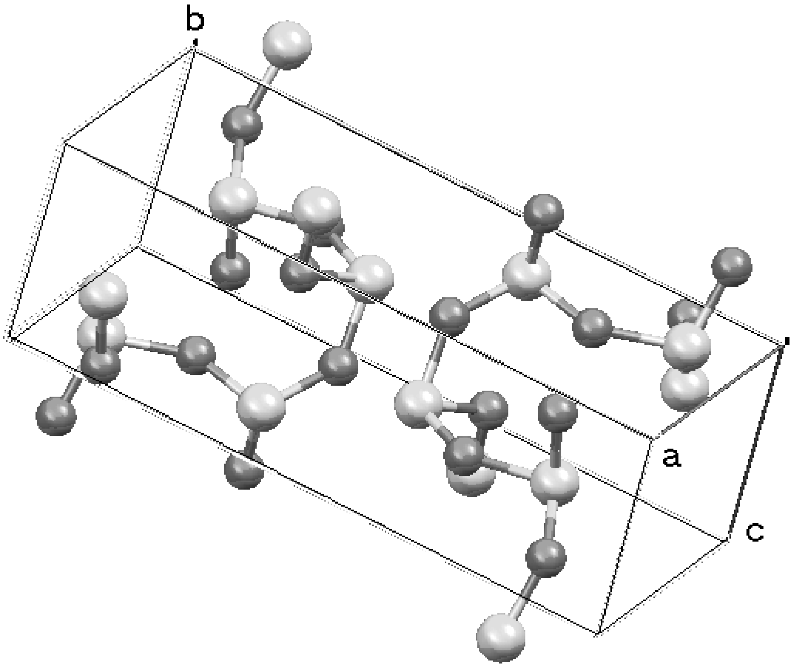

Fig. 1.2 – Structure of claudetite. Light atoms are As, dark atoms are O

The cubic senarmontite is stable at temperatures up to 517° C whereas the orthorhombic valentinite exists at higher temperatures [2]. Senarmontite consists of molecular units of Sb_4O_6 isostructural to arsenolite (Fig. 1.1).

Valentinite consists of long double chains of SbO_3, where each Sb atom is connected to three O atoms, one of which bridges two Sb atoms forming a polymeric chain $[Sb_2O_3]_n$ (Fig. 1.3) [38]. The alternate Sb and O atoms are linked into bands [2]. Senarmontite slowly converts to valentinite upon heating.

1.2.3 Antimony Pentoxide

Antimony pentoxide is almost insoluble in water but soluble in concentrated HCl [1–3]. Salts are poorly characterised but are categorised into hydrated and anhydrous salts, both of which do not have the SbO_3^{4-} anion in their structure [38]. Theoretically antimonic acids could be categorised, based on the different types of arsenic acids, into H_3SbO_4 (ortho), $H_4Sb_2O_7$ (pyro), or $HSbO_3$ (meta-antimonic acid) [3]. The alkali metal salts have very low solubility.

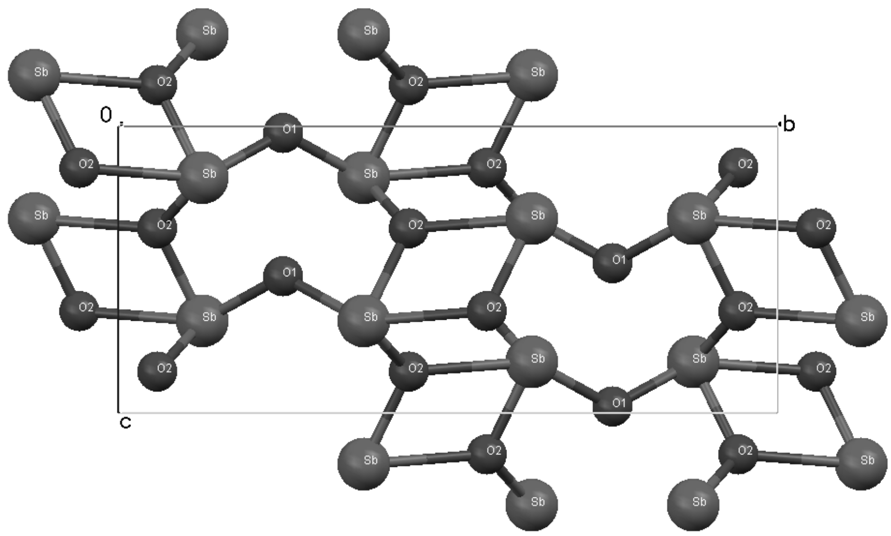

Fig. 1.3 – Structure of valentinite

1.3 STRUCTURAL STUDIES OF MINERALS

A list of all arsenite, antimonite, and hydroxyantimonate minerals that have been discovered thus far may be found in Appendix 1.

As mentioned previously in ortho salts the cation is found in an isolated configuration with three oxygen atoms forming a $[XO_3]^{3-}$ group where X=As or Sb. When two such groups are connected through a common bridging oxygen, a dimer or $[X_2O_5]^{4-}$ group is formed which is a constituent of pyro salts. When an infinite number of $[XO_3]^{3-}$groups are connected (Fig. 1.4), a meta salt is formed of which $NaAsO_2$ is an example [41].

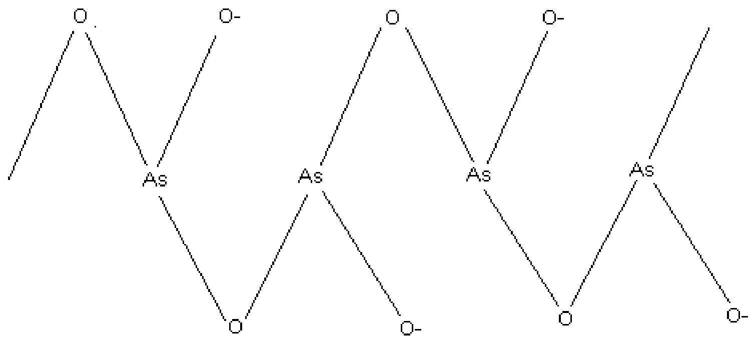

Fig. 1.4 – AsO_3 polymeric chain

1.3.1 Arsenite

The arsenite group $[AsO_3]^{3-}$ is found in a pyramidal geometry due to the stereochemically active lone pair on the As atom [42]. The anion can be found isolated or polymerised in a mineral structure. Reinerite $Zn_3(AsO_3)_3$ [23] and finnemanite $Pb_5(AsO_3)_3Cl$ have the anion isolated whereas arsenites polymerised via their vertices can be found in paulmooreite $Pb_2As_2O_5$ [25] and ludlockite $PbFe_4(As_5O_{11})_2$. As mentioned above the synthetic $NaAsO_2$ has the anions linked in a polymeric manner. The polymerisation of the arsenite group resulting in an infinite chain of $[AsO_2]_n^{n-}$ is termed a catena-arsenite chain [42]. This chain is also found in the minerals trippkeite $CuAs_2O_4$ [28] and leiteite $ZnAs_2O_4$ [27], and in the synthetic $Pb(AsO_2)Cl$ and $Pb_2(AsO_2)_3Cl$ [5].

1.3.2 Antimonite

The typical building block of antimonite minerals is the corner-sharing Sb^{3+} tetrahedra in a trigonal pyramid configuration (three corners occupied by O and the lone pair as the fourth ligand) [29]. Schafarzikite $Fe^{2+}Sb_2^{3+}O_4$ possess columns of edge-sharing Fe^{2+} octahedra parallel to the chains of Sb^{3+} tetrahedra. In versiliaite $Fe_2Fe_4Sb_6O_{16}S$ the schafarzikite type structure is preserved except for the substitution of every fourth tetrahedral Sb by Fe^{3+}. Apuanite $Fe^{2+}Fe_4^{3+}Sb_4^{3+}O_{12}S$ can also be derived from the crystal structure of schafarzikite by substituting every third tetrahedral Sb^{3+} by Fe^{3+}. The same Sb coordination is found in senarmontite (cubic Sb_2O_3), Sb_4O_5Cl, valentinite (orthorhombic Sb_2O_3), and derbylite $(Fe,Fe,Ti)_7SbO_{13}(OH)$.

1.3.3 Hydroxyantimonate

A common feature of all hydroxyantimonate minerals is the isolated $[Sb(OH)_6]^-$ anion [2]. Hydrated antimonates include mopungite $NaSb(OH)_6$ and brandholzite $Mg[Sb(OH)_6]_2{\bullet}6H_2O$. The structure of mopungite comprises hydrogen bonded layers of $[Sb(OH)_6]^-$ octahedra linked within the layer by Na^+ ions [43]. Whereas brandholzite-like structures consist of two different alternating layers stacked along the *c* axis; one contains only the $[Sb(OH)_6]^-$ octahedra, the other contains both $[M(H_2O)_6]^{2+}$ and $[Sb(OH)_6]^-$ octahedra in a ratio of 2:1. The $[Sb(OH)_6]^-$ hydroxyls form external hydrogen bonds that bind the layers together and the aqua ligands of the $[Mg(H_2O)_6]^{2+}$ form both inter and intra layer hydrogen bonds [44].

1.4 VIBRATIONAL SPECTROSCOPY

An attempt at building a database of Raman spectra of minerals was published in 1994 [45]. It relied on the existence of the totally symmetric vibrational mode which is usually observed as the strongest band in the characteristic spectral region. This mode corresponds to the most covalentic chemical bond of the anionic unit. It categorised the minerals into several groups, one of which included minerals having a $(XO_3)^{n-}$ unit such as carbonates and arsenites. The inclusion of arsenite minerals in this category must be examined carefully. The existence of a polymeric chain of AsO_3 in some minerals means that the vibrating unit is not isolated and may not vibrate like one would expect a $(XO_3)^{n-}$ unit possessing a C_{3V} free symmetry. Another category included minerals having a polymer of units in which corner O atoms are shared. Therefore two totally symmetric bands are expected; one corresponding to bonds belonging to non-bridging O atoms, and the other to bridging O atoms. The wavenumber of the latter is usually lower than the former. The relative intensities of the two bands vary depending on the ratio of non-bridging O to bridging O atoms. Some arsenite minerals such as leiteite may be better suited to fall under this category.

1.4.1 Arsenic Trioxide

Arsenic trioxide may take the form of arsenolite (cubic As_4O_6) or claudetite (monoclinic As_2O_3). Factor group analysis of an isolated As_4O_6 molecule shows: $\Gamma_{vib} = 2A_1$ (Raman) + $2E$ (Raman) + $2T_1$ (inactive) + $4T_2$ (Raman and IR). Many studies have reported IR and Raman spectra of arsenolite (As_4O_6) in its solid, hydrated, and gas phases [16-18]. A theoretical study has also been published [18,39]. A summary of the spectral results may be found in Appendix 2. Band assignments vary between authors.

Szymanski et al. [16] wrote that the vibrations of solid As_4O_6 can be described as those of the AsO_3 pyramid and two vibrations of the As_4O_6 tetrahedron as a whole. Band assignment for As_4O_6 was based on that of P_4O_6 since they both possess a T_d point symmetry, whereas the band assignment for AsO_3 was based on the SeO_3^{2-} ion, since mass of Se is very similar to that of As and SeO_3^{2-} and AsO_3 have C_{3v} symmetry. IR bands at 845 and 800 cm^{-1} (Raman at 830 and 785 cm^{-1}) were assigned to As-O antisymmetric and symmetric stretches respectively. The IR inactive symmetric breathing vibration of the As_4O_6 tetrahedron was observed in the Raman spectrum at 555 cm^{-1}. Bands at 475, 375, and 275 cm^{-1} were assigned to the deformation mode of the AsO_3 pyramid (first two) and deformation of As_4O_6 tetrahedron respectively. Although no assignment was made, Loehr and Plane reported similar Raman bands for solid As_4O_6 at 782, 561, 473, 372, 269, and 240 cm^{-1} [17].

Lezal and Konak [46] have reported IR bands corresponding to various As-O-As vibrations at 258, 346, 482 (strong), and 808 cm^{-1} (very strong), and is supported by calculated values [18,39]. The above bands agree with those observed by Szymanski et al. [16]. Assignment of the bands is as follows; 808 and 482 cm^{-1} are As-O-As stretches, 346 cm^{-1} is the As-O-As bend, and 258 cm^{-1} is the As-O-As wag [39].

Beattie et al. [47] has reported a gas-phase Raman spectrum of As_4O_6, which has the same 'cage' structure in the vapour phase. Bands at 492 (weak) and 556 cm^{-1} (very strong) are assigned to symmetric As-O-As stretch, and the symmetric As-O stretch is found at 381 cm^{-1} (very strong). These values are in close agreement to calculated ones [18,39]. The Raman spectrum of powder As_4O_6 shows signals at almost the same wavenumbers (370, 470, and 560 cm^{-1}). In a different theoretical study [39], the GaussView visualisation program was used to determine the predominant type of motion (As-O-As stretch, bend, or wag). In this study bands observed by Beattie at 556, 492, and 409 cm^{-1} are assigned to As-O-As stretches, and bands at 381 and 184 cm^{-1} are assigned to As-O-As bends. Other gas-phase and solid Raman spectra [48–50] agree with results reported by Beattie et al. [47].

Claudetite, the monoclinic modification of As_2O_3, has been studied by infrared and polarised Raman spectroscopy [51,52]. Factor group analysis determines that there should be $13A_g + 14B_g + 14A_u + 13B_u$ modes. The Raman spectrum is characterized by a very strong A_g band at 460 cm^{-1}.

Comparison of Raman and infrared spectra shows the presence of 'Davydov doublets', where a band in the infrared spectrum is found in close proximity to each Raman frequency as a result of weak interlayer coupling. Bands in the region of 600 – 900 cm^{-1} were assigned to the antisymmetric stretches of AsO_3, those in the region 500 – 600 cm^{-1} to symmetric stretches, and those in the region 300 – 500 cm^{-1} to symmetric deformations [52].

1.4.2 Raman Investigation into Arsenite Speciation in Aqueous Solutions

The solubility of As_4O_6 is known to increase by addition of a base. Loehr and Plane prepared solutions containing varying compositions of OH^- and As^{3+} ($[As^{3+}] + [OH^-] = 8.0M$, and ratio $R = [OH^-] / [As^{3+}]$ ranged from 3.5 to 15) and recorded their Raman spectra [17]. The study concluded that there are at least three As^{3+} species each of which gives rise to its own Raman spectrum.

Identification of the various forms of arsenious acid were based on selecting related series of bands which retain the same intensity relative to each other with varying experimental conditions.

$As(OH)_3$ gives rise to bands at 710 (polarised) and 655 cm^{-1} (depolarised) indicating its symmetric and antisymmetric As-(OH) stretches respectively. These bands were observed in solutions saturated with As_4O_6 (pH = 0 – 4) and in solutions where the ratio $[OH^-]/[As^{3+}] = 3.5$. In in D_2O solution these bands shift by about 20 cm^{-1} corresponding to As-OD stretches, confirming the assignment of the bands at 710 and 655 cm^{-1} to As-OH stretches.

$AsO(OH)_2^-$ is formed as more base is added according to the reaction $As(OH)_3 + OH^- \rightarrow AsO(OH)^{2-} + H_2O$. Bands corresponding to this species are observed in solutions where the ratio $[OH^-]/[As^{3+}] = 4$. As-O stretch is assigned to a band at 790 cm^{-1}, while symmetric and antisymmetric stretches of As-OH to 570 and 610 cm^{-1} respectively. The 790 cm^{-1} band did not shift in position in D_2O solution while the bands around 600 cm^{-1} did. This species, possessing a mirror plane, belongs to C_s symmetry and hence would give six Raman-active bands. Only two out of three bending modes were observed, at 320 and 370 cm^{-1}.

AsO_3^{3-} appeared in solutions with high ratios of $[OH^-]/[As^{3+}] \approx 15$. A polarised band 752 cm^{-1} is assigned to As-O symmetric stretch whereas the depolarised band 680 cm^{-1} is assigned to the antisymmetric stretch. A bending mode at 340 cm^{-1} was also observed.

$AsO_2(OH)^{2-}$ is also thought to exist as a product of stepwise dissociation of $As(OH)_3$ in solutions where $[OH^-]/[As^{3+}] \approx 6$. Since it has C_s symmetry, the antisymmetric As-O stretch is expected to occur at a higher wavenumber than the symmetric stretch. The symmetric As-O stretch is expected to appear midway between the observed positions of $AsO(OH)_2^-$ and AsO_3^{3-} (790 and 752 cm^{-1} respectively) and the antisymmetric around 800 cm^{-1}. The expected positions match the observed intensities in this region.

A theoretical study calculated structures, stabilities and the vibrational spectra of $As(OH)_3$ and its anions in solution, and of the oligomers [18]. The programs GAMESS and GAUSSIAN94 were implemented to obtain IR frequency and intensities, and Raman wavenumbers. The calculated stretching wavenumbers of $As(OH)_3$ agree with the experimental values determined by Loehr and Plane [17] while some calculated wavenumbers of $AsO(OH)_2^-$, $AsO_2(OH)^{2-}$, and AsO_3^{3-} do not agree closely with experimental values.

A later study [16], which utilised methods thought to improve accuracy of electron correlation and incorporation of anharmonic and hydration effects semiquantitatively, found that $AsO(OH)_2^-$ can be better modelled in terms of the ion pair $AsO(OH)_2^- \ldots Na^+$. The calculated frequencies for this ion pair are 836, 606, and 530 cm^{-1} which are in better agreement with experimental wavenumbers of 790, 610, and 570 cm^{-1}. This indicates that ion-pairing may be important for the formation of $AsO(OH)_2^-$. The new calculated wavenumbers for $AsO_2(OH)^{2-}$ and AsO_3^{3-} still do not agree closely with experimental data. The authors noted that it is difficult to apply their technique to anions with larger charges because the hydration and counterion effects are expected to be much larger, and because the experimental data are less certain.

Another Raman study [20] of the speciation of arsenite in aqueous solution confirmed the results obtained by Loehr and Plane [17]. A diagram constructed using data from an earlier study [53] showing the distribution of arsenite species as a function of pH at 25°C and 1 bar is also included which allows the confirmation of the species present at a certain pH. Broad bands near 600 and 800 cm^{-1} corresponding to $AsO_2(OH)^{2-}$ and AsO_3^{3-} are observed at pH = 13.2. At pH = 12.6 the above bands become narrower indicating the dominance of $AsO_2(OH)^{2-}$, the disappearance of the lower wavenumber shoulder of the 800 cm^{-1} band indicates the absence of 750 cm^{-1} band corresponding to AsO_3^{3-}. Spectra at pH = 10.5 show an intense band at 790 cm^{-1} and therefore $AsO(OH)_2^-$ to be most dominant. A small proportion of $As(OH)_3$ is also present at this pH visible by the weak band at 700 cm^{-1}. At pH = 8.5 and lower, the dominant species is $As(OH)_3$ seen by a strong band at 700 cm^{-1} with a shoulder at 650 cm^{-1} and the less dominant species is $AsO(OH)_2^-$. The arsenite species determined to be present at a given pH based on the spectra agree closely with the diagram.

1.4.3 Existence of Polymeric Species in Aqueous Solutions

Loehr and Plane [17] also conducted an investigation into the existence of polymeric As^{3+} but detected no spectral changes with dilution and up to 80°C. A more recent study by Gout et al. showed that at 275°C, pH ≤ 6, and As concentration up to 1 mol/kg, the symmetric stretch of $As(OH)_3$ at 700 cm^{-1} shifts by 5 – 10 cm^{-1} and the antisymmetric stretch at 650 cm^{-1} broadens slightly due to weakening of hydrogen bonds with increasing temperature [21]. Over 1M, additional bands appear at about 520 and 380 cm^{-1} which increase in intensity with increasing As concentration and temperature. These bands are assigned to the formation of As-O-As bonds, because these bands are also observed in amorphous and molten As_2O_3

which are both known to possess As-O-As chains. The 380 cm^{-1} band is assigned to the symmetrical vibration of As_4O_6 tetrahedron because it was also observed in gas-phase and powder spectra of As_4O_6 in a separate study by Beattie et al. [47]. A theoretical study [39], however, assigns this band to As-O-As bend.

A number of As hydroxide and oxide oligomers' structures are envisaged and their normal modes are calculated [18]. The energy differences for various polymerisation reactions were also calculated. The condensation of $3As(OH)_3$ is shown to give $As_3O_3(OH)_3$ and $3H_2O$, is favoured entropically and will become more favourable with increasing temperature. For $As_3O_3(OH)_3$ bands are calculated at 378, 437, 512, and 665 cm^{-1}. The broad band centred at 520cm^{-1} (which probably constitutes several bands including one near 437cm^{-1}) observed at high temperatures by Gout et al. [21] is thus assigned to $As_3O_3(OH)_3$ symmetric bridging O stretch, whereas the band at 665cm^{-1} corresponds to symmetric As-OH stretch (which seems to occur around 650 – 700 cm^{-1} in both monomers and all oligomers according to the calculations). This study noted that bands near 370 cm^{-1} (such as that observed by Pokrovski et al. [22]) is probably characteristic of oligomers mainly involving symmetric As motion but highlighted that it does not correspond to As_4O_6; because the broad band around 700cm^{-1} indicates that the oligomeric species possesses As-OH groups. It seems that $As_3O_3(OH)_3$ is the most probable oligomeric species in solution. The calculated and experimental vibrational frequencies of $As_3O_3(OH)_3$ are summarised in Table 1.1.

$As_3O_3(OH)_3$		Assignment
Experimental	**Calculated**	
~ 680	665	Symmetric As-OH stretch
520 (broad, from ~ 400 – 600cm^{-1})	512	Symmetric bridging As-O-As stretch
	437	
380	378	Symmetric stretches mainly involving As

Table 1.1 – Comparison of experimental and calculated Raman wavenumbers of $As_3O_3(OH)_3$ and their assignment

Raman spectra of aqueous arsenic solutions of varying concentration and temperature were recorded [21]. At low concentrations ($0.02 \leq m_{As} \leq 0.33$ mol/kg), 20° C, and at pH 0 – 8 the spectra appear the same; polarised sharp band at 700 cm^{-1} and depolarised shoulder at 650 cm^{-1} very similar to those observed by Loehr and Plane [17]. At pH > 8 $AsO(OH)_2^-$ appears as seen by new bands appearing at 600 and 790 cm^{-1}. Neutral arsenic solutions at low and medium (~0.5 mol/kg) concentrations were also studied under varying temperatures up to 275°C. Both bands only shift by about 5 cm^{-1} towards the lower wavenumber as temperatures increase indicating that only the monomer $As(OH)_3$ dominates. At higher concentrations (1 mol/kg) the sharp band starts to broaden and split into two bands at 696 and 669 cm^{-1} at

275°C, which is thought to have been caused by the formation of a dimeric hydrated arsenic species which consists of two $As(OH)_3$ molecules held together by hydrogen bonding. The splitting increases as concentration increases to 2 mol/kg at temperatures 175 – 275°C. A new polarised band is observed at 525 cm^{-1}. At even higher concentrations (4.1 and 5.2 mol/kg) this new band increases in intensity with increasing concentrations and temperature. Similar behaviour is observed in a polarised band at 380 cm^{-1} which started to appear at 4.1 mol/kg. The band at 525 cm^{-1} is similar to that observed in fused (at 275°C) and amorphous (at 20°C) arsenic oxide so it was assigned to the As-O-As bond. Possible polymeric species envisaged by the author with the aid of molecular dynamic calculations include a dehydrated dimer $As_2O(OH)_4$, $As_3O_6(OH)_3$, $As_6O_6(OH)_6$, and As_4O_6. The presence of the 380 cm^{-1} band in highly concentrated As solutions is similar to that observed in arsenolite and gas-phase As_4O_6 but not claudetite so it probably indicates the formation of As_4O_6 and corresponds to As-O-As bend as described by Jensen et al. [39].

1.4.4 Vibrational Spectroscopy of Arsenite Minerals

A single crystal of cafarsite, $Ca_8(Ti, Fe, Mn)_{6-7}(AsO_3)_{12}•4H_2O$, has been analysed using polarised Raman spectroscopy and the results compared with other metal oxides to achieve assignment of bands [54]. It is of cubic symmetry of space group *P*n3. The As atoms are at the apices of a trigonal pyramidal coordination but the pyramids are not connected to each other. There are two different Fe and Ca atoms. Polarised and cross-polarised spectra of the 001, 100, 010, and 111 faces were obtained and the spectra were identical. For symmetric pyramidal shapes four fundamental frequencies are expected which consist of a degenerate stretch and a degenerate deformation. The study compared vibrations of the AsO_3 of cafarsite to those of AsF_3 and noted that differences in band positions between the two are mainly due to the state in which the spectra were obtained (AsF_3 was in liquid state) and the difference of atomic weight between O and F. The authors wrote that bands of AsF_3 (274, 343, 644, and 715 cm^{-1}) are similar to those of AsO_3 (258, 319, 721, and 763 cm^{-1}), keeping in mind that the 763 and 319 cm^{-1} bands should be completely polarised.

1.4.5 Antimony Trioxide

Antimony trioxide may take the form of senarmontite (cubic Sb_4O_6) or valentinite (orthorhombic Sb_2O_3). Factor group analysis of an isolated Sb_4O_6 molecule shows: $\Gamma_{vib} = 2A_1$ (Raman) + $2E$ (Raman) + $2T_1$ (inactive) + $4T_2$ (Raman and IR). Sb_4O_6 also possesses the cage unit. Beattie et al. [47] reported Raman bands for powdered senarmontite at 87 (medium), 121 (weak – medium), 193 (medium – strong), 256 (very strong), 359 (very weak), 376 (weak – medium), 452 (medium), 717 cm^{-1} (weak). The author noted that there were large frequency differences between Sb_4O_6 and As_4O_6 fundamentals, which indicate a considerable force-field change between the two.

Senarmontite showed Raman bands at 84, 124, 197, 261 (most intense), 364, 381, 458, and 722 cm^{-1} whereas valentinite, orthorhombic Sb_2O_3, had peaks at 71, 103, 140 (most intense), 194, 223, 269, 294, 449, 502, 602, 690 cm^{-1} [55]. The same study also reported the Raman spectrum of Sb_2O_3 glass to be almost identical with that of valentinite except that the lattice mode bands (under 400 cm^{-1}) are lost, indicating that the polymeric Sb-O chains are found in the melt as well. The above band positions were supported by later studies [56–57].

IR of senarmontite showed bands at 675 (shoulder), 740, and 960 cm^{-1} (weak) and valentinite at 455, 488 (shoulder), 540, 585 (shoulder), and 740 cm^{-1} [56]. The senarmontite band at 960 cm^{-1} was later shown to be unrelated to the ideal structure of the compound [57].

The IR spectrum of gaseous Sb_4O_6 has also been studied [58] and found that peak positions differ to those observed by Beattie et al. [47] for Sb_4O_6 powder. Bands were observed at 785, 415, 292, and 175 cm^{-1}. The results agree more closely with those observed for senarmontite suspended in Nujol mulls in a study by Sourisseau and Mercier [59] at 744, 395, 272, and 179 cm^{-1}.

A study reported the calculated IR and Raman frequencies for senarmontite, Sb_4O_6, along with band assignments [60]. Stretches of Sb-O-Sb were found around 250 – 300 cm^{-1} (Raman), 350 cm^{-1} (Raman), 709 – 765 cm^{-1} (Raman and IR), 360 – 380 cm^{-1} (Raman and IR), Sb-O-Sb bends at 450 cm^{-1} (Raman), 135 cm^{-1} (Raman), 170 – 197 cm^{-1} (Raman and IR), and Sb-O-Sb wag at 290 – 350 cm^{-1} (Raman and IR).

Quantum chemical simulation of both cubic and orthorhombic Sb_2O_3 had been performed using the GAMESS package at the density functional theory level with the B2LYP exchange-correlation potential [57]. Good agreement is observed between calculated and experimental data. The author concluded that the 750 – 300 cm^{-1} region corresponds to the region of stretching vibration occurring in the chain plane, while the region below 300 cm^{-1} corresponds to deformation vibrations directed at angle to the chain plane.

For senarmontite, symmetric stretches of Sb-O-Sb were found at 460 (Raman and IR), 385 - 409 (Raman and IR), and 741 cm^{-1} (IR), while the antisymmetric stretches were found at 367 – 394 cm^{-1} (Raman) and 574 cm^{-1} (IR). Its deformations lie at 282 (IR), 280 (Raman), 179 (Raman and IR), 126 (Raman), and 109 cm^{-1} (Raman). For valentinite, there are two distinct bridging O atoms. Symmetric stretches of Sb-$O_{(1)}$-Sb are found at 344 and 311 cm^{-1} (IR) and Sb-$O_{(2)}$-Sb at 519 – 489 (Raman and IR) and 460 – 450 (Raman and IR) cm^{-1}. Antisymmetric stretches of $O_{(1)}$ are observed at 672 (IR), 663 cm^{-1} (Raman and IR), and those of O_2 at 600 – 550 (Raman and IR), 560 – 501 (IR) cm^{-1}. Bands from 316 – 200 cm^{-1} were determined to be a combination of scissoring, wagging, and twisting, of which are observed only in the Raman spectra with the exception of the twisting modes. Bands under ~160 cm^{-1} are assigned to lattice vibrations. A summary of the above bands are tabulated in Appendix 3.

1.4.6 Raman Investigations of Antimony Speciation in Aqueous Solutions

$Sb(OH)_3$ is found to be the main species responsible for Sb transport under moderately acidic to near neutral conditions while $Sb(OH)_4^-$ is predominant over pH 10 in sulfide-poor solutions. In sulfide-rich, near neutral to alkaline solutions thioantimony species may be important for Sb transport. However $Sb(OH)_3$ is primarily responsible for hydrothermal transport of Sb especially at temperatures above 200 – 250°C even in sulfide-rich systems [61]. The solubility of Sb^{3+} and Sb^{5+} increases with solution acidity [62]. Sb_2O_3 is dissolved as $Sb(OH)_3$ and $Sb(OH)_2^+$ [63] while Sb_2O_5 dissolves as $HSb(OH)_6$ and $Sb(OH)_6^-$.

1.4.7 Vibrational Spectroscopy of Antimonite Mineral

Band assignment from the work of Gilliam et al. [60] was applied to a Raman and IR spectroscopic study of schafarzikite $Fe^{2+}Sb_2^{3+}O_4$ [64]. Bands around 700 (strong) and 252 cm^{-1} (weak – medium) were assigned to Sb-O-Sb stretch (the latter may also correspond to Fe-O-Fe bend), around 610 (weak – medium) – 670 (very strong) and 405 (weak) – 467 cm^{-1} (weak) to Fe-O-Fe stretch. A band at 497 cm^{-1} (strong) was assigned to Sb-O-Fe stretch or $Sb-O_t$. Sb-O-Sb bends are found at 295 (strong) – 405 cm^{-1} (weak) and 161 – 217 cm^{-1} (medium – strong).

1.5 SYNTHETIC ARSENITES

1.5.1 Preparation of Arsenites

Alkali metal arsenites such as $NaAsO_2$, $KAsO_2$, and $RbAsO_2$ have been synthesised by solid state reaction using a 1:1 mixture of the elemental alkali metal and As_2O_3 under Ar gas [4]. It is heated to 500° C at a rate of 50° C/hour and then cooled afterwards at a rate of 5°C/hour to room temperature. $Cs_3As_5O_9$ was synthesised in a similar fashion except a cooling rate of 25°C/hour was used. Terminal As-O bond was found to be shorter than bridging As-O bond in the above compounds. The bond angles of O_t-As-O_b are around about 4°C greater than those of O_b-As-O_b.

Other synthetic minerals that have been prepared include $Pb(AsO_2)Cl$, $Pb_2(AsO_2)_3Cl$, and $Pb_2As_2O_5$ [5]. $Pb(AsO_2)Cl$ was prepared by mixing As_2O_3 and $PbCl_2$ in a ratio of 1:2 in a teflon-coated vessel which was filled with a 1M acetic acid solution. It was heated to a temperature ranging from 300 to 500 K and left to react for 10 days. The same procedure was implemented to prepare $Pb_2(AsO_2)_3Cl$ except that a mixture of PbO and $PbCl_2$ in a 10:1 weight % ratio was used instead of pure $PbCl_2$. The result was $Pb_2(AsO_2)_3Cl$ and $Pb_2As_2O_5$ in a weight ratio of 1:50. Unfortunately no spectroscopy was performed on the synthetic samples.

Pertlik [7] has previously prepared $CuAs_2O_4$ or trippkeite by hydrothermal route. As_2O_3 and CuO are placed in an autoclave (mole ratio 1:1, total mass 0.5 g) along with the solvent which could be CH_3COOH or H_2O. If CH_3COOH is used the temperature range should be 200 – 250°C, but other products are formed at this temperature including Cu and Cu_2O. If H_2O is used trippkeite forms above 100°C and no other product would form below about 200°C. In either case the reaction is left for 48 hours. The product is then mixed with 500mL H_2O and placed on a water bath at a temperature of 60° C and left for two hours to get rid of all water-dissolvable compounds.

Zinc meta-arsenite was also prepared by Curtin [8] and also in another study by Avery [9]. A solution of $NaAsO_2$, made from As_2O_3 and NaOH, is reacted with a solution of $ZnCl_2$, to which a few drops of glacial acetic acid is added, to cause the precipitation of $Zn(AsO_2)_2$.

1.5.2 Vibrational Spectroscopy of Synthetic Arsenite

The Raman spectra from the study by Emmerling and Röhr [4] were not presented in detail, only mentioning the bands at the highest wavenumber; 836 cm^{-1} for $KAsO_2$, 832 cm^{-1} for $RbAsO_2$, and 836 cm^{-1} for $Cs_3As_5O_9$ which can be assigned to the stretching of terminal As-O. These bands lie above those assigned to the stretch of the bridging As-O.

1.6 SYNTHETIC ANTIMONITES

1.6.1 Preparation of Antimonites

Hirschle and Röhr [11] has prepared alkali metal oxoantimonites of the structures $ASbO_2$ where A = K or Rb, and $A_4Sb_2O_5$ where A = K, Rb or Cs by reduction of Sb_2O_5, or of Sb_2O_3 and Sb_2O_5 with the alkali metal in a corundum crucible under Ar atmosphere at 500 – 600°C and afterwards cooled at a rate of 5°C/hour. $KSbO_2$ was synthesised through conversion of elemental Sb with KO_2, while $RbSbO_2$ obtained through stoichiometric mixture of Rb, Sb_2O_3, and Sb_2O_5. $A_4Sb_2O_5$ is obtained by a stoichiometric mixture of Sb_2O_5 and the alkali metal.

Uranyl antimonite $UO_2Sb_2O_4$ [14] has been prepared from the hydrothermal reaction of UO_3 with Sb_2O_3 and KCl in a ratio of 1:1:2. The autoclave used has a 23 mL capacity, the volume of water that was added to the solids was 4 mL. The autoclave was sealed, placed in a box furnace and heated to 180° C and held for 89 hours, after which the furnace was cooled at 9°C/hour to 23°C. The mother liquor is decanted from the products, which were then washed with water then methanol and dried. Even though neither K^+ nor Cl^- ions are present in the product, it is thought that Cl^- acts as a mineraliser agent that aids in solubilising the UO_3 and in recrystallising the product. KCl can be substituted with CsCl.

$MnSb_2O_4$ was prepared via hydrothermal synthesis [15] using stoichiometric mixtures of MnO and Sb_2O_3 in 5% HF solution. The reaction was carried out at 500°C and 1000 bars. The crystals are clear green in colour in the form of irregular needles.

1.6.2 Vibrational Spectroscopy of Synthetic Antimonites

Summarised in Table 1.2 are the results of Hirschle and Röhr [11]. The author notes that around 650 cm^{-1} a band will appear in compounds which have the ‘open’ Sb-O-Sb group, whereas a band around 614 cm^{-1} appears in the spectra of all compounds possessing the Sb-O-Sb group.

$KSbO_2$ and $RbSbO_2$ crystallises isotypically as $CsSbO_2$. The characteristic building block of the structure is the trigonal SbO_4 bipyramids, which are connected by their edges to form infinite chains.

$A_4Sb_2O_5$ where A = K, Rb, or Cs has the $[O_2Sb\text{-}O\text{-}Sb\text{-}O_2]^{4-}$ anion as building block, formed by two SbO_3 tetrahedra linked by a common bridging O. The K and Rb compounds have different conformations to the Cs compound.

The Raman and IR spectra of $MnSb_2O_4$ and $NiSb_2O_4$ have been published and the results can be found in Appendix 4 [15]. Few differences were observed above 300 cm^{-1} and it was concluded that the cations play only a weak role in this region. The authors assigned Raman bands at 670 and 620 cm^{-1} to Sb-O bonds.

1.7 SYNTHETIC HYDROXYANTIMONATES

1.7.1 Preparation of Hydroxyantimonates

A number of hydroxyantimonate compounds have been synthesized, including $Li[Sb(OH)_6]$, $Na[Sb(OH)_6]$, $Ag[Sb(OH)_6]$, $Mg[Sb(OH)_6]_2.6H_2O$, $Ni[Sb(OH)_6]_2.6H_2O$, $Co[Sb(OH)_6]_2.6H_2O$, and $Ba[Sb(OH)_6]_2.6H_2O$ [43,44,36,65]. The $Sb(OH)_6$ source, commonly an aqueous solution of $K[Sb(OH)_6]$, is mixed with an aqueous solution of the corresponding salt e.g. LiCl [65], NaCl [43], $AgNO_3$ [65], MgCl and $CoSO_4.7H_2O$ [44]. In the case of $Mg[Sb(OH)_6]_2.6H_2O$ and $Co[Sb(OH)_6]_2.6H_2O$ an immediate amorphous precipitate is usually acquired, then single crystals are obtained with slow evaporation at room temperature [44].

$KSbO_2$	**$RbSbO_2$**	**$K_4Sb_2O_5$**	**$Rb_4Sb_2O_5$**	**$Cs_4Sb_2O_5$**
		757 (weak)	748 (weak)	741 (weak)
		718 (medium)	707 (medium)	700 (strong)
		655 (weak)	646 (medium)	646 (strong)
612 (strong)	614 (strong)		613 (medium)	614 (weak)
581 (medium)	580 (weak)			
		372 (medium)	358 (medium)	
				305 (medium)
		263 (very strong)		
233 (weak)	231 (weak)		238 (medium)	
211 (weak)				
185 (weak)	184 (weak)	~180 (weak)		198 (weak)

Table 1.2 – Raman band positions for Synthetic Antimonites

1.7.2 Vibrational Spectroscopy of Synthetic Hydroxyantimonates

Siebert [34] first analysed synthetic $Na[Sb(OH)_6]$ by infrared spectroscopy. Bands under 1000 cm^{-1} were assigned to Sb-O stretch, 1000 – 1200 cm^{-1} to Sb-OH bend, 2100 – 2350 cm^{-1} to the second overtone of Sb-OH bend, and 3220 – 3400 cm^{-1} to Sb-OH stretch and H_2O stretch.

Balicheva and Roi [37], and Franck [36] has also published the infrared spectra of $Na[Sb(OH)_6]$ along with other synthetic hydroxyantimonates. No Raman study, however, had been attempted on any of the compounds.

The band assignment of $Na[Sb(OH)_6]$ made by Balicheva and Roi [37] differed from those made by Siebert [34], in that not all bands below 1000 cm^{-1} are assigned to Sb-O stretches. Instead the Sb-O stretches are assigned to bands in the 600 – 550 cm^{-1} region. Bands in the 800 – 690 cm^{-1} region which were previously assigned to Sb-O stretches were assigned to the out-of-plane deformation of the OH groups. Franck [36] was able to obtain infrared spectra of the hydroxyantimonates below 400 cm^{-1}. The assignments given by Franck agreed with those given by Balicheva and Roi, with the addition that the Sb-O bends were also characterized at 350, 287, and 230 cm^{-1}.

1.8 PROJECT AIMS

This work aims to enrich the Raman spectroscopic knowledge of arsenite, antimonite, and hydroxyantimonate ions in their mineral form. The purpose of the first part of this research is to investigate how polymerisation of arsenite and antimonite groups affects their vibrational spectra. The second part aims to investigate the vibrational spectra of hydrated antimonate minerals to ascertain the hydroxyantimonate ion contribution. Techniques employed include Raman spectroscopy, using both oriented and non-oriented crystals, infrared (IR) spectroscopy, scanning electron microscopy

(SEM), and powder x-ray diffraction (XRD). DFT calculations are employed to aid band assignments where possible.

The specific aims of this research are:

- Acquire the single crystal Raman spectra of the following arsenite and antimonite minerals: finnemanite $Pb_5(AsO_3)_3Cl$, paulmooreite $Pb_2As_2O_5$, leiteite $PbAs_2O_4$, schafarzikite $FeSb_2O_4$ and trippkeite $CuAs_2O_4$, and explain the differences in the spectra in terms of the configuration of the arsenite or antimonite group.
- Acquire the single crystal Raman spectra of the following hydrated antimonate minerals: brandholzite $Mg[Sb(OH)_6]_2.6H_2O$ and bottinoite $Ni[Sb(OH)_6]_2.6H_2O$, and determine the contribution of the hydroxyantimonate ion
- Acquire non-oriented Raman spectra of synthetic or natural specimens required to aid band assignments of the above minerals. These specimens include synthetic $PbAs_2O_4$, $Pb_2(AsO_2)_3Cl$, and $ZnSb_2O_4$ and natural apuanite $Fe^{2+}Fe_4^{3+}Sb_4O_{12}S$ and mopungite $Na[Sb(OH)_6]$.

Chapter 2

Experimental Methods

2.1 INTRODUCTION

This chapter will outline the instrumental details, synthetic procedures, and spectral manipulation techniques utilised in this project. Techniques employed include Raman spectroscopy, using both oriented and non-oriented crystals, infrared (IR) spectroscopy, scanning electron microscopy (SEM), and powder x-ray diffraction (XRD). Synthetic minerals were prepared by hydrothermal reaction or wet chemistry techniques.

2.2 SYNTHETIC PROCEDURES

Although it is desired to obtain natural specimens on which to perform experiments, the rarity of many minerals of interest required the synthesis of these minerals. The synthesis of a compound isostructural and homologous to the studied mineral could also be of interest, since it may be useful to investigate a series of specimens in that they may aid in determining the contribution of a specific moiety in the vibrational spectra. The synthetic procedures employed in this study are mainly wet chemistry and hydrothermal techniques. Some literature reports the synthesis of some arsenite and antimonite compounds by solid state reaction [4,10-11] but this method was avoided due to the requirement of grinding the reactants, which would pose inhalation hazards, and/or heating in inert atmosphere.

2.2.1 Wet Chemistry Method

The first step in synthesising arsenite and antimonite salts using wet chemistry methods is to create an alkali solution using X_2O_3 (X=As or Sb) and commonly NaOH. The molar ratio depends on whether the desired product is an ortho, pyro, or meta salt. The formation and composition of different alkali arsenites, obtained from the reaction between As_2O_3 and NaOH in the ratios 1:2, 1:4 and 1:6, have been studied from pH and conductivity measurements [66]. The following equations show the reaction that occurs in each case.

$2NaOH + X_2O_3 \rightarrow 2NaXO_2 + H_2O$ (meta)

$4NaOH + X_2O_3 \rightarrow Na_4X_2O_5 + 2H_2O$ (pyro)

$6NaOH + X_2O_3 \rightarrow 2Na_3XO_3 + 3H_2O$ (ortho)

The second step is to create a second solution containing a soluble metal salt, which is then mixed with the first solution to give a precipitate of the desired mineral. The product, still in its mother liquor, is usually aged or hydrothermally treated in order to increase crystal growth.

2.2.2 Hydrothermal Method

The hydrothermal method has proved useful in synthesis of some arsenite and antimonite compounds [5,7,14,15]. It also has an advantage over wet chemistry in that it may result in bigger and more crystalline products. In this project hydrothermal reactions were carried out in Teflon liners, of about 110ml capacity, placed in steel autoclaves which are then heated in ovens. This method required, in most cases, a series of reactions to be performed using different solvents, fill factor, temperature and length of reaction in order to find experimental conditions which yield the purest product.

2.3 INSTRUMENTAL TECHNIQUES

The technique vital to this study is Raman microscopy. The 1 micron spatial resolution proved useful for examination of geological samples which are often inhomogeneous and allows spectra to be collected on a single crystal. Its non-destructive nature and little sample preparation are also advantageous. Supporting techniques include IR spectroscopy, SEM, and powder XRD.

Infrared spectroscopy is a technique complementary to Raman spectroscopy; it allows the acquisition of spectra containing modes that are not Raman active. Although it is wise to utilise both Raman and IR, the limited quantity of most of the minerals studied limits the use of IR spectroscopy. However it lends itself nicely to the analysis of minerals with a layered structure as this allows the determination of the degree of interlayer coupling.

SEM is used to obtain micrographs of the specimen, both natural and synthetic, and to perform microprobe analysis mainly on synthetic samples. XRD is used mainly to identify the phases present in a synthetic product. In this study natural samples are rarely analysed using XRD due to the limited quantity of the sample and the destructive nature of sample preparation. The proportion of phases present in a sample may also be ascertained using Rietveld refinement.

2.3.1 Raman Microscopy

The instrument used was a Renishaw 1000 Raman microscope system, which also includes a monochromator, a Rayleigh filter system and a CCD detector coupled to an Olympus BHSM microscope equipped with 10x, and 50x objectives. The Raman spectra were excited by a Spectra-Physics model 127 He-Ne laser producing plane polarised light at 633 nm and collected at a resolution of better than 4 cm^{-1} and a precision of ± 1 cm^{-1} in the range between 120 and 4000 cm^{-1}. Repeated acquisitions on the crystals using the highest magnification (50x) were accumulated to improve the signal-to-noise ratio in the spectra. The instrument was calibrated prior to use using the 520.5 cm^{-1} line of a silicon wafer.

There are two possible measuring schemes in Raman microscopy; polarised and non-polarised. Non-polarised measurements may be performed on poly- or monocrystals, require no orientation of the sample, and give spectra containing all Raman active modes possible. Polarised measurements require orientation of the monocrystal with respect to the incident beam, and a polaroid analyser placed before the detector. Since polarisability tensors differ between crystal axes, spectra obtained in such measurements give only those modes that are active in the specific orientation. This method allows bands to be assigned to the corresponding symmetry species.

The crystal studied may be oriented by placing it on the corner of a perfect cube, aligning it parallel to the sides of the cube using a very fine needle. The rotation of the cube through 90° about the X, Y, Z axes of the laboratory frame allowed the determination of the three crystallographic axes. The Raman spectra of the oriented single crystals are reported in accordance with the Porto notation: the propagation directions of the incident and scattered light and their polarisations are described in terms of the crystallographic axes *a*, *b* and *c*. The notation may, for example read CABC. Here the first C is the direction of the incident light, A is the direction of the polarisation of the electric vector of the incident light, B is the orientation of the analyser and the second C is the direction of the propagation of the scattered light.

2.3.2 Infrared Spectroscopy

Infrared spectra were obtained using a Nicolet Nexus 870 FTIR spectrometer. Spectra over the range 4000 to 550 cm^{-1} were obtained using the KBr beam splitter by the co-addition of 64 scans with a resolution of 2 cm^{-1} and a mirror velocity of 0.6329 cms^{-1}. Far infrared spectra were collected using the same spectrometer equipped with a polyethylene beam splitter replacing the KBr beam splitter. Samples (2 mg) were ground and intimately mixed with CsI (200 mg), followed by pressing it into a tablet at a pressure of 10 tonnes.

2.3.3 Scanning Electron Microscopy

Scanning electron microscope (SEM) photos were obtained on a FEI QUANTA 200 Environmental Scanning Electron Microscope operating at high vacuum and 15 kV. This system is equipped with an Energy Dispersive X-ray spectrometer with a thin Be window capable of analysing all elements of the periodic table down to carbon. For the analysis a counting time of 100 s was applied.

2.3.4 X-Ray Diffraction

XRD analyses were carried out on a Philips wide-angle PW 1050/25 vertical goniometer (Bragg Brentano geometry) applying CuKα radiation (λ = 1.54 Ǻ, 40 kV, 40 mA). The samples were measured in step scan mode with steps of 0.02° 2θ and a scan speed of 1.00° per minute from 2 to 75° 2θ.

2.4 SPECTRAL MANIPULATION

Spectral manipulation such as baseline correction/adjustment was performed using the GRAMS software package (Galactic Industries Corporation, NH, USA). Band component analysis was undertaken using the Jandel 'Peakfit' software package that enabled the type of fitting function to be selected and allows specific parameters to be fixed or varied accordingly. Band fitting was done using a Lorentzian-Gaussian cross-product function with the minimum number of component bands used for the fitting process. The Gaussian-Lorentzian ratio was maintained at values greater than 0.7 and fitting was undertaken until reproducible results were obtained with squared correlations of R^2 greater than 0.995.

Chapter 3

Single Crystal Raman Spectroscopy of Natural Finnemanite $Pb_5(AsO_3)_3Cl$ from Långban, Sweden

3.1 INTRODUCTION

The single crystal Raman spectra of natural finnemanite are presented. Finnemanite $Pb_5(AsO_3)_3Cl$ is an ortho arsenite mineral containing isolated AsO_3 pyramids belonging to the hexagonal space group $P6_3/m$ (C_{6h}^2), a = 10.322 and c = 7.055 Å, Z = 2 [24]. Other ortho arsenite minerals include reinerite $Zn_3(AsO_3)_2$ [23], cafarsite $Ca_8(Ti,Fe,Fe,Mn)_{6-7}(AsO_3)_{12}.4H_2O$ [54], and nealite $Pb_4Fe(AsO_3)_2Cl_4.2H_2O$ [67,68]. The finnemanite crystal used in this investigation was black and opaque, originating from the Långban locality, Sweden and was kindly supplied by the Swedish Museum of Natural History (specimen number NRM883736).

To aid in determining the AsO_3 ion contribution in the finnemanite spectrum, the Raman spectrum of the isolated $[AsO_3]^{3-}$ ion was calculated by density field theory (DFT) and was compared to the spectrum of natural finnemanite. Since there was insufficient quantity of natural finnemanite on which to perform powder XRD, its spectrum was also compared to that of pure synthetic finnemanite to ensure its purity. Additionally, the spectra of the above ortho arsenite minerals, synthetic $Pb_2(AsO_2)_3Cl$ and $PbAs_2O_4$, and $Pb_2As_2O_5$ (paulmooreite) were recorded and compared to finnemanite .

Finnemanite may be considered as an O-deficient mimetite structure ($Pb_5(AsO_4)_3Cl$), where a site that is normally occupied by O in mimetite is left vacant in finnemanite to balance the reduction of As^{5+} to As^{3+} [69]. No Raman study had been published on finnemanite, although the Raman spectra of lead apatite minerals including mimetite have been published [70,71].

3.2 EXPERIMENTAL

3.2.1 Minerals

Single crystals of finnemanite and paulmooreite were supplied by the Swedish Museum of Natural History of specimen numbers NRM883736 and NRM532109 respectively. The specimens originated from the Långban locality, Filipstad district, Värmland province, Sweden. Nealite and cafarsite were supplied by the Mineralogical Research Company and originated from Laurium, Greece and Piedmont, Italy, respectively.

3.2.2 Synthetic Procedures

Baikie et al. [69] reported a low temperature procedure for synthesis of finnemanite which was implemented in this study. A mixture containing 6.255 g (0.02778 mol) PbO, 1.6434 g (0.00833 mol) As_2O_3, and 5.56 mL (0.00556 mol) 1 M HCl (mole ratio of 10:3:2) in 50 mL deionised H_2O was stirred at 50°C for 24 hours. The mixture was initially bright yellow in colour which turned paler as the reaction progressed. The resulting grey slurry was filtered, washed with methanol, and dried at 70°C for 2 hours.

Reinerite was prepared by mixing a solution containing As_2O_3 (0.0319 mol) and NaOH (0.1916 mol) in 100 mL deionised H_2O with a solution containing $ZnSO_4.7H_2O$ (0.0958 mol) in 50 mL deionised H_2O. The product appeared as a white powder.

For details of the preparation of $Pb_2(AsO_2)_3Cl$ and $PbAs_2O_4$, please refer to Sections 4.2.2 and 4.4.1.

3.2.3 Raman Microscopy

A crystal of finnemanite was selected and placed on the corner of a perfect cube, aligned parallel to the sides of the cube using a very fine needle. In the plane of the crystal, the long axis corresponded to the *c* axis, and the *a* and *b* axis are not readily identifiable in the specimen under study. Fortunately it is not necessary to separate *a* from *b* in order to classify the modes according to their symmetry. In this case the *a* and *b* axes are arbitrarily assigned.

3.2.4 DFT Calculations

Calculations were performed using the Gaussian 03 program [72] and the GaussView 4.0 (Gaussian, Inc.,Wallingford, CT) front end, running on an SGI Origin 3000 supercomputer. The wavenumbers of the fundamental modes were calculated using density field theory (DFT) with B3-LYP method and a 6-31G(d) basis set. A scaling factor of 0.972 was applied to account for anharmonicity which is not incorporated into DFT calculations resulting in overestimation of the vibrational frequencies. Raman intensities were calculated from the Gaussian activities based on 633 nm excitation.

3.3 DESCRIPTION OF CRYSTAL STRUCTURE

Finnemanite is hexagonal with the space group $P6_3/m$ (C_{6h}^2) and two formula units per unit cell. The crystal cell dimensions are a = 10.322 and c

= 7.055 Å [24]. The structural building blocks include isolated AsO_3 pyramids, $Pb_{(1)}$-O and $Pb_{(2)}$-O-Cl polyhedra (Fig. 3.1). Each $Pb_{(1)}$ is connected to 3 $O_{(1)}$ and 3 $O_{(2)}$; two $Pb_{(1)}$ atoms share the same $O_{(1)}$ atoms forming $Pb_{(2)}(O_{(1)})_3(O_{(2)})_6$ groups. Each $Pb_{(2)}$ is connected to 1 $O_{(1)}$, 4 $O_{(2)}$, and 2 Cl. The O atoms form a distorted tetragonal pyramid around $Pb_{(2)}$. The symmetry of the AsO_3 pyramids is reduced to C_s from the ideal trigonal pyramid (C_{3v}) symmetry. The As atom is connected to 1 $O_{(1)}$ and 2 $O_{(2)}$, the lengths of which are 1.86 and 1.74 Å respectively.

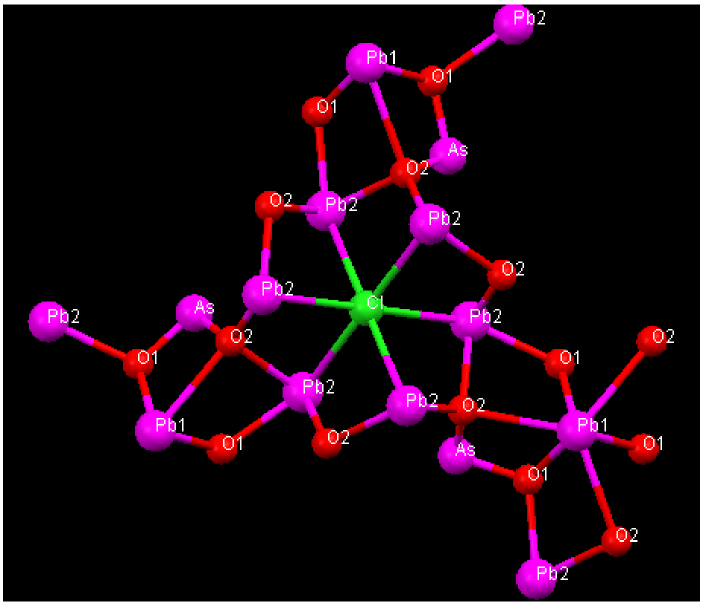

Fig. 3.1 – Model of the structure of finnemanite

3.4 RESULTS

3.4.1 X-ray Diffraction

The synthetic grey powder was subjected to X-ray powder diffraction. The powder pattern of the product showed an excellent correlation with that of finnemanite, with no impurities. There was an insufficient amount of the natural sample to perform XRD (Fig. 3.2).

The white powder resulting from the reinerite synthesis was found to consist of pure reinerite $Zn_3(AsO_3)_2$ (Fig. 3.3).

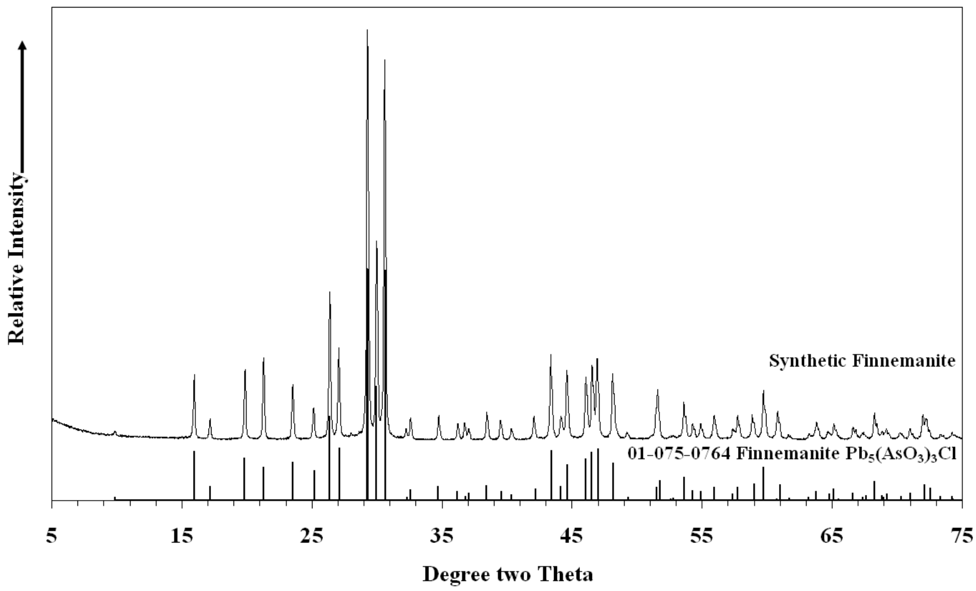

Fig. 3.2 – XRD pattern of synthetic finnemanite

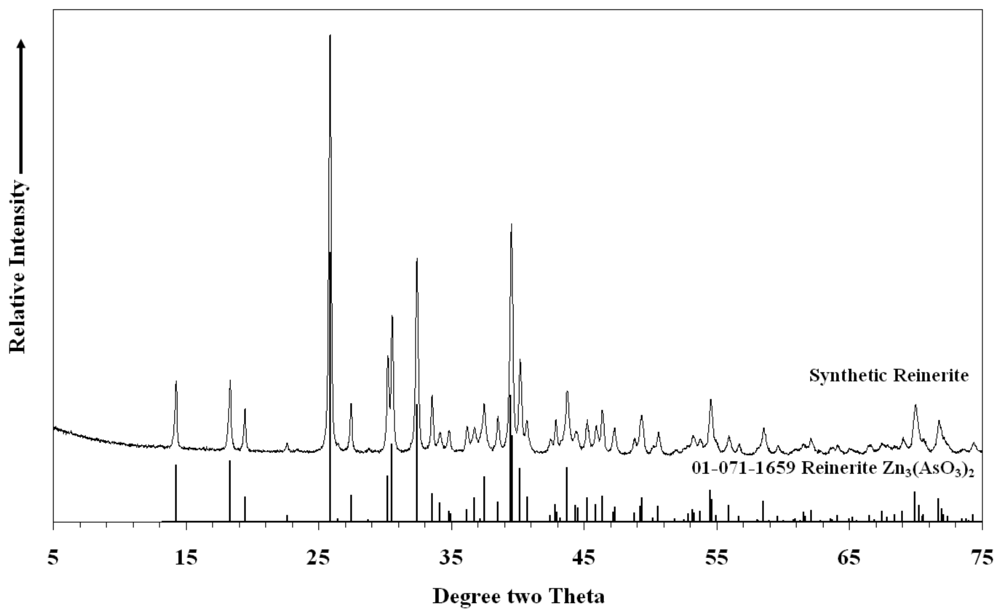

Fig. 3.3 – XRD pattern of synthetic reinerite

3.4.2 Raman Microscopy

3.4.2.1 *Factor Group Analysis*

The unit cell of finnemanite is the primitive unit cell and it contains two formula units. Thus a primitive unit cell contains 36 atoms. The number of allowable modes is 105 consisting of $10A_g + 8B_g$ (IA) + $7A_u + 10B_u$ (IA) + $7E_{1g} + 11E_{2g} + 10E_{1u} + 7E_{2u}$ (IA) (IA = inactive). The form of the polarisability tensor for C_{6h} crystals dictates that A_g modes are observed in *aa*, *bb*, and *cc* orientations, E_{1g} in *ac* and *bc*, E_{2g} in *aa*, *ab*, and *bb*.

The isolated $[AsO_3]^{3-}$ pyramid has 6 normal modes of vibration consisting of $2A_1$ and $2E$. On a *C*s site each A_1 mode transforms to *A*', and each *E* mode splits to *A*' and *A*''. Correlating this to a C_{6h} crystal splits each *A*' mode to A_g, E_{2g}, B_u, and E_{1u}, and each *A*'' mode to B_g, E_{1g}, A_u, and E_{2u}. The splitting pattern is summarised in Table 3.1.

C_{3v}	C_s	C_{6h}
$2A_1$ (υ_1, υ_2)	$2A'$	$2A_g + 2E_{2g} + 2B_u + 2E_{1u}$
$2E$ (υ_3, υ_4)	$2A' + 2A''$	$2A_g + 2E_{2g} + 2B_u + 2E_{1u} + 2B_g + 2E_{1g} + 2A_u + 2E_{2u}$

Table 3.1 – Splitting Pattern of the Isolated $[AsO_3]^{3-}$ Group

3.4.2.2 *Raman Spectra of Finnemanite*

The non-polarised spectrum of natural and synthetic finnemanite in the 900 – 100 cm^{-1} region is presented in Fig. 3.4. The spectra of specimens agree favourably, with minor differences in intensity probably due to the orientation effects in the natural specimen. In the higher wavenumber region the spectra are characterised by a weak band at 808 cm^{-1}, a strong band at 733 cm^{-1} overlying a shoulder at 726 cm^{-1}, and weak bands at 640 and 575 cm^{-1}. Weak to medium bands are found at 450, 372, and 354 cm^{-1}, whereas the lower wavenumber region exhibits a number of broad overlapping bands. The broader band profiles in this region in the spectrum of the synthetic specimen compared to the natural specimen made it more difficult to determine band positions, which caused some discrepancies in the positions of the shoulders between the two spectra.

The single crystal data is presented in Figs. 3.5 – 3.7. Figs. 3.5 and 3.6 show parallel spectra collected on *a*, *b*, and *c* faces of the crystal, the relative intensities of each band allowing assignments to be made to either A_g or E_{2g} symmetry. The assignments were made based on whether the band of interest had higher intensity in the *cc* or *aa*/*bb* orientations. If a band is present with considerable intensity in both *cc* and *aa*/*bb* orientations then it is assigned to A_g symmetry, and if it is present in the *aa*/*bb* and *ab* orientations (Fig. 3.7) only then it is assigned to E_{2g} symmetry. If a band is present in the *ac* orientation only, then it is assigned to E_{1g} symmetry.

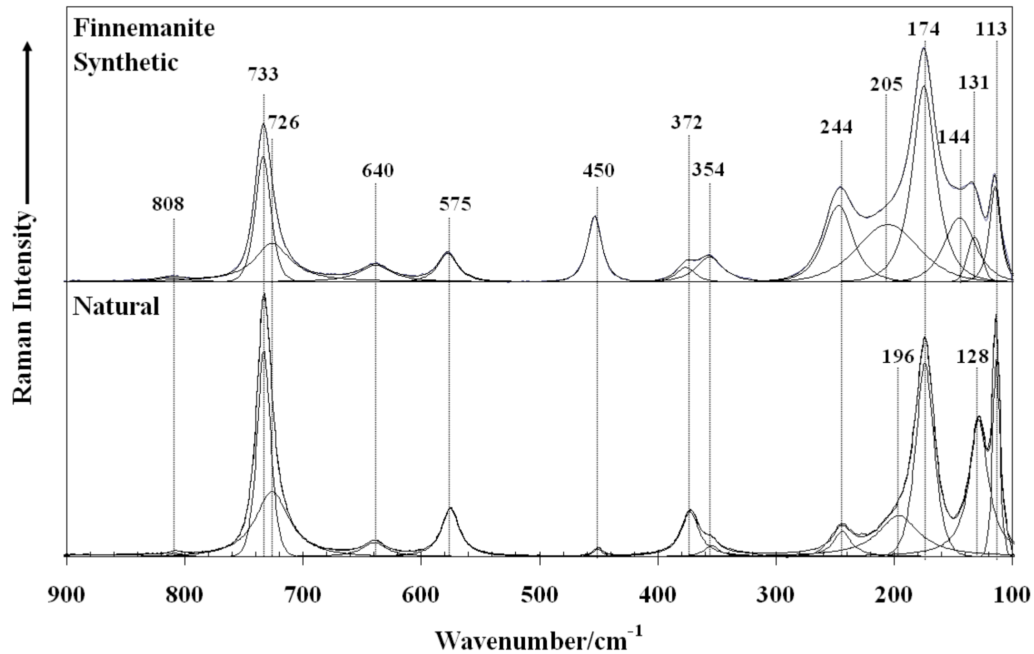

Fig. 3.4 – Raman spectrum of natural and synthetic finnemanite in the 900 – 100 cm^{-1} region

Bands at 808, 733, 726, 372, 244, 196, 174, 128, and 113 cm^{-1} are determined to be of A_g symmetry. The above assignments were made based on their significant intensity in the *cc* orientations (Figs. 3.5 and 3.6) compared to the *aa*/*bb* spectrum on the same face. The *aa*/*bb* and *cc* spectra on a given face were collected on the same spot, ruling out the likelihood that optical quality of the spot is responsible for the intensity differences between the spectra. The band at 733 cm^{-1}, although appearing in the *ab* orientation (Fig. 3.7), was assigned to A_g symmetry because it appears the most intense in the *cc* orientation (Fig. 3.5). The band at 808 cm^{-1} is just detectable in the ACCA spectrum, but the existence of this band is not doubtful since it is observed in the depolarised spectra of the natural and synthetic specimens.

Bands at 456, 452, 358, and 166 cm^{-1} are determined to be of E_{2g} symmetry based on the observation of these bands in the *aa*/*bb* orientations as well as *ab*. The depolarised spectrum (Fig. 3.4) shows only one band at 453 cm^{-1}, but it may contain two E_{2g} bands at 456 (CABC) and 452 cm^{-1} (CAAC). The two bands are considered to be different because the shift is bigger than the experimental error in the band positions. An E_{2g} band at 160 cm^{-1} in the CABC spectrum was not observed in the parallel spectra possibly due to strong overlying bands.

E_{1g} bands should only be observed in the *ac* spectrum, therefore bands visible in the BACB spectrum (Fig. 3.7) at 640, 354, and 207 cm^{-1} were assigned accordingly. The band at 207 cm^{-1} was not resolved in the peak-fitted depolarised spectrum (Fig. 3.4) due to overlap with stronger bands. The band positions and symmetry assignments are summarised in Table 3.2.

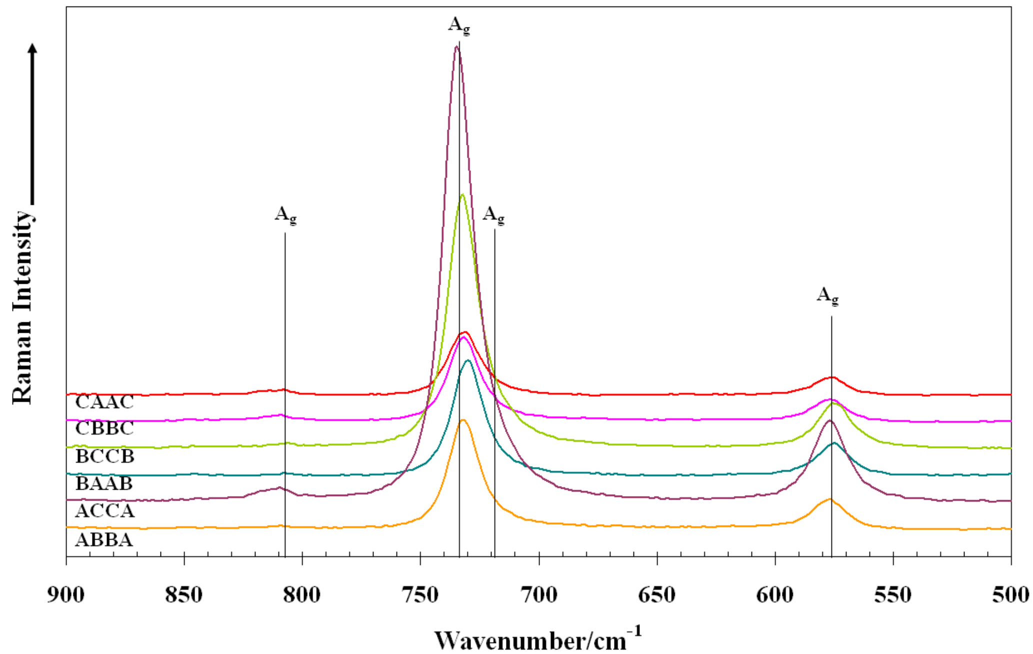

Fig. 3.5 – Oriented single-crystal parallel Raman spectra of finnemanite in the 900 – 500 cm^{-1} region

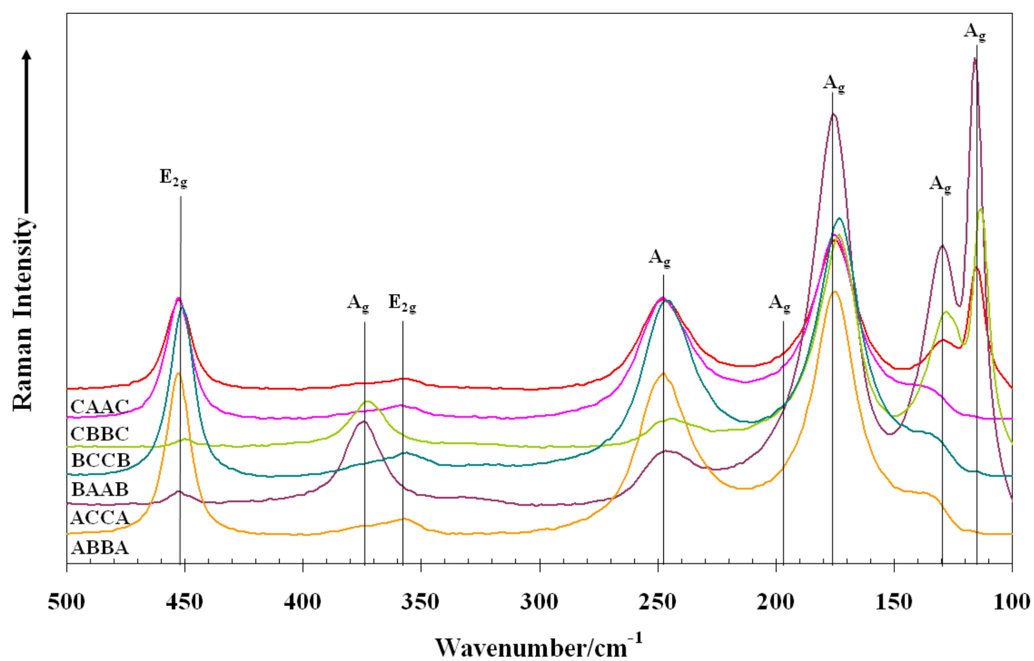

Fig. 3.6 – Oriented single-crystal parallel Raman spectra of finnemanite in the 500 – 100 cm^{-1} region

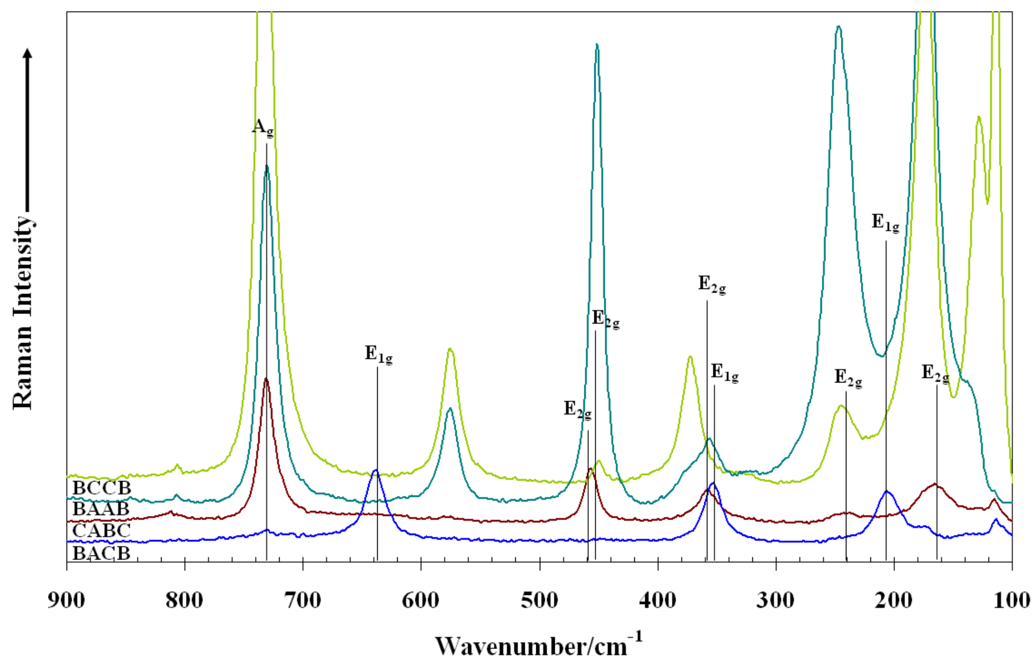

Fig. 3.7 – Oriented single-crystal parallel and perpendicular spectra of finnemanite in the 900 – 100 cm^{-1}

3.5 DISCUSSION

The fundamental modes of the free $[AsO_3]^{3-}$ ion in solution were determined by Loehr and Plane [17] and estimated by Tossell [18]. DFT calculations were also performed in this study on a free $[AsO_3]^{3-}$ ion. The results are summarised in Table 3.3 along with assignments of the present work. A difference in the calculated results between the present work and that of Tossell [18] may be explained by different scaling factors used, and Tossell also explains that the model utilised in the study was less accurate when applied to more highly charged anionic species stable only at quite high pH. The work of Loehr and Plane [17] gave clear positions of υ_1 and υ_3 but the lower wavenumber region consisted of broad bands so υ_2 and υ_4 were not resolved. As elaborated in the factor group analysis, υ_1 and υ_2 each gives A_g and E_{2g} in the Raman spectrum and υ_3 and υ_4 each gives A_g, E_{1g}, and E_{2g}. A few of these components especially E_{1g} and E_{2g} were not observed in due to their intrinsic weakness. Therefore the band assignments were made based on band symmetry and the proximity of the observed A_g bands to the calculated band position of the free $[AsO_3]^{3-}$ ion.

The most intense band at 733 cm^{-1} was assigned to the symmetric stretch (υ_1) of the AsO_3 unit, and its shoulder at 726 cm^{-1} to the antisymmetric stretch (υ_3) following the assignment made by Loehr and Plane on a study of arsenite ions in solution [17]. The higher wavenumber of the symmetric stretch with respect to the antisymmetric stretch has been known to occur in most C_{3v} molecules [73]. As well as applying to arsenite and antimonite ions, this is also the case for sulfites [74]. The small difference between υ_1 and υ_3 agrees with the calculated results of the present study and Tossell [18]. The expected E_{2g} modes of both stretches were not observed in close proximity to either bands, however the E_{1g} mode of the antisymmetric stretch was observed at 640 cm^{-1}. Bands at 372 (A_g) and 357 cm^{-1} (E_{2g}) were assigned to the symmetric deformation (υ_2) and at 244 (A_g) and 207 cm^{-1} (E_{1g}) to the antisymmetric deformation (υ_4).

Band Position (cm^{-1})	Assignment
808	A_g
733	A_g
726	A_g
640	E_{1g}
575	A_g
456	E_{2g}
452	E_{2g}
372	A_g
357	E_{2g}
353	E_{1g}
244	A_g
239	E_{2g}
207	E_{1g}
196	A_g
174	A_g
166	E_{2g}
128	A_g
115	A_g

Table 3.2 – Band symmetry assignments of finnemanite

	Free Ion AsO_3^{3-}			Finnemanite
	Loehr & Plane	Tossell	This study	
υ_1	752	690	653	733 (A_g)
υ_2	~340	-	382	372 (A_g), 357 (E_{2g})
υ_3	680	672	631	726 (A_g), 640 (E_{1g})
υ_4	~340	-	309	244 (A_g), 239 (E_{2g}), 207 (E_{1g})

Table 3.3 – Band assignments for the AsO_3^{3-} group in finnemanite

Finnemanite belongs to a group of ortho arsenite minerals which includes reinerite $Zn_3(AsO_3)_2$ [23], cafarsite $Ca_8(Ti,Fe,Fe,Mn)_{6-7}(AsO_3)_{12}.4H_2O$ [54], and nealite $Pb_4Fe(AsO_3)_2Cl_4.2H_2O$ [67,68]. Fig. 3.8 shows the stacked Raman spectra of the above four minerals for comparison. All four minerals show a number of bands at 900 – 600 cm^{-1}, with the most intense bands located approximately at 800 – 700 cm^{-1}. The narrow profile of the υ_1 band in finnemanite appears to have the most in common with that of nealite, whereas the spectra of reinerite and cafarsite in this region consist of numerous overlapping bands. This observation may be explained as follows. Nealite is a triclinic (C_i) mineral possessing only one AsO_3 group (C_1 site) with its factor group analysis predicting a total of $3A_g$ modes corresponding to υ_1 and υ_3. Cafarsite (cubic – T_h^2) has three inequivalent AsO_3 groups (one on C_3 site, the rest on C_1 sites) and reinerite (orthorhombic – D_{2h}^9) possesses two (C_s sites). Factor group analysis predicts a total of $7A_g + 7E_g$ for cafarsite and $4A_g + 4B_{1g} + 2B_{2g} + 2B_{3g}$ for reinerite corresponding to the stretching vibrations of all of the inequivalent arsenite groups.

The presence of Ca, Mn, Ti, and Fe polyhedra in cafarsite, and Pb-O-Cl and Fe-O-Cl polyhedra in nealite makes it difficult to tease out the vibrations of the AsO_3 unit since there may be some coincidence of the AsO_3 vibrations with those of the above polyhedra. The structure of reinerite shows the least number of polyhedra other than AsO_3, and therefore has less potential for interference from bands not belonging to the AsO_3 moiety. The spectrum of reinerite shows a group of bands at approximately 850 – 600 cm^{-1} and 350 – 100 cm^{-1}, and it is reasonable to assign most of these to AsO_3 vibrations. This observation agrees with the finnemanite assignment made in this study (733 – 640 cm^{-1} assigned to stretches, 372 – 207 cm^{-1} to deformations). Bands in the above region are also observed in the spectra of nealite and cafarsite.

The spectra of nealite and finnemanite appear to exhibit bands at 600 – 400 cm^{-1} and a very weak band just above 800 cm^{-1} which are similar in appearance in both compounds. Since the structures of both compounds possess Pb-O-Cl polyhedra, the above bands may be assigned to vibrations of these polyhedra. To explore this further, the spectra of finnemanite and nealite are compared to those of synthetic $Pb_2(AsO_2)_3Cl$, $Pb_2As_2O_5$, and $PbAs_2O_4$ (Fig. 3.9). Similar weak bands are found at 570 – 550 and 470 – 420 cm^{-1} in the spectra of lead chloride arsenite compounds whereas in this region $Pb_2As_2O_5$ and $PbAs_2O_4$ show medium to strong bands corresponding to bridging As-O vibrations. Similarly the weak band(s) just above 800 cm^{-1} are only observed in the spectra of lead chloride arsenite compounds, and not in the spectra of $Pb_2As_2O_5$ and $PbAs_2O_4$. This observation supports the assignment of these bands to the vibrations of the Pb-O-Cl polyhedra.

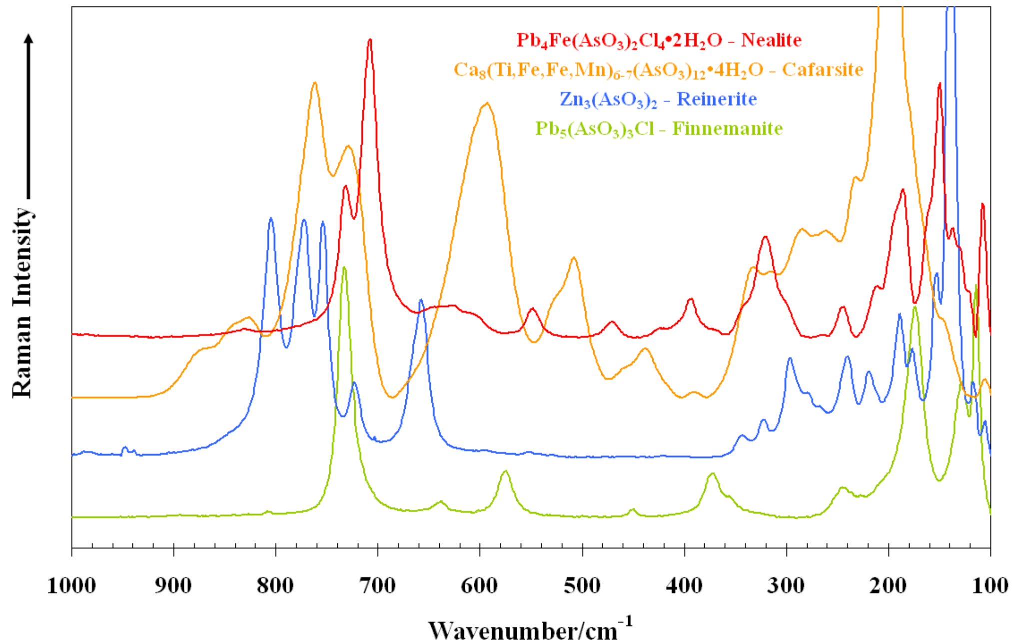

Fig. 3.8 – Stacked Raman spectra of ortho arsenite minerals nealite, cafarsite, reinerite, and finnemanite in the 1000 – 100 cm^{-1} region

3.6 CONCLUSION

The Raman spectrum of a natural sample of finnemanite is characterised by a strong band at 734 cm^{-1} overlying a shoulder at 726 cm^{-1}, weak bands at 808, 640, 575 cm^{-1}, and overlapping bands at 244 – 113 cm^{-1}. The Raman spectrum of pure synthetic finnemanite was found to agree very closely to that of the natural specimen. An oriented single crystal Raman study was performed which showed good separation between different symmetry species. Band assignments were made based on band symmetry and experimental band positions from literature and DFT calculated Raman spectrum.

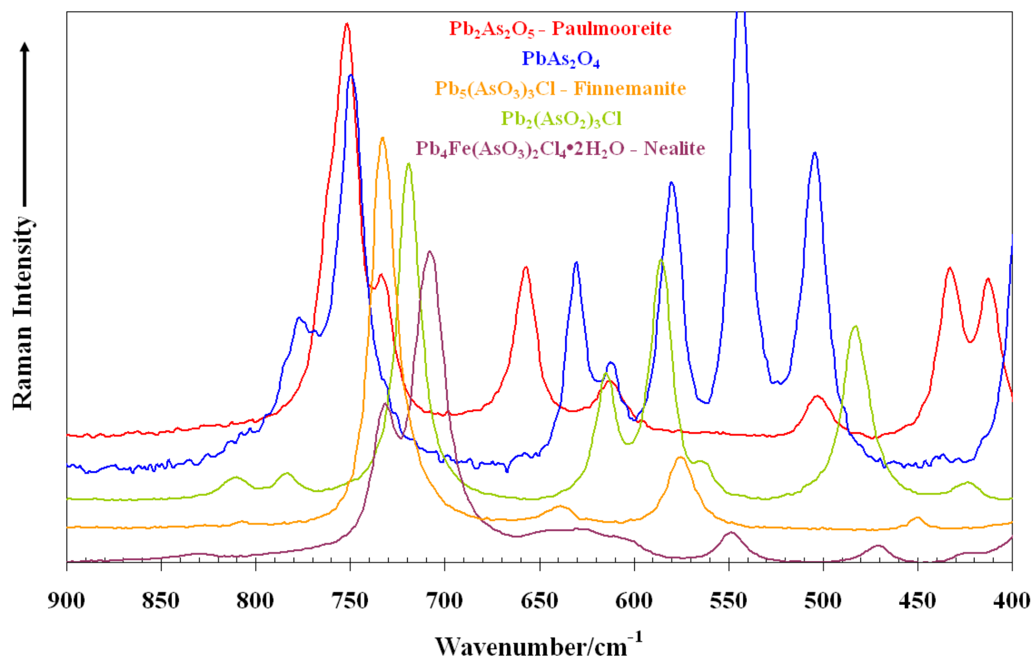

Fig. 3.9 – Stacked Raman spectra of $Pb_2As_2O_5$, $PbAs_2O_4$, $Pb_2(AsO_2)_3Cl$, finnemanite, and nealite in the 900 – 400 cm^{-1} region

The band at 734 cm^{-1} was assigned to $\upsilon_1(AsO_3)$, bands at 726 and 640 cm^{-1} assigned to υ_3, 372 and 357 cm^{-1} to υ_2, and 244, 239 and 207 cm^{-1} to υ_4. The positions of the above bands compare favourably to literature and DFT data. Comparison with other ortho arsenite minerals confirmed the above assignments. Vibrations of the Pb-O-Cl polyhedra were also able to be tentatively assigned based on comparison with various lead arsenite ($PbAs_2O_4$ and paulmooreite) and lead chloride arsenite (nealite and $Pb_2(AsO_2)_3Cl$) compounds. Factor group analysis predicted that there should be $10A_g + 7E_{1g} + 11E_{2g}$ in the Raman spectrum and in this study $10A_g + 3E_{1g} + 5E_{2g}$ were observed.

Chapter 4

Single Crystal Raman Spectroscopy of Natural Paulmooreite $Pb_2As_2O_5$ in Comparison with the Synthesised Mineral

4.1 INTRODUCTION

Paulmooreite is a lead arsenite mineral containing dimeric $[As_2O_5]^{4-}$ units, which was first announced as a new mineral by Dunn et al. [25]. Its structure was refined by Araki et al. [77] who placed it in the monoclinic space group $P2_1/a$ (C_{2h}^5), a = 13.584, b = 5.650, c = 8.551 Å, and Z = 4. It belongs to a small group of diarsenite minerals consisting of vajdakite $[(MoO_2)_2(H_2O)_2As_2O_5].H_2O$ [26] and gebhardite $Pb_8(As_2O_5)_2OCl_6$ [78]; the dimeric unit in each mineral differing by the orientation of one trigonal pyramid to the other. In paulmooreite, the triangular bases of the dimer are oriented nearly normal to each other [77].

The natural paulmooreite sample was kindly supplied by the Swedish Museum of Natural History (specimen number NRM532109). In preparing a synthetic analogue of paulmooreite, hydrothermal and wet synthetic methods were explored including the method given by Pertlik [5] who reported the presence of $Pb_2As_2O_5$ among the products of the hydrothermal synthesis of $Pb_2(AsO_2)_3Cl$. The details of the different synthetic routes will be discussed in the Experimental section.

To aid the determination of the contribution of the diarsenite unit to the vibrational spectra, the Raman spectrum of an isolated $[As_2O_5]^{4-}$ ion was calculated using Hartree-Fock methods. Furthermore to determine the contribution of the bridging and terminal As-O atoms the spectra of $Pb_2As_2O_5$ was compared with related synthetic compounds $PbAs_2O_4$ and $Pb_2(AsO_2)_3Cl$ and natural finnemanite $Pb_5(AsO_3)_3Cl$. The vibrational spectra of paulmooreite and the above compounds have not been previously published. This study presents the single crystal data for natural and synthetic paulmooreite and makes band assignments according to symmetry and type.

4.2 EXPERIMENTAL

4.2.1 Minerals

Single crystals of paulmooreite and finnemanite were supplied by the Swedish Museum of Natural History of specimen numbers NRM532109 and NRM883736 respectively. Both specimens originated from the Långban locality, Filipstad district, Värmland province, Sweden.

4.2.2 Synthetic Procedures

Pertlik reported the hydrothermal synthesis of $Pb_2(AsO_2)_3Cl$ [5]. The reactants were $PbCl_2$ and PbO in a 1:10 weight ratio and As_2O_3. The reaction was performed using 1M acetic acid as solvent (80% fill factor) over 10 days at temperatures ranging from about 30°C to 230°C. The product was found to be a mixture of $Pb_2(AsO_2)_3Cl$ and $Pb_2As_2O_5$ in a 1:50 weight ratio. This procedure was followed as a starting point for synthesis, with the following conditions: P1 – 150°C for 4 days, P2 – 50°C for 4 days, P3 – 150°C for 10 days, and P4 – 60°C for 7 days.

Other hydrothermal reactions were performed, using various temperatures and reaction times. PbO and As_2O_3 were used in a mole ratio of 2:1. In all cases 1M acetic acid was used as solvent unless indicated. The first set of reactions was performed at 150°C for 10 days (H1) and at 210°C for 4 days (H2). The second set of reactions used 1M acetic acid bubbled with N_2 prior to sealing the autoclave with the following conditions: H3 – 60°C for 7 days, H4 – 150°C for 2 days, and H5 – 150°C for 2 days using water bubbled with N_2.

Wet synthesis methods were also attempted. NaOH and As_2O_3 were mixed in a ratio of 4:1 to give one mole of $Na_4As_2O_5$, which is then mixed with two moles of $Pb(NO_3)_2$. The precipitate and mother liquor were aged for 7 days at W1 – room temperature, W2 – 40°C, and W3 – 60°C.

4.2.3 Raman Microscopy

A natural crystal of paulmooreite was placed on the corner of a perfect cube and aligned parallel to the sides of the cube. It was assumed that the crystal laid on its perfect (001) cleavage plane. In the plane of the crystal, the long axis corresponded to the *b* axis, and the *a* axis was at right angles to the long axis. The synthetic crystal was not oriented due to its size.

4.2.4 Hartree-Fock Calculations

Calculations were performed using the Gaussian 03 program [72] and the GaussView 4.0 (Gaussian, Inc.,Wallingford, CT) front end, running on an SGI Origin 3000 supercomputer. The wavenumbers of the fundamental modes were calculated using Hartree-Fock (HF) with B3-LYP method and a 6-31G(d) basis set for O atoms and Lanl2dz for As. A scaling factor of

0.972 was applied. Raman intensities were calculated from the Gaussian activities based on 633 nm excitation.

4.3 DESCRIPTION OF CRYSTAL STRUCTURE

Paulmooreite is monoclinic with space group $P2_1/a$ (C_{2h}^5) and four formula units [77]. The crystal cell dimensions are a = 13.584, b = 5.650, c = 8.551 Å. Two inequivalent As^{3+} atoms are connected through a common O atom and two other O atoms each, forming a dimeric $[As^{3+}{}_2O_5]^{4-}$ unit. Each AsO_3 pyramid in the $[As_2O_5]^{4-}$ unit may be oriented in number of different ways with respect to the other; parallel orientation (Fig. 4.1a), 90° orientation, and 180° orientation. In paulmooreite the dimers have approximately 90° orientation (Fig. 4.1b), where one AsO_3 pyramid is rotated 90° from the ideal parallel orientation. There are also two inequivalent Pb^{2+} atoms in distorted tetragonal pyramidal geometry. The symmetry of the AsO_3 pyramids is reduced to C_1 from the ideal trigonal pyramid (C_{3v}) symmetry. The bridging $O_{(3)}$ atom has longer bond lengths to $As_{(1)}$ and $As_{(2)}$ than the terminal O atoms. $As_{(1)}$-$O_{(3)}$ and $As_{(2)}$-$O_{(3)}$ bond lengths are 1.826 and 1.842 Å, respectively. The bond lengths of the terminal O atoms belonging to $As_{(1)}$ are 1.747 and 1.750 Å, and those belonging to $As_{(2)}$ are 1.733 and 1.772 Å.

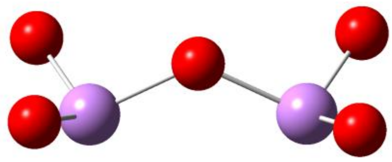

Fig. 4.1a – $[As_2O_5]^{4-}$ dimer in parallel orientation (As:purple)

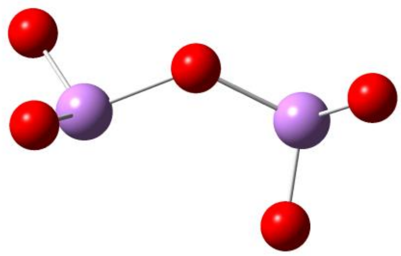

Fig. 4.1b – $[As_2O_5]^{4-}$ dimer in paulmooreite (90° orientation)

4.4 RESULTS

4.4.1 Results of X-ray Diffraction

Using the procedures outlined by Pertlik [5], it was found that $PbAs_2O_4$ was formed instead of $Pb_2As_2O_5$. $Pb_2(AsO_2)_3Cl$ was also formed in this procedure. Different temperatures and reaction times attempted were: P1 – 150°C for 4 days, P2 – 50°C for 4 days, P3 – 150°C for 10 days, and P4 – 60°C for 7 days. The same products had resulted in all instances. Fig. 4.2 shows the XRD pattern of the product of P3.

The first set of hydrothermal reactions outside of the procedures given by Pertlik were performed at 150°C for 10 days (H1) and at 210°C for 4 days (H2), which gave hydroxymimetite $Pb_5(AsO_4)_3OH$ (Fig. 4.3). Since the formation of an arsenate compound indicates the presence of oxidising conditions in the system, N_2 was bubbled through the solvent prior to sealing the autoclave. to prevent the oxidation of As^{3+}. This reaction was performed at 60°C for 7 days (H3) giving only $PbAs_2O_4$ as product. Shortening the reaction time to 2 days finally resulted in $Pb_2As_2O_5$ as part of the product. At 150°C in acetic acid (H4) the products formed were 70% $Pb_2As_2O_5$ and 30% $PbAs_2O_4$, while the same reaction using water (H5) gives approximately 50% $Pb_2As_2O_5$ and 50% $PbAs_2O_4$. Fig. 4.4 shows the XRD patterns of the products of reactions H3, H4 and H5.

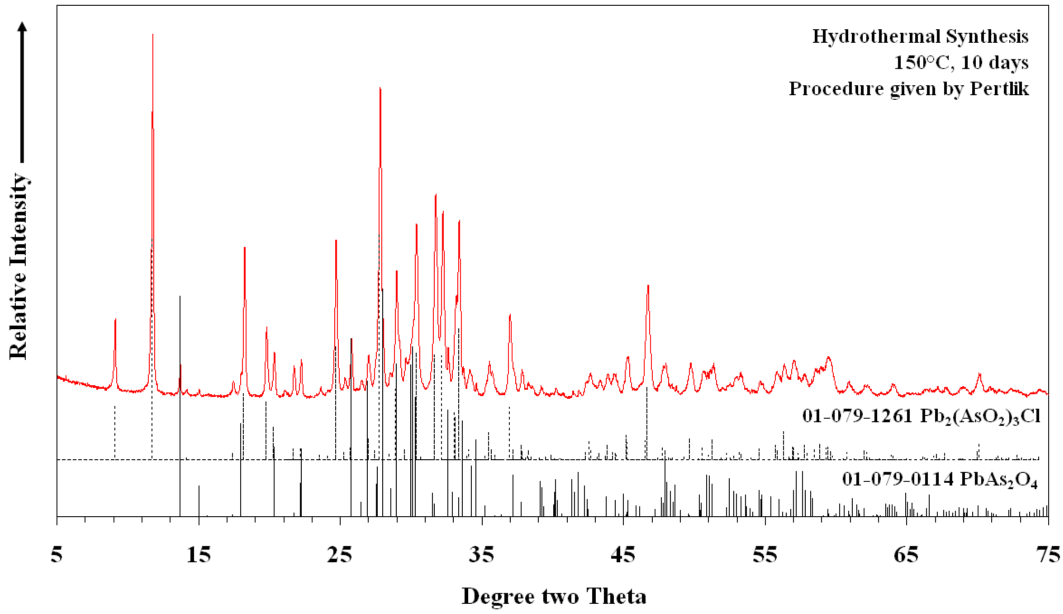

Fig. 4.2 – XRD pattern of the product of reaction P3

The wet syntheses gave a white, fluffy precipitate of $Pb_2As_2O_5$. The precipitate and mother liquor were aged for 7 days at room temperature (W1), 40°C (W2), and 60°C (W3). XRD patterns of the product of W1 and W2 (Fig. 4.5) shows $Pb_2As_2O_5$ to be the major constituent. Product of W3 (Fig. 4.6) also shows $Pb_2As_2O_5$, however $PbAs_2O_6$ is also detected in addition to other products that could not be identified.

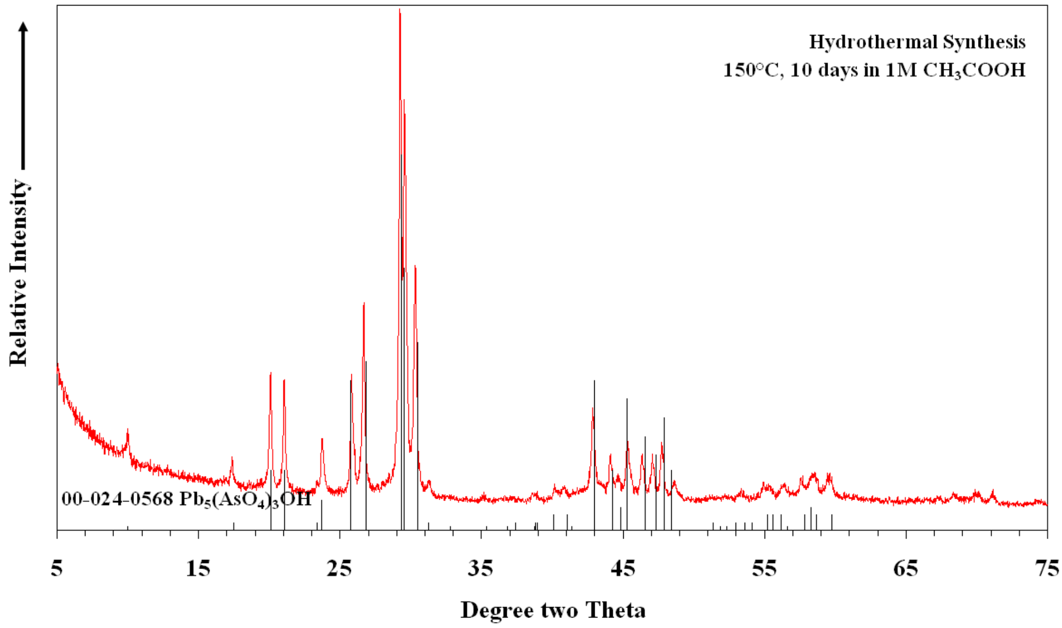

Fig. 4.3 – XRD pattern of the product of reaction H1

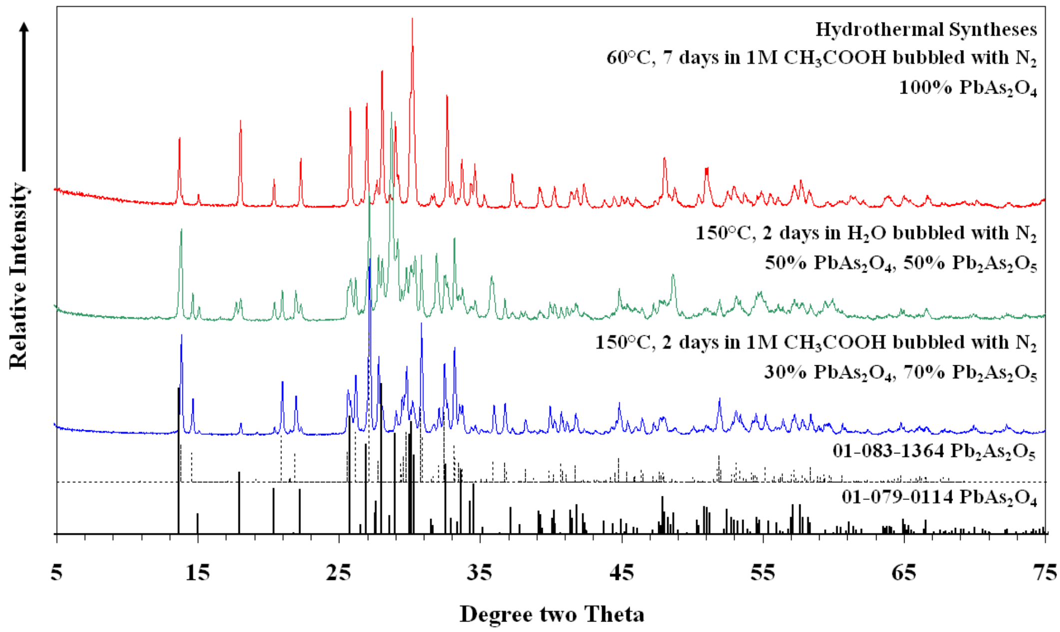

Fig. 4.4 – XRD patterns of products of reactions H3 – H5

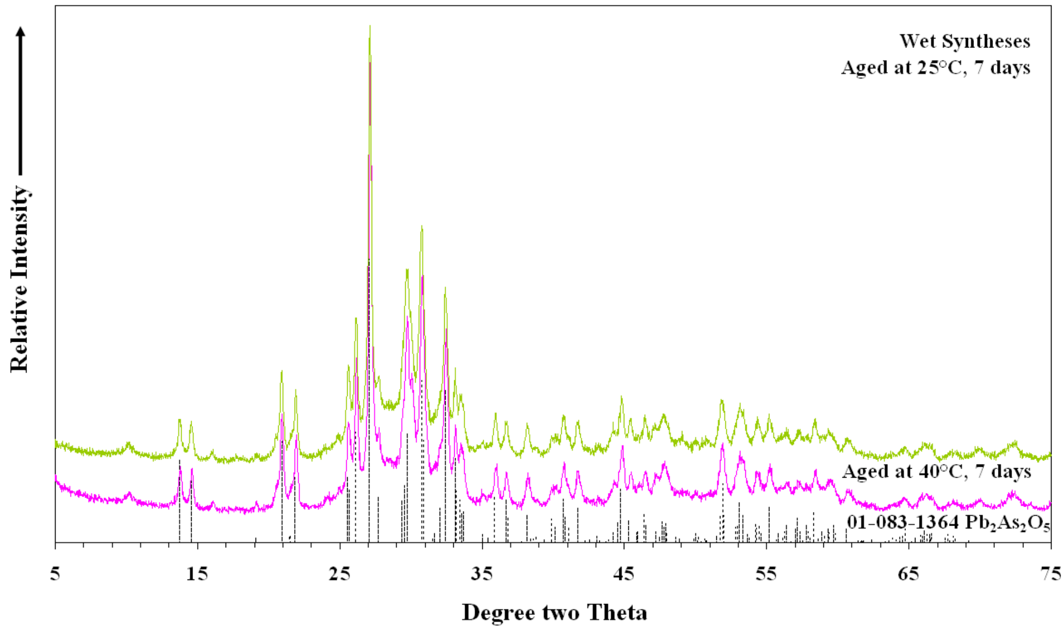

Fig. 4.5 – XRD patterns of products of reactions W1 and W2

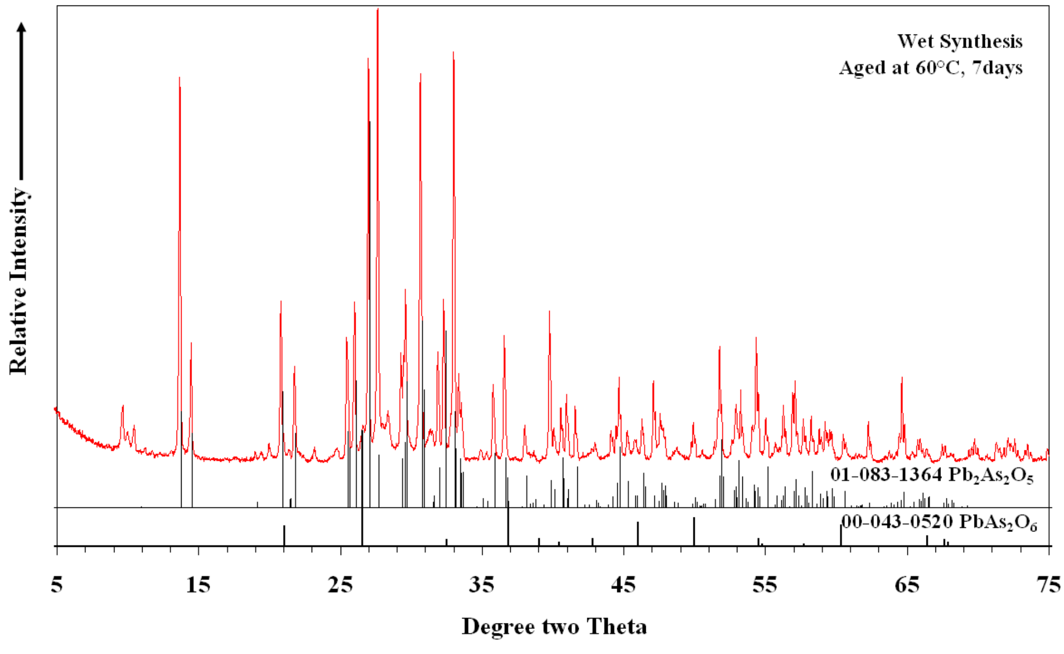

Fig. 4.6 – XRD pattern of the product of reaction W3

4.4.2 Scanning Electron Microscopy

The SEM micrographs of $Pb_2As_2O_5$ synthesised by reactions W1 and W2 are shown in Figs. 4.7a and b. The product of W2 appears to have three different morphologies. There are aggregates of small fibrous particles, between which are interspersed thin plates of about 10 – 20 microns arranged in a pine-needle formation A significant amount of the crystals takes the form of flat plates of about 20 – 100 microns. The product of W1 appears uniform in morphology and very similar to the fibrous particles in W2 except that in this case they form spheres.

4.4.3 Raman Microscopy

4.4.3.1 *Factor Group Analysis*

The unit cell of paulmooreite is the primitive unit cell and it contains four formula units. Thus a primitive unit cell contains 36 atoms. The number of allowable modes is 105 consisting of $27A_g + 27B_g + 26A_u + 25B_u$. The analysis is represented in Table 4.1. The form of the polarisability tensor for C_{2h} crystals dictates that A_g modes are observed in the *aa*, *bb*, *cc*, and *ac* orientations and B_g modes in the *ab* and *bc* orientations. The isolated $[As_2O_5]^{4-}$ ion with the pyramidal bases in a parallel orientation has C_{2v} symmetry and 15 normal modes of vibration consisting of $5A_1 + 3A_2 + 3B_1 + 4B_2$. On a C_1 site, such as the case with paulmooreite, each of the above modes turns into an *A* mode, and each *A* mode splits into A_g, B_g, A_u and B_u in a C_{2h} crystal. This splitting pattern is summarised in Table 4.1.

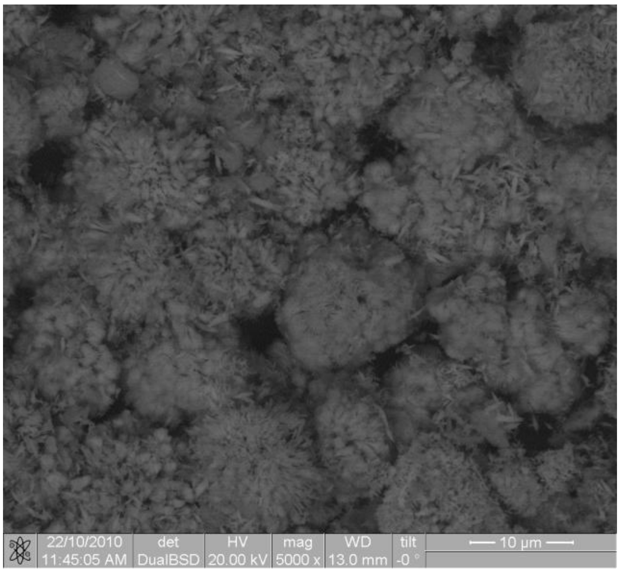

Fig. 4.7a – SEM micrograph of product of reaction W1

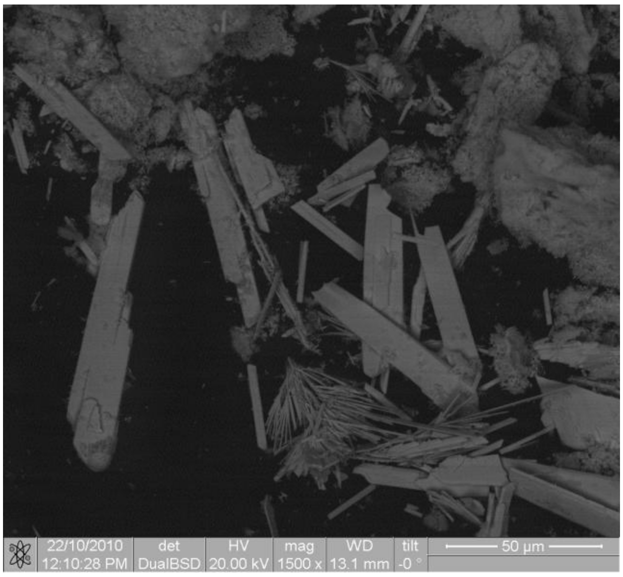

Fig. 4.7b – SEM micrograph of product of reaction W2

C_{2v}	C_1	C_{2h}
$5A_1$	$15A$	$15A_g$
$3A_2$		$15B_g$
$3B_1$		$15A_u$
$4B_2$		$15B_u$

Table 4.1 – Splitting Pattern of Isolated $[As_2O_5]^{4-}$ Ion

4.4.3.2 *Raman Spectra of Paulmooreite*

Paulmooreite is biaxially positive with a birefringence of about 0.110. The optical direction which coincides with the *b* axis is Y, meaning that light travelling along the *b* axis will not encounter circular sections and will therefore experience birefringence. Crystals of paulmooreite are tabular on {100} or {001}, leading to easier collection of spectra on these faces and avoiding birefringence.

Fig. 4.8 shows spectra collected on the *a* and *c* faces of natural paulmooreite and a spectrum of the product of reaction W2. All three spectra compare favourably, with minor differences. The strongest band in all three spectra occurs at 186 cm^{-1}, followed in intensity by a band near 140 cm^{-1}, and a group of bands in the 800 – 600 cm^{-1} region. The synthetic spectrum shows bands at 637 and 598 cm^{-1} which were not observed in the natural spectra. A strong band near 140 cm^{-1} seems to be broader and may consist of two bands in the synthetic spectrum, and sharper in the natural spectra. Whether or not the above bands are 'real' will be explored in later sections based on the single crystal data.

The single crystal data of natural paulmooreite are presented in Figs. 4.9, 4.10 and 4.11. Two non-polarised spectra collected on the *a* and *c* faces are shown, along with the parallel and perpendicular spectra of each face. Single crystal spectra of synthetic paulmooreite are shown in Figs. 4.12 and 4.13. A non-polarised, parallel, and perpendicular spectrum was collected on the tabular face of the crystal.

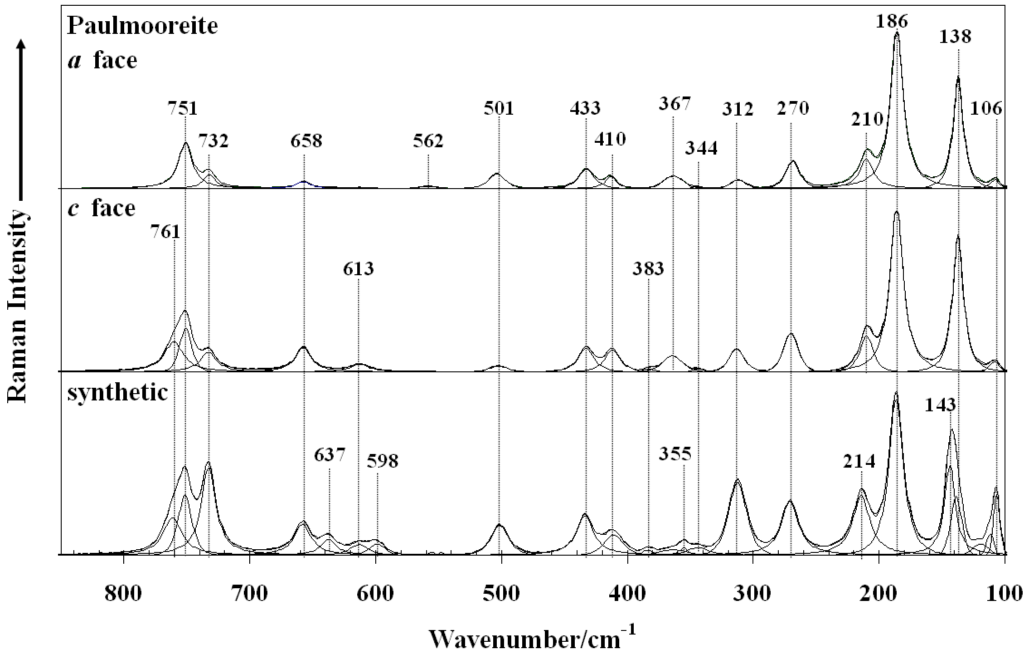

Fig. 4.8 – Raman spectra of natural and synthetic paulmooreite in the 800 – 100 cm^{-1} region

A group of bands in the 800 – 700 cm^{-1} region (Fig. 4.9) appears to consist of two A_g and B_g bands, whereas the group of bands in the 700 – 600 cm^{-1} region (Fig. 4.12) consists of three bands instead of the four observed in the non-polarised spectrum of synthetic paulmooreite (Figs. 4.12 and 4.10). The assignment of the bands around 640 and 598 cm^{-1} in the synthetic spectrum is uncertain since neither the parallel nor perpendicular spectra show these bands. However the natural non-polarised spectrum collected on the *a*-face and the ABCA spectrum show the 640 cm^{-1} band clearly defined and thus assigned to B_g symmetry. The weak band at 598 cm^{-1} is only observed in the Raman spectra of products of reactions H4, W2 and W3 and hence may be due to edge effect, resulting from the small crystal domain size. The same applies to the very weak band just above 350 cm^{-1}. A band at 560 cm^{-1} is detected only in the spectra collected on the *a*-face.

Although it is weak, it is clearly defined in the depolarised *a*-face and ABCA spectra and was determined to be of B_g symmetry. The presence of two components in the band near 140 cm^{-1} as suggested by the broadness of this band in the depolarised synthetic spectrum is confirmed by the presence of the weak B_g band just above 140 and the strong A_g band just below 140 cm^{-1}. The complete band symmetry assignments are presented in Table 4.2.

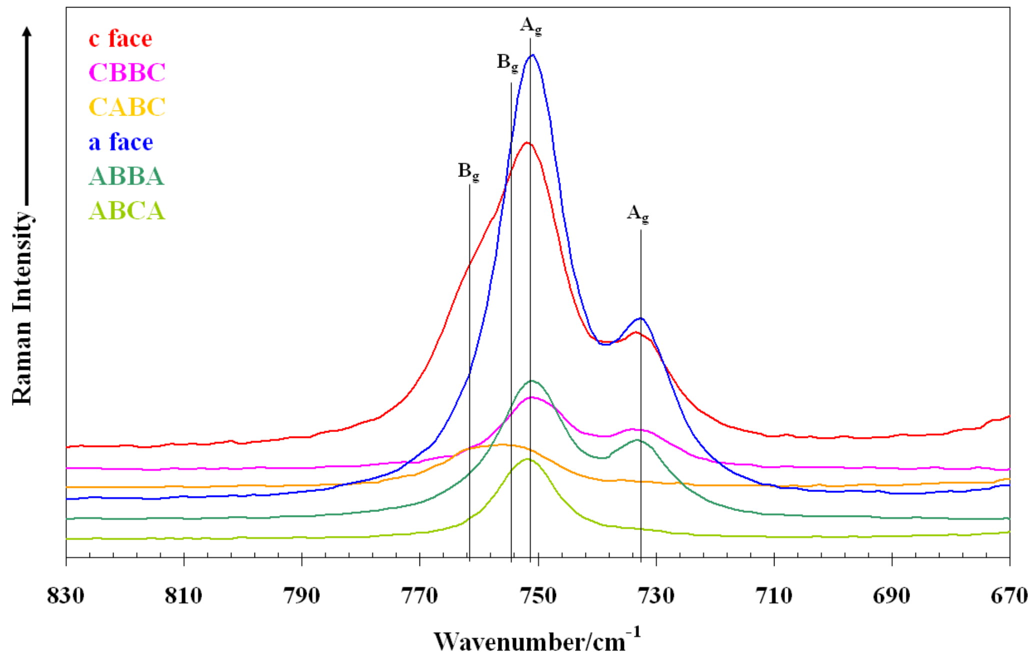

Fig. 4.9 – Oriented single crystal spectra of natural paulmooreite in the 830 – 670 cm^{-1} region

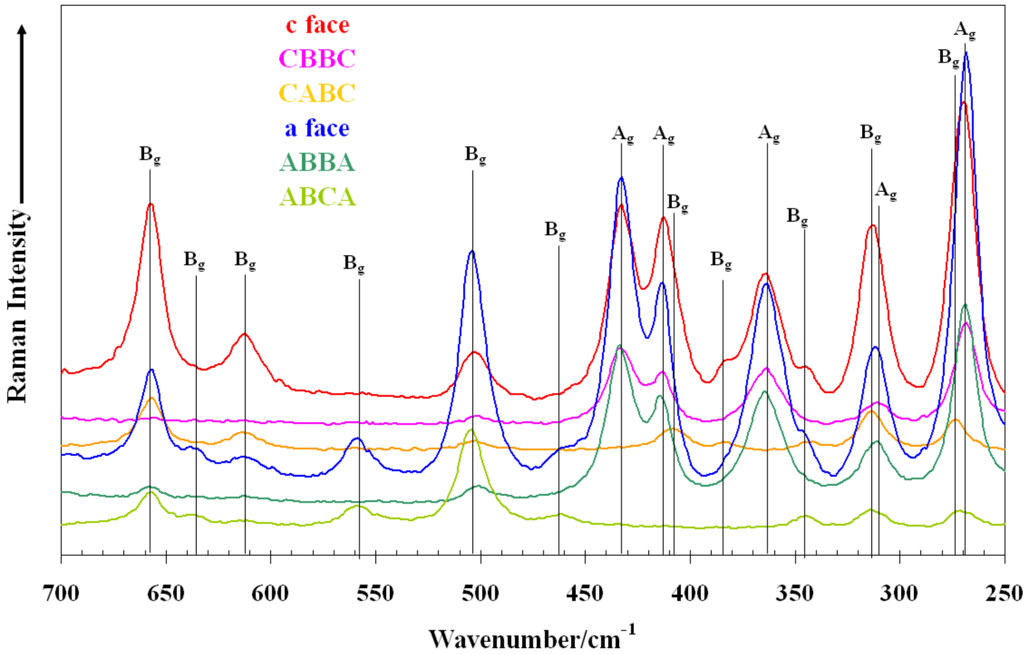

Fig. 4.10 – Oriented single crystal spectra of natural paulmooreite in the 700 – 250 cm^{-1} region.

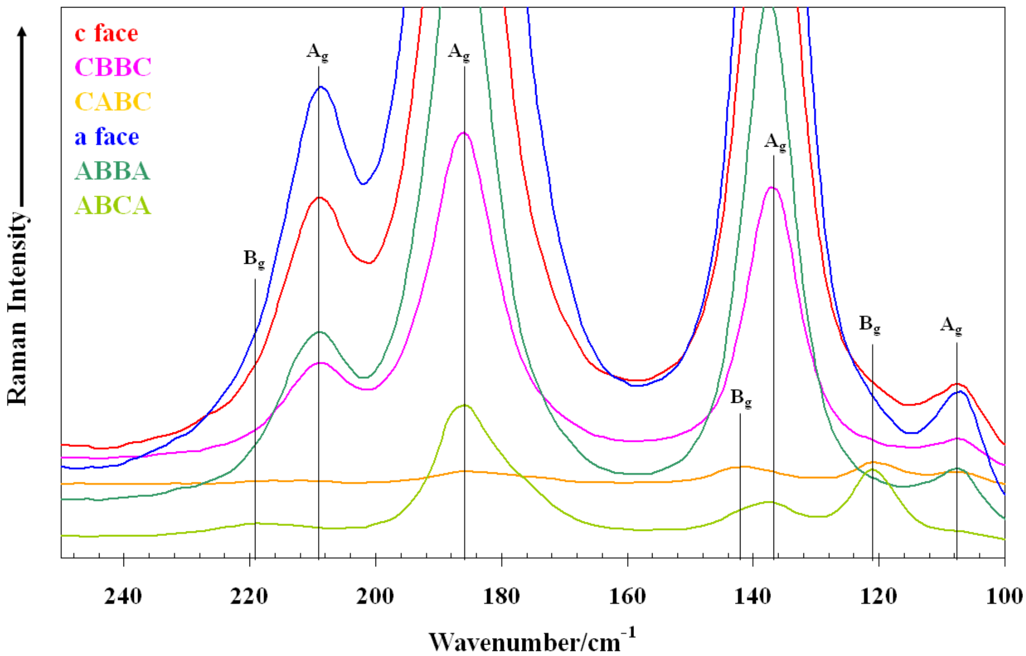

Fig. 4.11 – Oriented single crystal spectra of natural paulmooreite in the 250 – 100 cm^{-1} region.

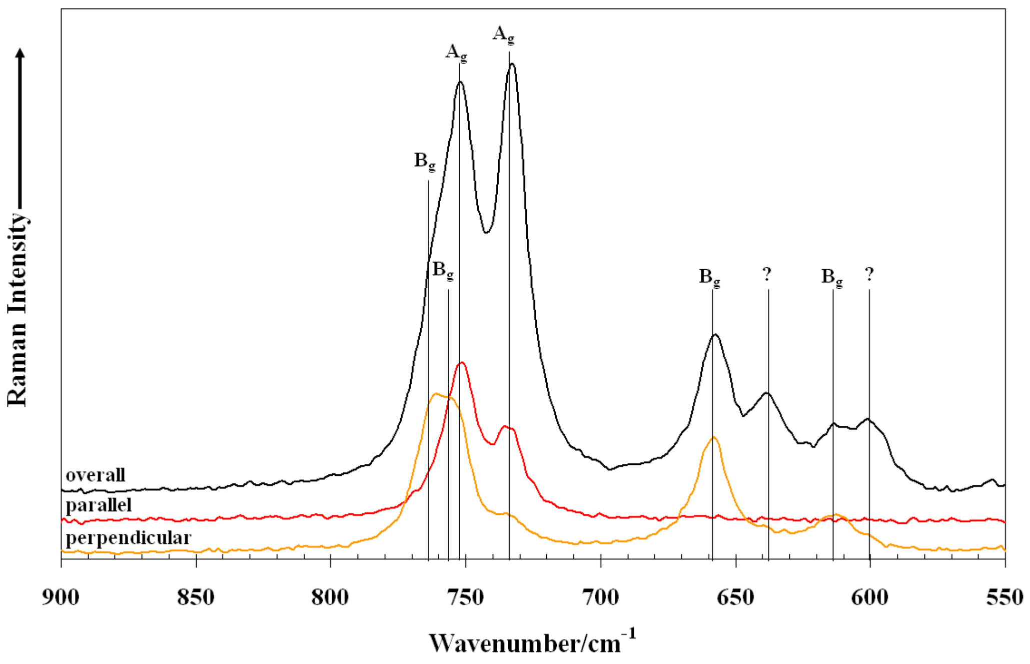

Fig. 4.12 – Oriented single crystal spectra of synthetic paulmooreite in the 900 – 550 cm^{-1} region.

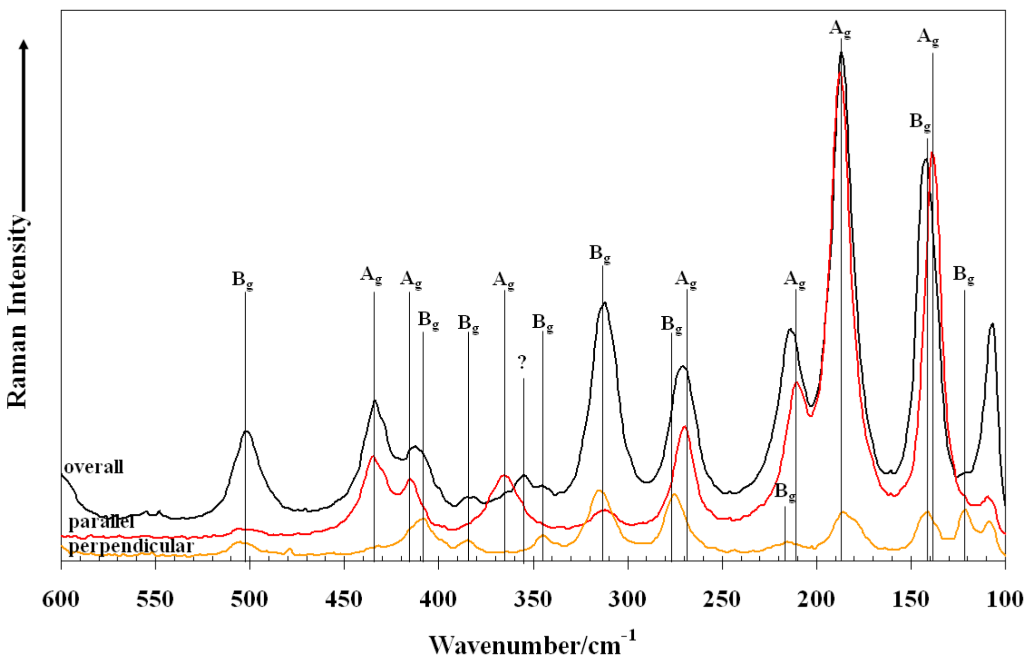

Fig. 4.13 – Oriented single crystal spectra of synthetic paulmooreite in the 600 – 100 cm^{-1} region.

4.5 DISCUSSION

Out of the 54 allowable Raman modes of paulmooreite 27 modes were observed consisting of 11A_g and 16B_g modes. Two types of As-O stretches can be expected corresponding to terminal and bridging As-O atoms. The symmetry of each AsO_3 group in the $[As_2O_5]^{4-}$ ion is reduced from the ideal trigonal pyramid (C_{3v}) symmetry to C_1. In an isolated $[As_2O_5]^{4-}$ ion with parallel orientation (thus having C_{2v} symmetry), stretches of the bridging O gives A_1 (symmetric) and B_2 (antisymmetric) modes while its symmetric deformation gives A_1. Stretches of the terminal O atoms should give A_1, A_2, B_1, and B_2 modes. If the ion occupies a C_1 site such as the case with paulmooreite each vibration will turn into a vibration of A symmetry, each of which will split into an A_g and B_g component in a C_{2h} crystal. The low symmetry in paulmooreite limits the value of factor group analysis in band assignment, therefore to aid in the task of assigning bridging and terminal O vibrations the spectra of paulmooreite are compared with the HF calculated Raman spectrum and the spectra of a number of lead arsenite compounds containing polymeric and discrete AsO_3 groups.

Spectra of natural paulmooreite collected on the *a* and *c* faces of the crystal are shown in Fig. 4.14 along with $PbAs_2O_4$ resulting from reaction H5, $Pb_2(AsO_2)_3Cl$ from reaction P3, natural finnemanite ($Pb_5(AsO_3)_3Cl$) and the HF calculated Raman spectrum of an isolated $[As_2O_5]^{4-}$ with parallel orientation (C_{2v} symmetry).

$PbAs_2O_4$ and $Pb_2(AsO_2)_3Cl$ consist of polymerised AsO_3 groups arranged into As_4O_8 rings [79] and open-branched single chains [5], respectively. Finnemanite, on the other hand, possesses isolated AsO_3 pyramids [24].

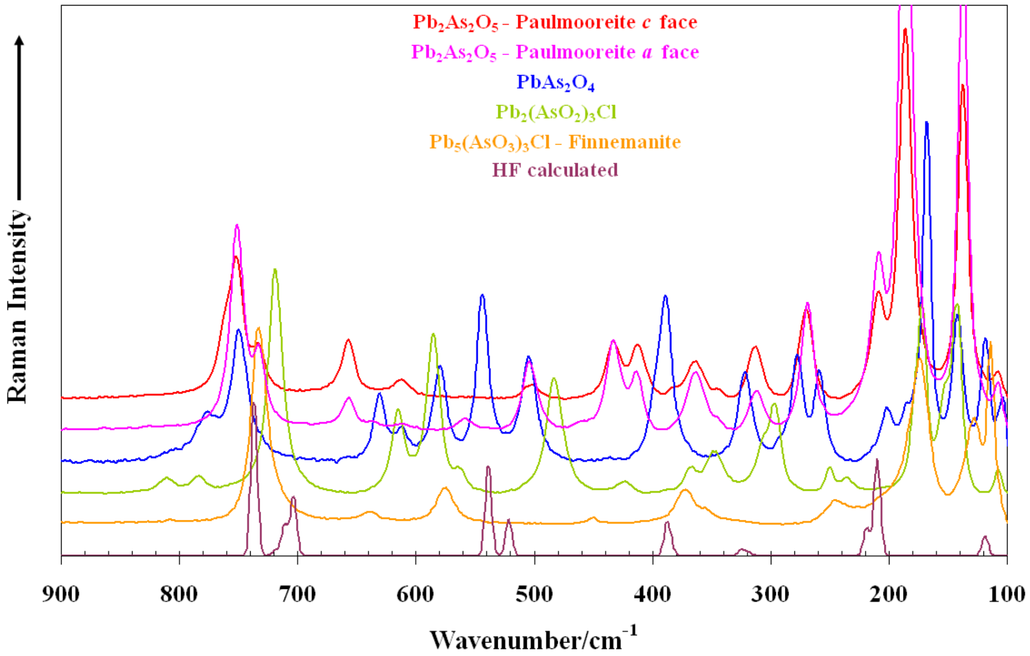

Fig. 4.14 – Stacked Raman spectra of paulmooreite,$Pb_5(AsO_3)_3Cl$, $PbAs_2O_4$, $Pb_2(AsO_2)_3Cl$, and HF calculated Rama spectrum of paulmooreite

All of the compounds show two or three bands in the 850 – 700 cm^{-1} region. A band at 734 cm^{-1} (υ_1) is the most intense in the finnemanite spectrum, with the other bands down to 200 cm^{-1} having medium or weak intensity. $PbAs_2O_4$ and $Pb_2(AsO_2)_3Cl$ show bands of higher intensity than paulmooreite in the 660 – 480 cm^{-1} region. The next group of bands which the dimeric/polymeric arsenites have in common is located in the 450 – 250 cm^{-1} band.

Bands in the 850 – 700 cm^{-1} region in the spectrum of paulmooreite are assigned to terminal As-O stretches since these bands are found in the spectra of all of the above lead arsenite compounds, including finnemanite which does not contain bridging O atoms. Single crystal data show two B_g bands at 760 and 755 cm^{-1}, and two A_g bands at 750 and 733 cm^{-1}. HF calculated data on an isolated $[As_2O_5]^{4-}$ ion presented in a study by Tossell [18] assigned terminal O stretches to bands at 751, 740, 739 and 734 cm^{-1} which agrees closely with the experimental data and HF calculated data of this study which showed bands at 736, 720, 710, and 703 cm^{-1}. FGA on an isolated $[As_2O_5]^{4-}$ ion predicts that each of these bands (which should possess A_1, A_2, B_1 and B_2 symmetry) is split into A_g and B_g components but the observed number of bands is rather less than that predicted, possibly due to accidental degeneracies arising from the highly similar terminal bond lengths of the two inequivalent As atoms.

Bands in the 660 – 480 cm^{-1} region are more intense in the spectra of $PbAs_2O_4$ and $Pb_2(AsO_2)_3Cl$, which contain two As-O_b bonds to one As-O_t, than in the spectrum of paulmooreite which contains one As-O_b and two As-O_t bonds. The above observation suggests that this region corresponds to various stretching vibrations of the bridging O atoms. The spectrum of paulmooreite shows two bands at 562 (B_g) and 503 cm^{-1} (B_g). The HF data of Tossell [18] showed bridging As-O-As stretches at 554 and 496 cm^{-1}, in excellent agreement with the experimental data. The HF data in this study calculated Raman bands corresponding to the symmetric and antisymmetric bridging O stretches at 538 and 521 cm^{-1}, which also supports the above assignments. FGA on an isolated $[As_2O_5]^{4-}$ ion predicts stretches of the bridging O giving bands of A_1 and B_2 symmetry, thus it is reasonable to assign each of the calculated bands to either A_1 or B_2. Even though there should be an A_g and B_g component to each of the above modes, the A_g components in this region may be too weak to be observed.

Band Position (cm^{-1})		Assignment
Natural	Synthetic	
760	761	B_g
755	755	B_g
750	751	A_g
733	733	A_g
658	658	B_g
635	637	B_g
613	613	B_g
	599	?
562		B_g
503	501	B_g
460		B_g
433	434	A_g
412	411	A_g
409	409	B_g
383	384	B_g
367	364	A_g
	355	?
344	344	B_g
312	312	B_g
310	310	A_g
272	274	A_g
268	270	B_g
219	214	B_g
210	209	A_g
186	186	A_g
142	144	B_g
138	139	A_g
120	120	B_g
108	107	A_g

Table 4.2 – Band symmetry assignments of paulmooreite

The observation that terminal As-O stretch occurs at a higher wavenumber fits in well with the shorter terminal As-O bond lengths (ranging from 1.733 to 1.772 Å) compared to the bridging As-O bond length (1.826 and 1.842 Å). Between vibrations of terminal and bridging O, there are three bands at 658, 635, and 613 cm^{-1} in the spectra of paulmooreite that have not been accounted for. They were not observed in the calculated data for the isolated $[As_2O_5]^{4-}$ ion, indicating the unlikelihood that these bands correspond to As-O vibrations. Bands of similar appearance and intensity, however, are observed in the spectrum of $PbAs_2O_4$, which makes it possible that these bands correspond to Pb-O vibrations.

The next group of bands which dimeric/polymeric lead arsenites have in common occurs in 460 – 240 cm^{-1}. Bands around 380 cm^{-1} have been associated with deformations of the As-O-As unit [18,19,21,22], and the HF data in this study calculated Raman bands corresponding to deformations of the terminal O atoms to occur at 386 – 382 cm^{-1}, and deformations of the bridging O atoms (although some coupling occurs with the terminal O) at 324 – 318 cm^{-1}. The spectra of paulmooreite exhibit $2A_g + 3B_g$ bands at 383 – 268 cm^{-1} and $2A_g + 2B_g$ bands at 460 – 409 cm^{-1}, the former region assigned to deformations of the terminal O and the latter to deformations of the bridging O. Except for the presence of an extra B_g band in the former region, the above observation follows the expectation that each calculated band should split into two components (A_g and B_g) caused by the lower symmetry. Similar to the previous region, bands in this region have a higher intensity in the spectrum of $PbAs_2O_4$ compared to the other lead arsenites.

No other pyroarsenite compounds had been studied to date with Raman spectroscopy apart from the theoretical study by Tossell [18]. Vajdakite, $[(MoO_2)_2(H_2O)_2As_2O_5].H_2O$, also possesses $[As_2O_5]^{4-}$ units [26] and had been studied previously with Raman spectroscopy [80]. However the presence of two inequivalent $MoO_5(H_2O)$ units makes it difficult to tease out the vibrations of the unit since there may be some coincidence of the bands. A study on some pyroantimonite compounds had been published [11]. In $Cs_4Sb_2O_5$ the SbO_3 pyramids of the $[Sb_2O_5]^{4-}$ unit have the 180° orientation. Its Raman spectrum is similar to that of paulmooreite in the 800 – 600 cm^{-1} region; a strong band at 700, a medium band at 650, and a weak band at 615 cm^{-1} (Fig. 4 of ref. 11). The first two bands were assigned to terminal Sb-O and the last to bridging Sb-O vibrations. This assignment agrees broadly with assignments made in the present study.

It is difficult to determine whether the experimental Raman spectrum reflects that predicted by factor group analysis. The low site symmetry caused by the 90° orientation of the AsO_3 units in the $[As_2O_5]^{4-}$ ion converts all vibrational modes to *A* modes and thus the experimental Raman spectrum only reflects the crystal symmetry. Furthermore it is also difficult to accurately model and calculate the Raman spectrum of the arsenite ion since its conformation in paulmooreite is not at an energy minimum in the free ion.

4.6 CONCLUSION

The Raman spectra of synthetic and natural paulmooreite are characterised by three medium bands in 800 – 700 cm^{-1}, weak-medium bands near 650, 430, 410, 365, and 310 cm^{-1}, and strong bands near 190 and 140 cm^{-1}. The single crystal data of the natural and synthetic specimens also compare favourably. It is difficult to make band assignments based on symmetry alone due to the low site symmetry. Spectral comparison with lead arsenites such as synthetic $PbAs_2O_4$ and $Pb_2(AsO_2)_3Cl$ and natural finnemanite suggests at 760, 755, 750, and 733 cm^{-1} in the spectra of paulmooreite to correspond to terminal As-O vibrations, whereas stretches of the bridging O occur at 562 and 503 cm^{-1}. The assignment above is confirmed by the shorter terminal As-O bond compared to bridging bonds and by the Raman spectrum of an isolated $[As_2O_5]^{4-}$ ion calculated by HF methods. Factor group analysis predicted $27A_g + 27B_g$ modes in the Raman spectrum and in this study $11A_g + 16B_g$ modes were observed.

Chapter 5

Single Crystal Raman Spectroscopy of Natural Leiteite $ZnAs_2O_4$ and Comparison with the Synthesised Mineral

5.1 INTRODUCTION

The zinc arsenite mineral leiteite has the formula $ZnAs_2O_4$ and is monoclinic with space group $P2_1/c$ (C_{2h}^5) and Z = 4 (a = 4.542, b = 5.022, c = 17.597 Å) and β =90.81° [27]. It occurs as brown to colourless transparent flakes with a pearlescent appearance. Leiteite is a zinc meta arsenite, which has been prepared in a laboratory as wood preservative and insecticide [8]. Meta arsenite compounds that have been previously studied include $NaAsO_2$ [41,42] and $CuAs_2O_4$ or trippkeite [7,28]. In the above compounds the arsenite group is not isolated, rather polymerised via their vertices. The structure of claudetite, the monoclinic modification of As_2O_3, is also comparable to those of meta arsenites; it consists of an infinite zigzag chain of alternating As and O [51]. Although trippkeite $CuAs_2O_4$ and the isostructural schafarzikite $Fe^{2+}Sb_2O_4$ [64,79] both have infinite arsenite or antimonite chains, leiteite is the only known mineral of its kind. In the first two the cation is found in an octahedral geometry whereas Zn is in a tetrahedral geometry in leiteite. Furthermore the bridging O atoms in the arsenite group of leiteite bind only to As atoms; one bridging O in trippkeite and schafarzikite is connected to a Cu or Fe atom as well as two As or Sb atoms.

Although Raman studies on aqueous solutions of arsenic trioxide have spanned several decades, few spectroscopic investigations have been undertaken on other arsenite minerals and none to date on leiteite. Certainly no single crystal studies of these types of minerals have ever been undertaken.

5.2 EXPERIMENTAL

5.2.1 Minerals

Crystals of leiteite were supplied by The Mineralogical Research Company. The mineral originated from the Tsumeb mine, Tsumeb, Otavi District, Oshikoto, Namibia.

5.2.2 Synthesis of Leiteite

Synthetic leiteite was prepared following the procedures given by Curtin [80]. 16.7429 g (0.0583 mol) of $ZnSO_4.7H_2O$ was dissolved in 100 mL deionised H_2O, followed by two drops glacial CH_3COOH. Another solution is made up consisting of 200 mL deionised H_2O and 12.5981 g (0.0639 mol) As_2O_3. To assist dissolution of As_2O_3 in H_2O 0.5800 g of Na_2CO_3 was added and heat was applied to boil the solution. After dissolution the temperature was allowed to decrease to below 50°C after which 5.294 g (0.0555 mol in total) of Na_2CO_3 was added. The latter solution ($NaAsO_2$) is added to the former with good agitation. Snow white crystals of $ZnAs_2O_4$ precipitated immediately, separated by filtration, washed with deionised water, and dried at 150°C overnight. Note that the glacial CH_3COOH was added to prevent the initial precipitation of zinc ortho arsenite also known as the mineral reinerite or $Zn_3(AsO_3)_2$. When CH_3COOH was not present, leiteite was still the major component of the reaction but reinerite was also present as an impurity.

5.2.3 Raman Microscopy

A crystal of leiteite was selected and placed on the corner of a perfect cube, aligned parallel to the sides of the cube using a very fine needle. The crystal flake lay flat on its perfect (001) cleavage plane with the *c* axis almost perpendicular to the plane. Since $\beta = 90.82°$ this slight misalignment between the c axis and the laboratory frame was ignored. In the plane of the leiteite flake, the long axis of the leiteite crystal corresponded to the *b* axis, and the *a* axis was at right angles to the long axis.

5.3 DESCRIPTION OF CRYSTAL STRUCTURE

Leiteite is monoclinic with space group $P2_1/c$ (C_{2h}^5) and four formula units per unit cell (a = 4.542, b = 5.022, and c = 17.597 Å) [27]. The structure consists of open Zn tetrahedral layer flanked on either side by single arsenite chains (Fig. 5.1). The [ZnO_4] tetrahedral share corners ($O_{(3)}$ and $O_{(4)}$) to form a checkerboard pattern. Similarly the arsenite groups also share corners ($O_{(1)}$ and $O_{(2)}$) to form chains. There are two distinct arsenite groups in the trigonal pyramidal geometry which alternate along the chain. Each As atom is thus connected to $O_{(1)}$, $O_{(2)}$, and either $O_{(3)}$ or $O_{(4)}$. $O_{(1)}$ and $O_{(2)}$ connect two As atoms and are termed bridging, while $O_{(3)}$ and $O_{(4)}$ connect As to Zn and thus are termed non-bridging with respect to As. The layers, connected by long As-O bonds, are stacked in the direction of *c*-axis. Positional parameters indicate all atoms are on general C_1 sites [27]. The non-bridging and bridging As-O bond lengths are 1.73 – 1.76 and 1.80 – 1.82 Å respectively.

5.4 RESULTS

5.4.1 X-ray diffraction

The natural leiteite flakes and its synthetic snow white powder were subjected to X-ray powder diffraction (Fig. 5.2). Although no impurities are observed in either pattern, confirming the absence of reinerite in the synthetic sample, there are relative intensity differences in the natural leiteite owing to the preferred orientation in the natural sample corresponding to the perfect (001) cleavage.

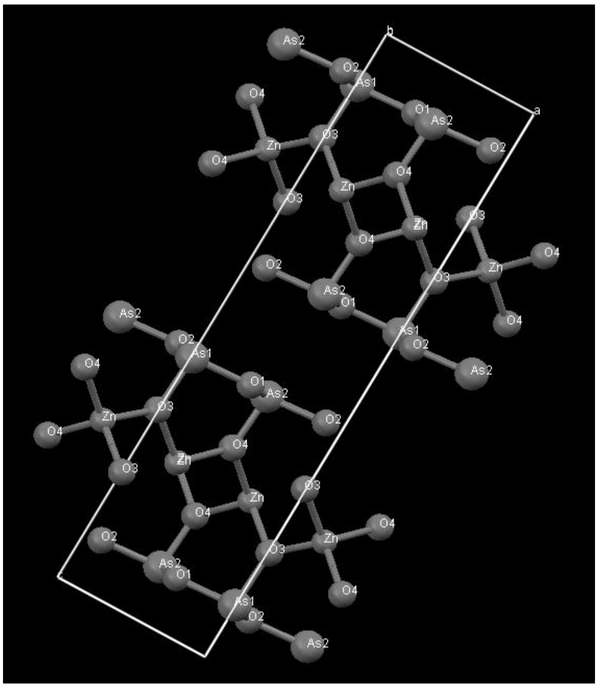

Fig. 5.1 – Model of the structure of leiteite

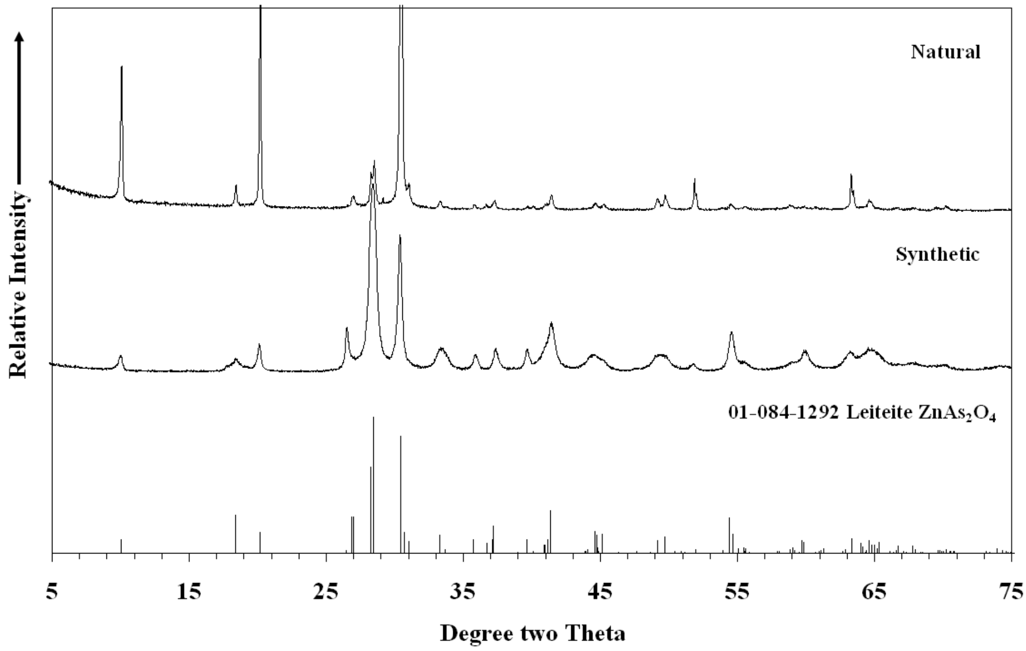

Fig. 5.2 – XRD pattern of natural and synthetic leiteite

5.4.2 Scanning Electron Microscopy

The SEM image of the natural leiteite is shown in (Fig. 5.3a). Synthetic leiteite images show dandelion-like spheres (Fig. 5.3b). On closer examination the spheres appear to be made of small flakes. A possible explanation for this occurrence is the fact that the flakes of the synthetic crystals had not had time to grow into the large flakes such as those that appear in the natural sample.

5.4.3 Raman Microscopy

5.4.3.1 *Factor Group Analysis*

The unit cell of leiteite is the primitive unit cell and it contains four formula units. Thus a primitive unit cell contains 28 atoms. The number of allowable modes is 81 consisting of $21A_g$ + $21B_g$ + $20A_u$ +$19B_u$. The analysis is represented in Table 5.1. The form of the polarisability tensor for C_{2h} crystals dictates that A_g modes are observed in the *aa*, *bb*, *cc*, and *ac* orientations and B_g modes in the *ab* and *bc* orientations. Thus it should be possible to assign a symmetry species to many of the Raman active modes.

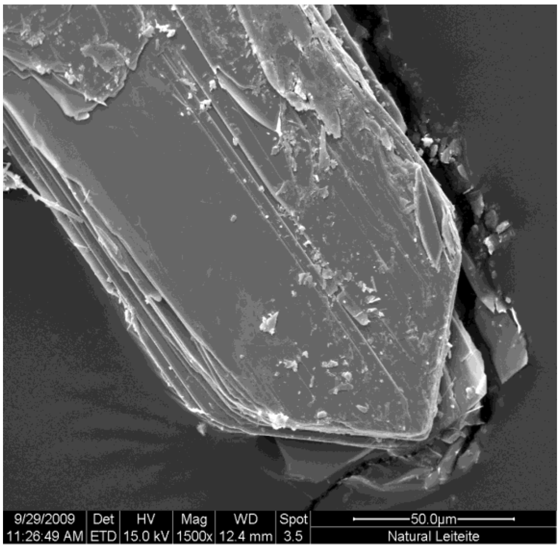

Fig. 5.3a – SEM micrograph of natural leiteite

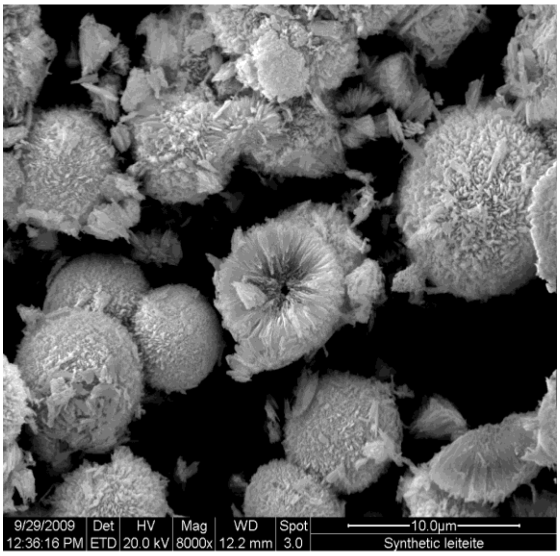

Fig. 5.3b – SEM micrograph of synthetic leiteite

C_1 site symmetry	C_{2h} crystal symmetry	Translation
21*A* (7 atoms x 3*A* on each atom)	$21A_g$	
	$21B_g$	
	$21A_u$	T_z
	$21B_u$	T_{xy}

Table 5.1 – Factor group analysis of leiteite

5.4.3.2 *Raman Spectra of Leiteite*

The Raman spectra of leiteite are shown in Figs. 5.4 to 5.10. Figs. 5.4 and 5.5 show the non-oriented Raman spectra of natural and synthetic leiteite respectively. Both spectra show bands at similar positions but some bands are broader in the synthetic specimen. Figs. 5.6 – 5.10 show Raman spectra of an oriented single crystal of natural leiteite. The intensities of the observed bands vary according to orientation allowing them to be assigned to either A_g or B_g modes as summarised in Table 5.2. A_g bands are generally the most intense in the CAAC spectrum, followed by ACCA, CBBC, and ABBA whereas B_g bands are generally the most intense in the CBAC followed by ABCA. The CAAC and ACCA spectra are identical, as are those obtained in the CBBC and ABBA orientations. Both cross-polarised spectra are identical.

After closer examination it was decided that the BACB and BAAB should not be used to determine band assignments. They are unreliable since they contain both A_g and B_g bands with intermediate intensities, for example bands at 169 (A_g), 181 (B_g), 201 (B_g), 207 (A_g), 258 (B_g), 270 (A_g), 305 (B_g), 370 (A_g), 550 (B_g), 603 (A_g), 651 (B_g), 764 (B_g), and 807 cm^{-1} (A_g) are all present in the above spectra. This is probably an indication of scrambling of the incident radiation, due to the biaxial nature of leiteite. Monoclinic crystals have one of the main optical directions (X, Y, and Z) of the indicatrix coincide with the *b* axis. The biaxial indicatrix is a triaxial ellipsoid containing the optical directions X, Y, and Z which are proportional to the refractive indices α, β, and γ respectively, listed in the order of decreasing ray velocity. Every section passing through the centre of this ellipsoid is an ellipse, except for two circular sections. The two directions normal to the circular sections are the optic axes which lie in the XZ plane [81]. No birefringence is shown when light moves along the optic axes because it encounters the circular sections which have a constant refractive index β and thus, from the point of view of the light travelling along the axis, the crystal will seem isotropic. The acute angle between the two optic axes is defined by 2V or the optic angle. Leiteite is biaxially positive, α =1.87, β=1.88, γ =1.98. Biaxial positive indicates that the axis that bisects the optic angle is the Z axis. Monoclinic crystals always have one if its principal optical directions (X, Y or Z) coincide with the *b* axis. In the case of leiteite this optical direction is Y. The angles between the *c* axis to Z and *a* axis to X are 10° and 11° respectively [82]. Light travelling along the *b* axis will not encounter circular sections and will therefore experience birefringence.

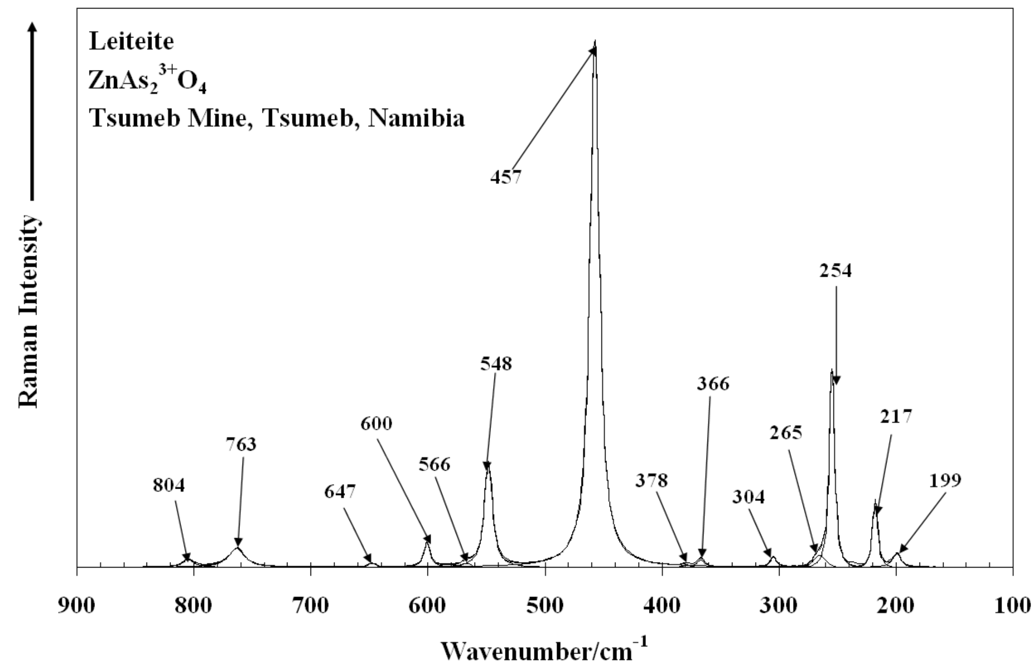

Fig. 5.4 – Raman spectra of natural leiteite in the 900 – 100 cm^{-1} region

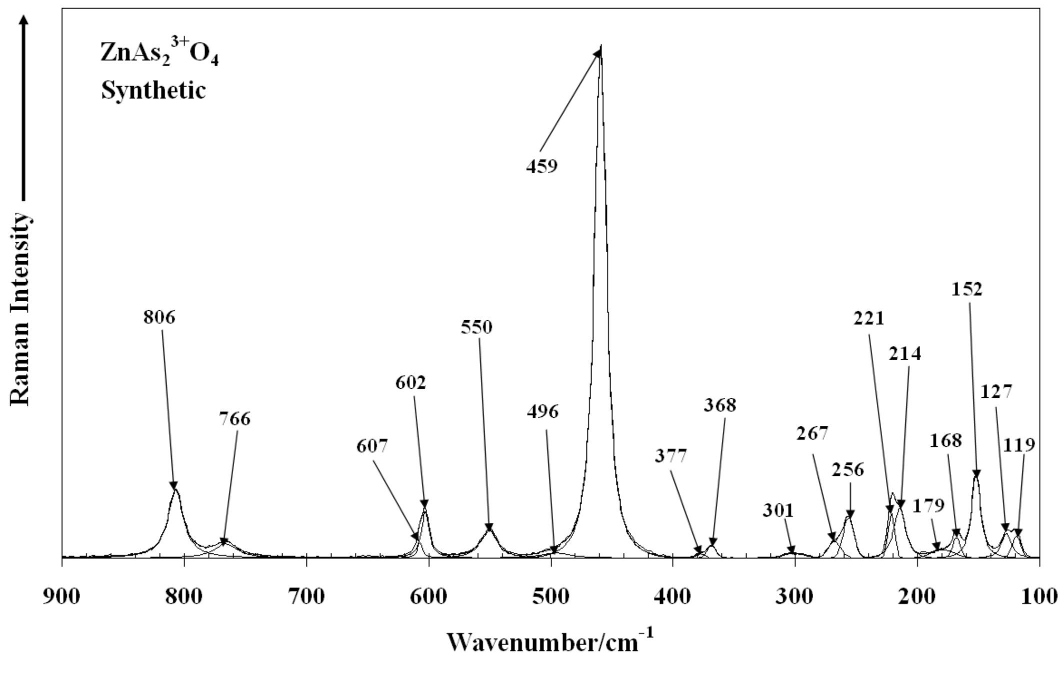

Fig. 5.5 – Raman spectra of synthetic leiteite in the 900 – 100 cm^{-1} region

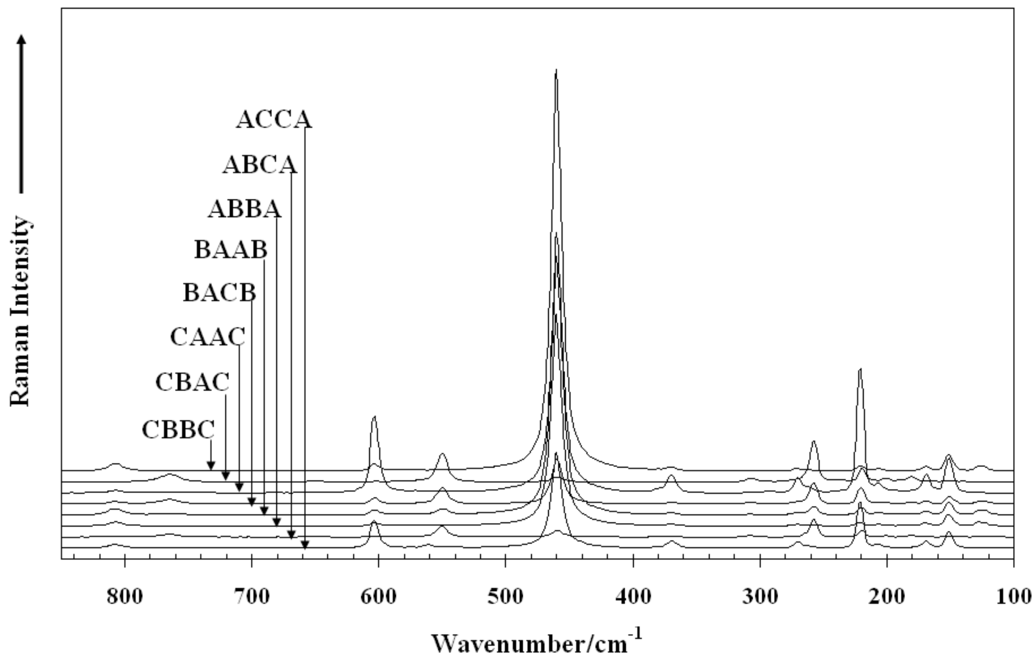

Fig. 5.6 – Raman spectra of the oriented single crystal of leiteite in the 900 – 100 cm^{-1} region

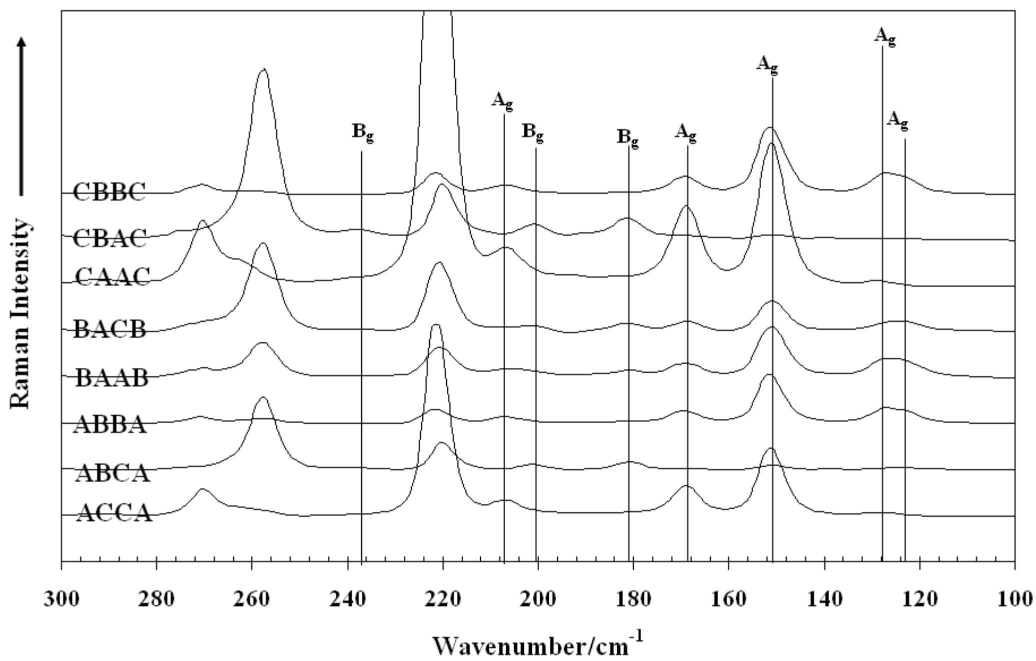

Fig. 5.7 – Raman spectra of the oriented single crystal of leiteite in the 300 – 100 cm^{-1} region

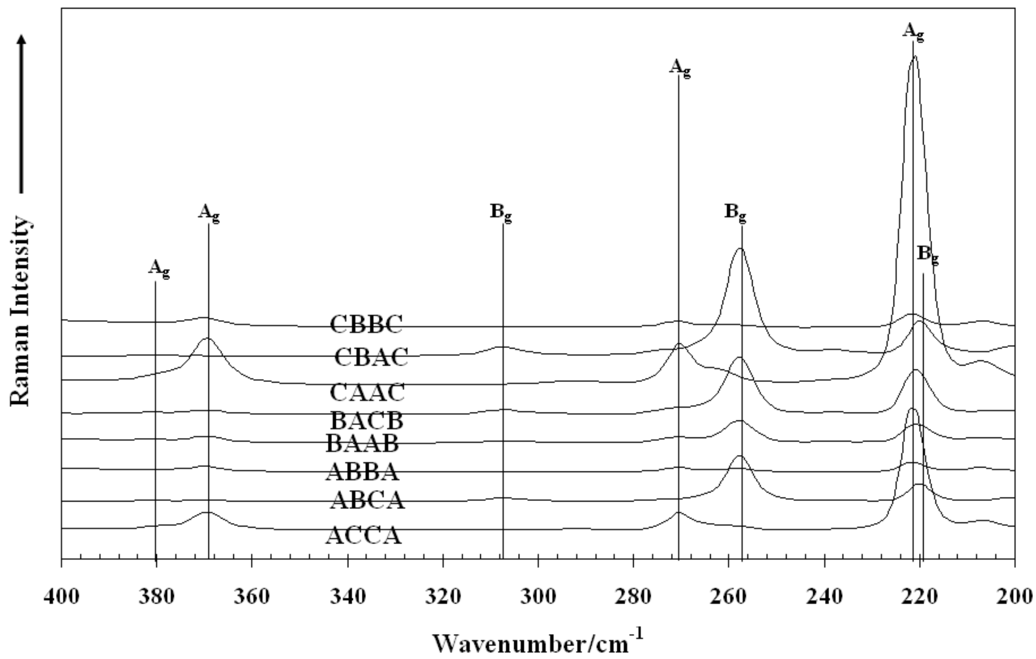

Fig. 5.8 – Raman spectra of the oriented single crystal of leiteite in the 400 – 200 cm^{-1} region

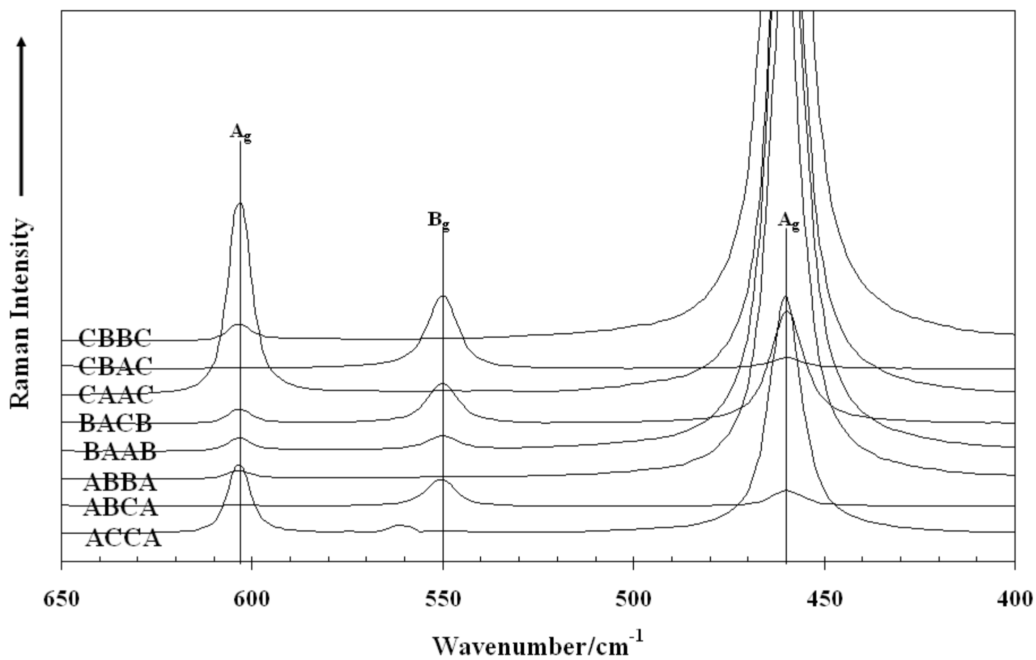

Fig. 5.9 – Raman spectra of the oriented single crystal of leiteite in the 650 – 400 cm^{-1} region

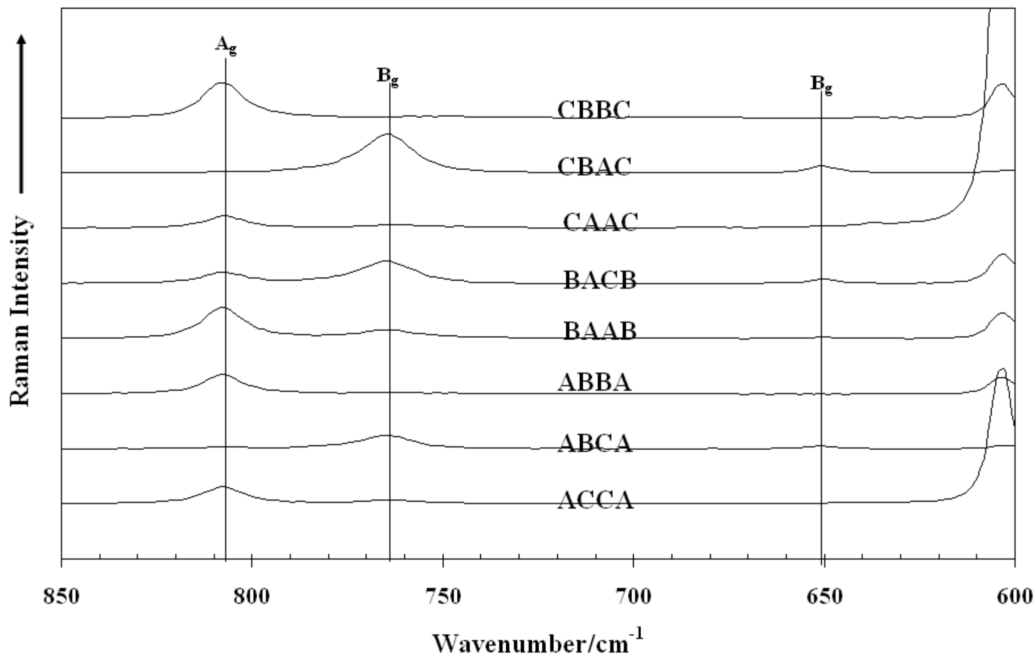

Fig. 5.10 – Raman spectra of the oriented single crystal of leiteite in the 850 – 600 cm^{-1} region

Band Position (cm^{-1})	Assignment
123	A_g
127	A_g
139	B_g
151	A_g
169	A_g
181	B_g
201	A_g
207	A_g
220	A_g
239	B_g
258	B_g
270	A_g
305	B_g
370	A_g
381	A_g
460	A_g
550	B_g
603	A_g
651	B_g
764	B_g
807	A_g

Table 5.2 – Assignments of the Raman bands

The infrared spectra of leiteite are provided in Fig. 5.11. Bands are observed at 794, 765, 641, 609, 558, 462, 377, 370 – 360, 264, 254, 216, and 205 cm^{-1}. Upon closer examination, it was found that most of the Raman bands have a closely-spaced partner in the infrared spectrum resulting from weak layer-layer coupling. This phenomenon is also observed in the spectra of the layered arsenite mineral claudetite As_2O_3 also of space group C_{2h}^5, which show each pair to contain either A_g-B_u or B_g-A_u members. By determining the mode of the Raman band, the mode of its infrared partner can be deduced, as summarised in Table 5.3.

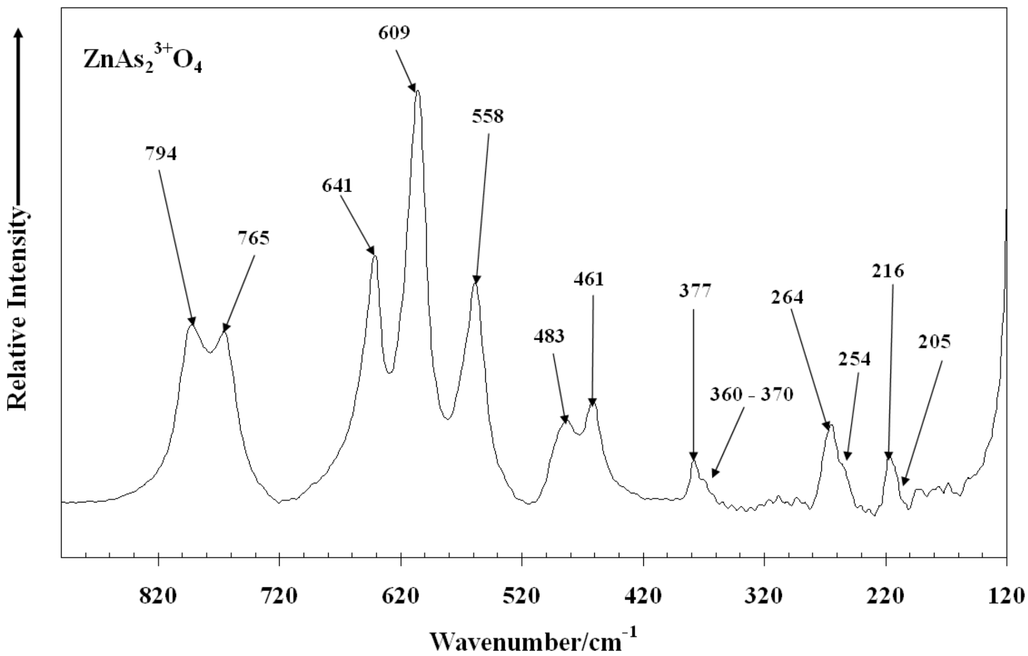

Fig. 5.11 – Infrared spectra of leiteite in the 900 – 120 cm^{-1} region

5.5 DISCUSSION

The presence of the polymeric chain of AsO_2 instead of an isolated vibrating unit limits the value of factor group analysis in assigning the various arsenite modes. Theoretically the stretching vibrations of the non-equivalent As-O bonds can be expected to give rise to 6A_g and 6B_g modes.

Raman	Assignment	IR	Assignment
201	A_g	205	B_u
207	A_g		
220	A_g	216	B_u
239	B_g		
258	B_g	254	A_u
270	A_g	264	B_u
305	B_g		
370	A_g	360 - 370	B_u
381	A_g	377	B_u
460	A_g	462	B_u
550	B_g	558	A_u
603	A_g	609	B_u
651	B_g	641	A_u
764	B_g	765	A_u
807	A_g	794	B_u

Table 5.3 – Comparison of the Raman and IR bands of leiteite

Since the arsenite groups are not isolated, instead forming infinite chains, the factor group analysis is performed as follows: 2 distinct As atoms x 3 non-equivalent As-O bonds x 4 formula units in a unit cell = 24 bands, which will split into 6A_g, 6B_g, 6A_u, and 6B_u. For the bridging As-O units 4A_g and 4B_g modes are expected but realistically only 2A_g and 2B_g can be observed due to the similarity of the bridging As-O bond lengths in the chain. Similarly even though there are two terminal As-O bonds, their bond lengths are identical, causing only 1A_g and 1B_g modes (out of the expected 2A_g and 2B_g modes) to be observed. The form of the polarisability tensor for C_{2h} crystals dictates that A_g modes are observed in the *aa*, *bb*, *cc*, and *ac* orientations and B_g modes in the *ab* and *bc* orientations. An A_g mode is simply caused by all four formula units in the unit cell vibrating in-phase, whereas in the case of a B_g mode the formula units across a mirror plane do not vibrate in-phase with each other.

Gout et al. [21] and Pokrovski et al. [22] associated broad bands around 520 and 380 cm^{-1} in concentrated aqueous As solutions to the formation of bridging As-O-As bonds. Theoretical studies by Tossell [18] and Tossell and Zimmermann [19] later assigned these vibrations to the symmetric ring breathing and deformation of $As_3O_3(OH)_3$. Loehr and Plane [17] assigned the region 750 – 790 cm^{-1} to stretches of terminal As-O. Keeping in mind that each vibration has an A_g and B_g component, some band assignments have been made on leiteite based on the oriented single crystal spectra and past literature. Bands at 650 (B_g), 600 (A_g), 550 (B_g) and 458 cm^{-1} (A_g) have been assigned to the stretching vibrations of the bridging As-O-As units, whereas bands at 763 (B_g) and 805 cm^{-1} (A_g) correspond to the stretches of non-bridging As-O. The deformation of the bridging As-O-As units may be found in the region 370 – 258 cm^{-1}.

The highly intense band at 458 cm^{-1} is assigned as the A_g manifestation of the symmetric stretch of the bridging bonds, which may be envisaged as a breathing motion [83] of the As-O-As unit propagating along the chain. An identical band was observed in the spectrum of claudetite [51,52]. The highly symmetric nature of this vibration explains the strong intensity of the band. An antisymmetric stretch may appear as the bridging bonds of one As atom expanding and the bonds belonging to an adjacent As atom contracting, and alternating in this way along the chain. The vibrations of the bridging bonds are unlikely to couple with the vibration of the terminal bonds because the terminal bonds are normal to the plane.

5.6 CONCLUSIONS

The A_g and B_g modes of leiteite $ZnAs_2O_4$ were successfully separated using Raman microscopy and an oriented single crystal. Factor group analysis predicted there should be 21 A_g + 21 B_g modes in the Raman spectrum, and in this study 13 A_g + 8 B_g modes were observed. The remaining bands may be accidentally degenerate due to the existence of similar bond lengths in the crystal structure. The assignment of bands in the mid and far IR spectra into A_u and B_u modes were aided by the presence of doublets, which arise due to weak interlayer coupling. Most of the Raman bands were found to have an IR partner; those that do not may simply have a weak partner that is masked by interference patterns in the far IR spectrum. Band assignments were made with respect to bridging and terminal As-O bonds. Bands at 650 – 450 and 380 – 250 cm^{-1} region were assigned to stretches and deformations of bridging As-O-As units respectively, and those in the 850 – 650 cm^{-1} region were assigned to terminal As-O vibrations.

Chapter 6

Single Crystal Raman Spectroscopy of Natural Schafarzikite $FeSb_2O_4$ from Pernek, Slovak Republic

6.1 INTRODUCTION

The single crystal Raman spectra of natural schafarzikite $FeSb_2O_4$ and the non-oriented Raman spectra of its Zn analogue and the related minerals, apuanite and trippkeite are presented. Schafarzikite is a meta antimonite mineral containing polymeric SbO_3 pyramids, belonging to the tetragonal space group $P4_2$/mbc (D_{4h}^{13}), a = 8.59 and c = 5.92 Å, Z = 4 [64,79,84]. Schafarzikite is isostructural to trippkeite $CuAs_2O_4$, which was the first mineral characterised to possess AsO_3 chain polymer [85], others being the synthetic compound $NaAsO_2$ [41,42] and the mineral leiteite $ZnAs_2O_4$ [27]. The crystal studied is dark brown with a metallic luster, and originated from Pernek, Malé Karpaty Mountains, Slovak Republic. It is also known to occur at Buca della Vena, Apuan Alps, Italy commonly associated with and closely related to other antimonites versiliaite $Fe^{2+}{}_2Fe^{3+}{}_4Sb_6O_{16}S$ and apuanite $Fe^{2+}Fe_4^{3+}Sb_4O_{12}S$ [29,86].

A comparison of chemical formulae may tempt one to conclude that leiteite, is isostructural to schafarzikite, and trippkeite when in fact this is not the case. In trippkeite and schafarzikite the cation is found in octahedral geometry surrounded with six O atoms, whereas in leiteite the cation is found in an open tetrahedral geometry. Leiteite also shows a different arrangement of the O atoms around the As; the bridging O connect only As together whereas for schafarzikite-like structures the so-called bridging O atom is bound to the cation in addition to bridging the two As atoms. A more detailed discussion can be found in the description of crystal structure section below.

There have been no known attempts on a single crystal study of schafarzikite previously, although a non oriented Raman and IR spectra of schafarzikite from the Pernek locality has been published [64]. To aid assignments, comparisons were made with the spectra of synthetic antimonites of manganese and nickel found in the literature [15]. Additionally $ZnSb_2O_4$ and trippkeite $CuAs_2O_4$ were synthesised and their Raman spectra recorded. Raman experiments were also performed on crystals of apuanite. The single crystal spectra enabled the assignment of modes to their symmetry.

6.2 EXPERIMENTAL

6.2.1 Mineral

Crystals of schafarzikite and apuanite were supplied by the National Museum in the Czech Republic and the Mineralogical Research Museum, respectively. Schafarzikite originated from the Pernek – Krížnica locality in the Malé Karpaty Mountains in the Slovak Republic, and apuanite from Buca della Vena in the Apuan Alps, Italy.

6.2.2 Synthesis of $ZnSb_2O_4$

$ZnSb_2O_4$ was prepared by adjusting the procedures to prepare $UO_2Sb_2O_4$ given by Albrecht-Schmitt et al. [14]. A mixture of 4 g of Sb_2O_3 and 1.12 g of ZnO (0.01375 mol) reacted hydrothermally in 20 mL H_2O at 180°C for 89 hours and cooled at a rate of 10°C/hour. The product appeared as white crystals dispersed in white powder, which is possibly undissolved Sb_2O_3. The two were separated manually after filtering from the mother liquor, washing several times with deionised water, and drying in an oven at 150°C overnight.

6.2.3 Synthesis of Trippkeite $CuAs_2O_4$

Trippkeite was synthesised following the procedures given by Pertlik [7]. 2.2 g of As_2O_3 and 0.88 g of CuO were reacted hydrothermally in 80 mL 1M CH_3COOH at 210°C for approximately 2 days and cooled naturally. The product appeared as dark green needles covered with red metallic wires. During filtration the product was washed several times with deionised water, and then dried at 110°C overnight.

6.2.4 Raman Microscopy

A crystal of schafarzikite was selected and placed on the corner of a perfect cube, aligned parallel to the sides of the cube using a very fine needle. In the plane of the schafarzikite flake, the long axis corresponded to the *c* axis, and the *b* axis was at right angles in the same plane as the long axis, and the axis at right angles to the *bc* plane is the *a* axis.

6.3 DESCRIPTION OF CRYSTAL STRUCTURE

Schafarzikite is tetragonal with space group $P4_2$/mbc (D_{4h}^{13}) and four formula units per unit cell. The crystal cell dimension are a = 8.59 and c = 5.91 Å [79,86]. The structural building blocks of schafarzikite consist of the octahedrally coordinated Fe and the Sb trigonal pyramidal geometry. Columns of edge-sharing FeO_6 octahedra run parallel to [001], on either side of which are chains of corner sharing $[SbO_3]^{3-}$ groups (Fig. 6.1). The symmetry of the SbO_3 pyramids is reduced to C_s from the ideal trigonal pyramid (C_{3v}) symmetry. Open channels parallel to [001] are also found within the framework [29]. There are two kinds of O atoms, $O_{(1)}$ and $O_{(2)}$. Each Sb is connected to 2 $O_{(1)}$ and 1 $O_{(2)}$ and each Fe is connected to 4 $O_{(2)}$ and 2 $O_{(1)}$. The above arrangement of O atoms is observed in a number of compounds with similar building blocks e.g. natural minerals trippkeite $CuAs_2O_4$ and apuanite $Fe^{2+}Fe_4^{3+}Sb_4O_{12}S$, and synthetic $ZnSb_2O_4$, $NiSb_2O_4$ and $MnSb_2O_4$. However it is unlike that found in other known antimonite compounds. Hirschle and Röhr showed synthetic antimonites of formulae $ASbO_2$ and $A_4Sb_2O_5$ where A = K, Rb, Cs to possess some O atoms which could definitively be characterised as bridging (those that connect only two Sb atoms together and no other atom) and others as terminal (those that connect the Sb atom to the other metal atom) [11]. In schafarzikite $O_{(1)}$ can be considered to be the bridging O, even though it also connects Sb to Fe, because it connects two Sb atoms together whereas $O_{(2)}$ does not. Positional parameters indicate that Fe occupy 4(*d*) or $D_2^{''}$, Sb and $O_{(2)}$ on 8(*h*) or C_s^{h}, and $O_{(1)}$ on 8(*g*) or $C_2^{''}$. The Sb-$O_{(1)}$ and Sb-$O_{(2)}$ bond lengths are 1.987 and 1.917 Å respectively. As in the case of the antimonites mentioned above, the distance from Sb to a terminal O atom is shorter than that to a bridging O atom.

The structure of apuanite can be derived from that of schafarzikite by substitution of every third Sb^{3+} in the chain with Fe^{3+}, and insertion of S^- in the open channels between the two Fe^{3+} atoms facing each other in adjacent chains. Furthermore two thirds of Fe^{2+} in the FeO_6 columns in schafarzikite are oxidised to Fe^{3+} in apuanite [29]. Unlike schafarzikite where there are two types of O atoms connected to Sb apuanite has three types of O atoms due to the substitution of every third Sb with Fe^{3+}. The terminal Sb-O bond is 1.975 Å, and the two bridging bonds, Sb-O-Sb and Sb-O-Fe, are 2.006 and 1.964 Å respectively.

The structure of trippkeite was first solved by Zemann [85] and later refined by Pertlik [28]. The cell dimensions of trippkeite are a = 8.59 and c = 5.57 Å [28], and As-$O_{(1)}$ and As-$O_{(2)}$ bond lengths are 1.814 and 1.765 Å respectively. Cu and As replace Fe and Sb respectively in the schafarzikite structure.

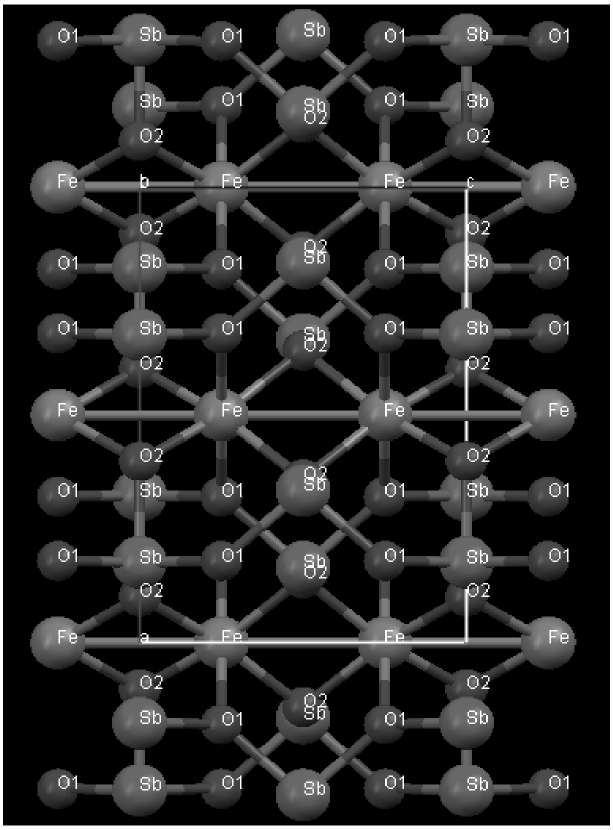

Fig. 6.1 – Model of the structure of schafarzikite

6.4 RESULTS

6.4.1 Results of X-ray Diffraction

The product of $ZnSb_2O_4$ synthesis was subjected to XRD analysis (Fig. 6.2a). The major phase of the white powder was Sb_2O_3, with minor phases of ZnO and $ZnSb_2O_4$, while that of the crystal was $ZnSb_2O_4$. Although the crystals were separated as best as possible from the powder, they were still covered in the powder causing the XRD pattern of the crystal to show lines corresponding to Sb_2O_3 and ZnO (both minor).

Fig. 6.2b shows XRD analysis of the product of trippkeite synthesis. Rietveld refinement showed the product to consist of approximately 65 % trippkeite, 20% CuO and 14% Cu_2O and negligible amounts of copper arsenates olivenite and cornubite.

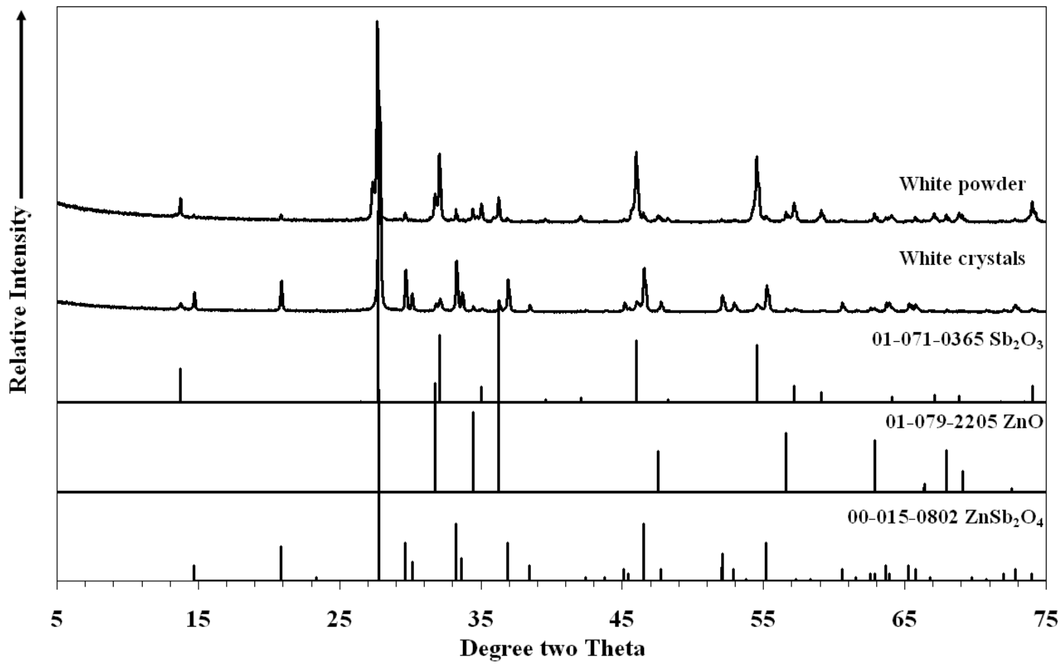

Fig. 6.2a – XRD patterns of the products formed in $ZnSb_2O_4$ synthesis

6.4.2 Scanning Electron Microscopy

The SEM images (Figs. 6.3a-b) of natural schafarzikite and synthetic $ZnSb_2O_4$ show the columnar nature of the compounds. The crystal size of greater than 100 microns and the flat surfaces are suitable for single crystal experiments. The SEM image (Fig. 6.3c) of synthetic trippkeite shows the majority of crystals to be 10 microns or less in size, with some being about 20 microns. While the size and the needle-like morphology of the crystals was well suited to single crystal Raman experiments, the aggregation of all crystals proved isolation of a single crystal difficult.

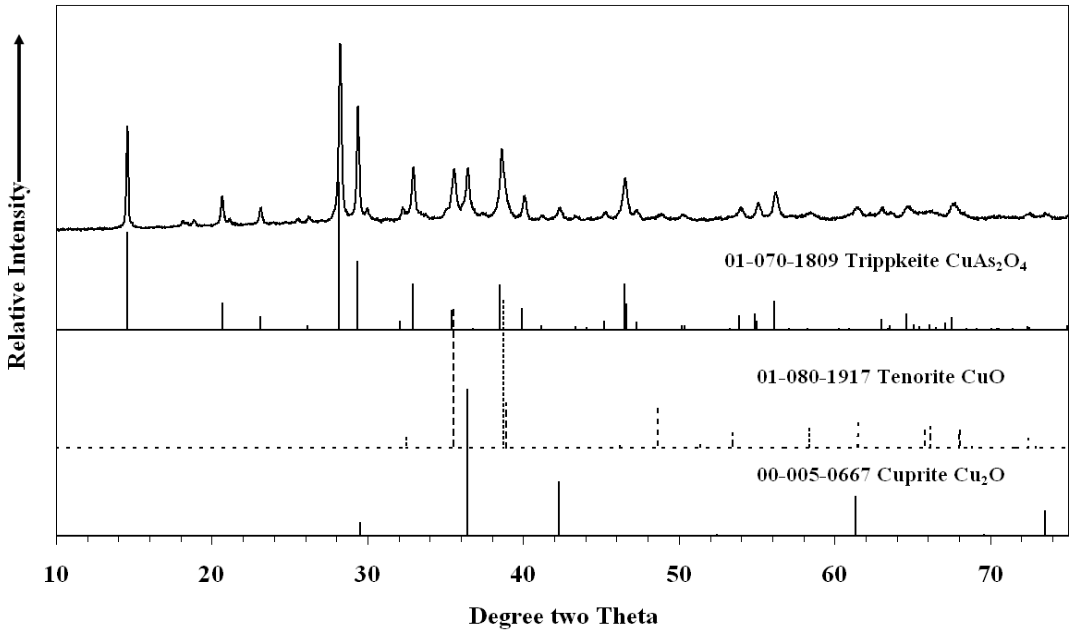

Fig. 6.2b – XRD patterns of the products formed in $CuAs_2O_4$ synthesis

6.4.3 Raman Microscopy

6.4.3.1 *Factor Group Analysis*

The unit cell of schafarzikite is the primitive unit cell and it contains four formula units. Thus a primitive unit cell contains 28 atoms. The number of allowable modes is 81 consisting of $5A_{1g}$ + $7A_{2g}$ (IA) + $7B_{1g}$ + $5B_{2g}$ + $3A_{1u}$

(IA) + $4A_{2u}$ + $5B_{1u}$ (IA) + $3B_{2u}$ (IA) + $9E_g$ + $12E_u$ (IA=inactive). The form of the polarisability tensor for D_{4h} crystals dictates that A_{1g} modes are observed in the *aa*, *bb*, and *cc* orientations, B_{1g} in *aa* and *bb*, B_{2g} in *ab*, and E_g in *ac* and *bc*. Schafarzikite is uniaxially positive (ω > 1.74, ε = n.d), with the only optic axis parallel to the *c* axis. The difference in velocities between the ordinary and extraordinary rays is 0 when light travels along the optic axis and maximum 90° away. In a tetragonal crystal such as schafarzikite α = ß = γ = 90° so light travelling along any axes other than *c* will experience birefringence, although weakly in this case since no scrambling of incident radiation is observed in spectra taken from *a* or *b* faces.

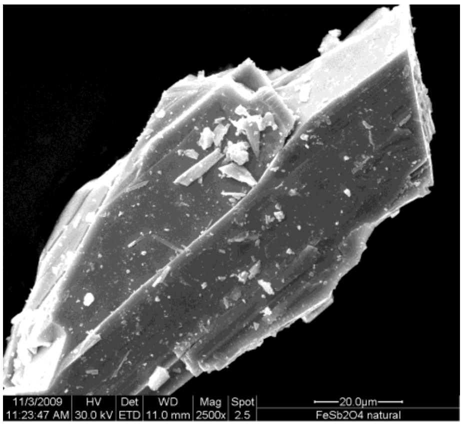

Fig. 6.3a – SEM micrograph of natural schafarzikite

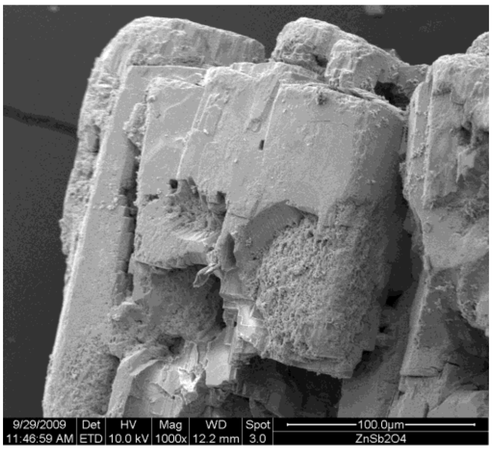

Fig. 6.3b – SEM micrograph of synthetic $ZnSb_2O_4$

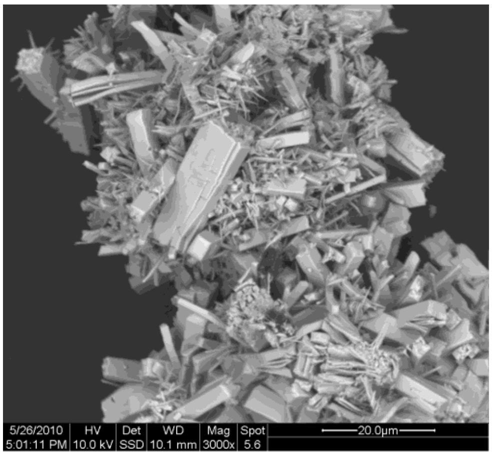

Fig. 6.3c – SEM micrograph of synthetic trippkeite

6.4.3.2 *Raman Spectra of Schafarzikite*

The Raman spectrum of non-oriented natural schafarzikite, as shown in Fig. 6.4, is characterised by a very intense band at 668 cm^{-1}, and medium bands at 295, 158, and 107 cm^{-1}. These peak positions compare favourably to those found previously [64] but peakfitting reveals several bands that were hitherto unreported, such as the small band at 709 cm^{-1} underlying the most intense band and weak bands at 478 and 188 cm^{-1}. Extra bands are also detected in the lower wavenumber range at 131, 119, and 107 cm^{-1}. Also unreported are two broad bands at 1388 and 1031 cm^{-1} (not shown) that are very weak relative to other bands. Although the band at 709 cm^{-1} is weak relative to the overlying band, its existence is not doubtful. Without the band at 709 cm^{-1}, there would be unaccounted intensity on the high wavenumber side of the strong band. A summary of peak positions found in the current work and previously are reported in Table 6.1.

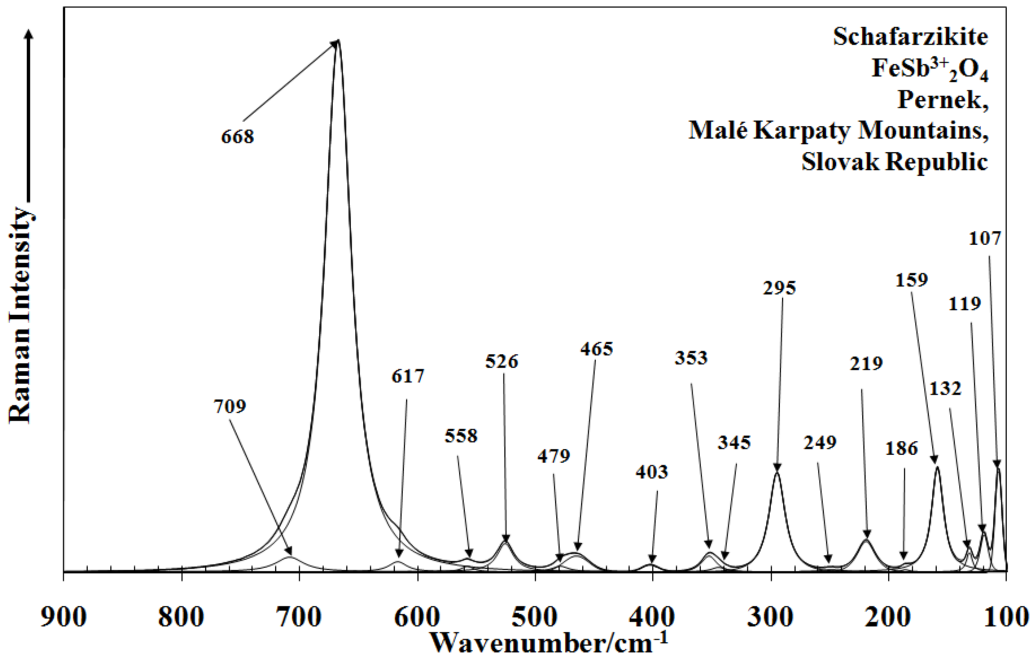

Fig. 6.4 – Raman spectrum of schafarzikite in the 900 – 100 cm^{-1} region

Schafarzikite			Schafarzikite [64]		Synthetic $ZnSb_2O_4$			Synthetic $NiSb_2O_4$ [15]		Synthetic $MnSb_2O_4$ [15]	
Centre	FWHM	%	Centre	Intensity	Centre	FWHM	%	Centre	Intensity	Centre	Intensity
1387	66.24	1.39									
1036	99.50	0.65									
709	28.96	2.31									
668	27.51	72.30	670	vs	676	21.73	36.42	685	m-s	670	vs
617	18.50	1.07	617	w-m	635	15.08	1.98	638	m	620	m
558	12.22	0.38			572	9.85	0.55	585	w	547	vw
526	16.81	2.54	524	w	528	10.72	0.76	535	w	527	m
479	17.20	0.53			482	9.75	0.57	486	w	474	m
465	24.97	1.46	467	w	454	11.65	2.55			465	m
403	16.40	0.41	405	w	414	12.59	2.25	421	w	399	w
353	15.09	1.06			360	9.58	0.71	360	m	350	m
345	14.65	0.41	348	m	338	15.61	2.36			345	m
295	16.30	3.67	295	s	298	11.28	30.05	309	vs	292	s
249	21.00	0.36	252	w-m	253	11.35	1.69	244	m	255	m
219	17.64	2.18	217	m	213	33.46	2.82			215	w
					208	8.44	4.08				
186	7.92	0.14			191	9.66	0.34	180	s	189	w-m
					177	10.35	0.71				
					164	7.89	6.56				
159	12.15	6.64	161	m-s	151	15.11	1.03	157	m	156	m
132	5.76	0.60			126	6.09	1.55	132	s	124	s
119	8.00	0.58			111	7.58	0.24	119	s	118	w
107	6.88	1.31			106	5.54	1.25			105	s

Table 6.1 – Peak-fitted results of Raman spectra of schafarzikite and $ZnSb_2O_4$ of the current study, and peak positions of Raman spectra of schafarzikite, $MnSb_2O_4$ and $NiSb_2O_4$ of prior literature

The oriented single crystal spectra of schafarzkite are displayed in Figs. 6.5a-b. Good separation between different symmetry species is observed. The band at 668 cm^{-1} is very strong in the CAAC and CBBC spectra, and its intensity does not diminish significantly in the ACCA spectrum and thus is assigned as A_{1g}, and the shoulder at 709 cm^{-1} is assigned to B_{1g} symmetry. The shoulder on the low wavenumber side, at 616 cm^{-1} is strongest in the CABC spectrum and is assigned to B_{2g} symmetry. The very weak bands at 557 and 402 cm^{-1} apparent in the peak-fitted spectrum cannot clearly be seen in Fig. 6.4 but on magnification it appears to be the most defined in ABCA and thus E_g is a possible symmetry for these modes. The bands at 525 and 465 cm^{-1} are assigned to B_{1g} and A_{1g}, respectively, the weak underlying band at 478 cm^{-1} is assigned to the B_{1g} The band around 350 cm^{-1} appears to have only one component in the peakfitted spectrum, but the oriented spectra clearly show two closely spaced bands at 352 (B_{1g}) and 344 cm^{-1} (B_{2g}). A band at 295 cm^{-1} which is strongest in CAAC and CBBC spectra is assigned to be of A_{1g} symmetry since its intensity is still significant in the ACCA spectrum.

6.4.3.3 *Raman Spectra of ASb_2O_4 (A = Zn, Ni, Mn)*

Synthetic antimonites isostructural to schafarzikite include those of zinc, nickel and manganese. The non-oriented Raman spectrum of $ZnSb_2O_4$ is shown in Fig. 6.6. Raman spectra of $NiSb_2O_4$ and $MnSb_2O_4$ may be found in Fig. 2 of [15]. The region 250 – 900 cm^{-1} is very similar in all the above MSb_2O_4 compounds and it may be concluded that this region corresponds to

Sb-O vibrations with minimal contribution from cations. The peak position and intensities of these compounds are summarised in Table 6.1. Spectra of $NiSb_2O_4$ and $MnSb_2O_4$ were not peak-fitted so the band list is not necessarily complete, for instance the bands at the highest wavenumber (685 and 670 cm^{-1} respectively) were not mentioned to have shoulders but the fact that they are broad makes the existence of shoulders possible as in the case of $ZnSb_2O_4$ and schafarzikite.

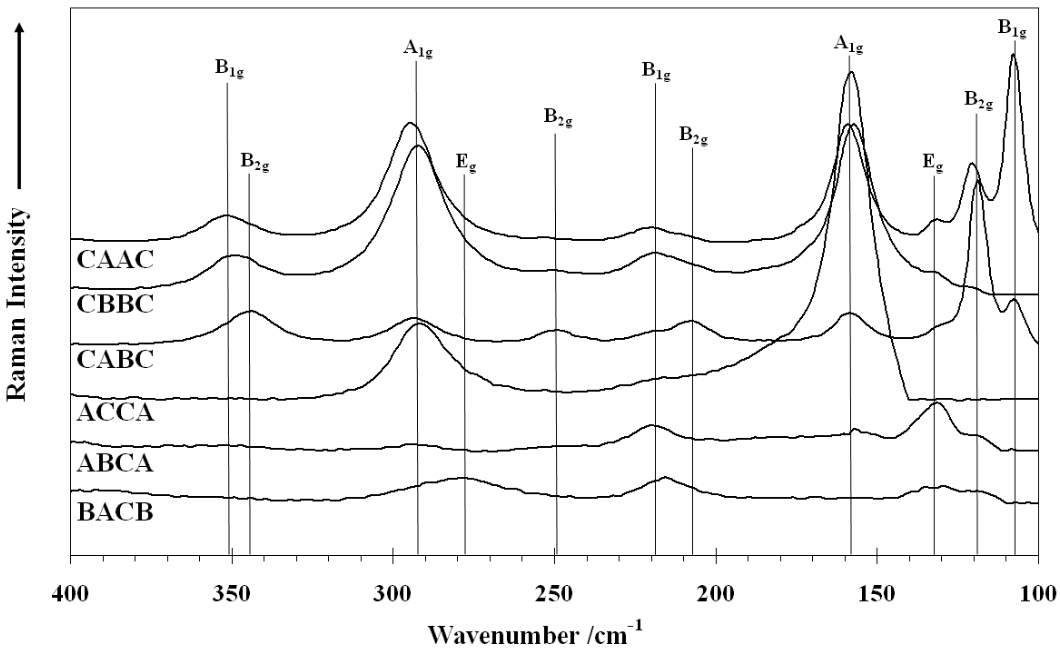

Fig. 6.5a – Oriented single crystal Raman spectrum of schafarzikite in the 400 – 100 cm^{-1} region

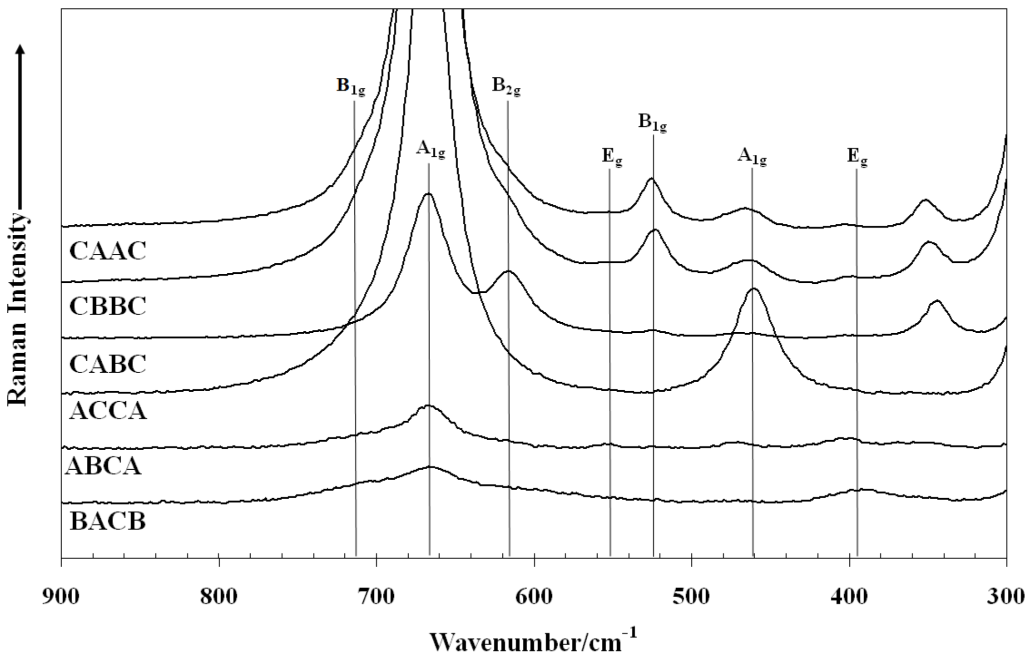

Fig. 6.5b – Oriented single crystal Raman spectrum of schafarzikite in the 900 – 300 cm^{-1} region

Single crystal study of $NiSb_2O_4$ and $MnSb_2O_4$ was not attempted due to insufficient crystal size. The synthesis of $ZnSb_2O_4$, however, did give suitable crystals and thus a single crystal study was attempted in order to compare its symmetry assignments to those of schafarzikite. It was found that the major band at around 670 cm^{-1} and its shoulder have the same symmetry as their corresponding bands in schafarzikite (675 cm^{-1}: A_{1g}, 634 cm^{-1}: B_{2g} in $ZnSb_2O_4$). Weak E_g bands were also observed in the spectra of both compounds at 550 – 570 cm^{-1} and 400 – 420 cm^{-1}. The A_{1g} symmetry of the band near 295 cm^{-1} is also replicated in $ZnSb_2O_4$.

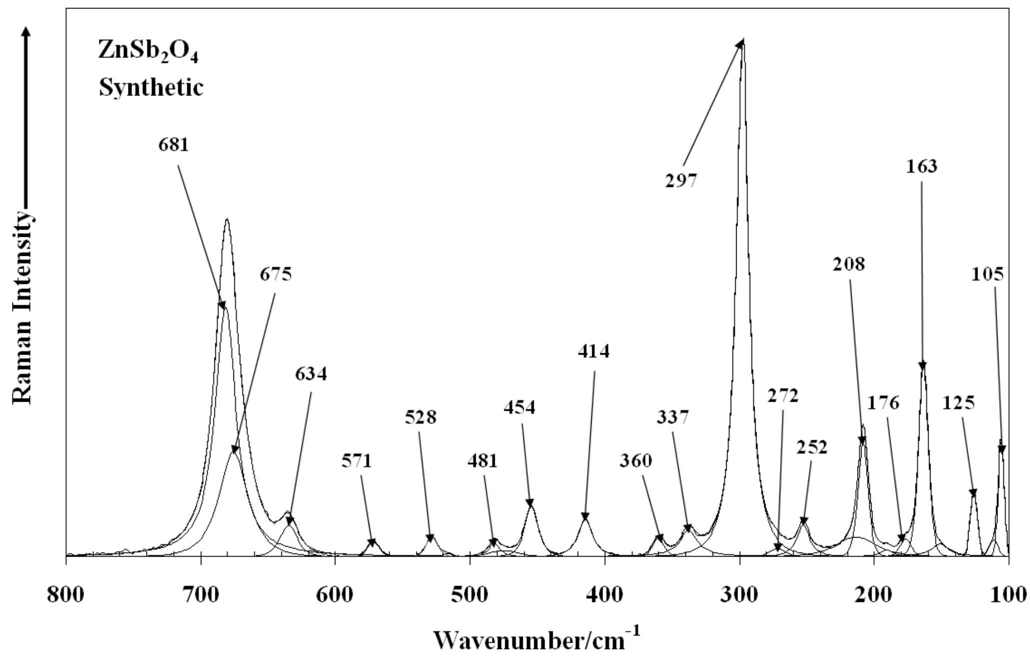

Fig. 6.6 – Peak-fitted Raman spectrum of $ZnSb_2O_4$ in the 800 – 100 cm^{-1} region

6.4.3.4 *Raman Spectrum of Apuanite*

An oriented single crystal study of apuanite gave poor mode separation. Poor optical qualities on some faces of the crystal led to weak Raman scattering in the spectra of these faces. Here a non-oriented Raman spectrum of apuanite is included (Fig. 6.7). Common features of apuanite and schafarzikite are the strong band around 660 cm^{-1} with two shoulders on either side, medium to strong band around 220 cm^{-1} and medium band in 150 – 170 cm^{-1} region. The high wavenumber shoulder is far more defined in this case compared to compounds of ASb_2O_4 structure where A is Fe, Mn, Ni, or Zn.

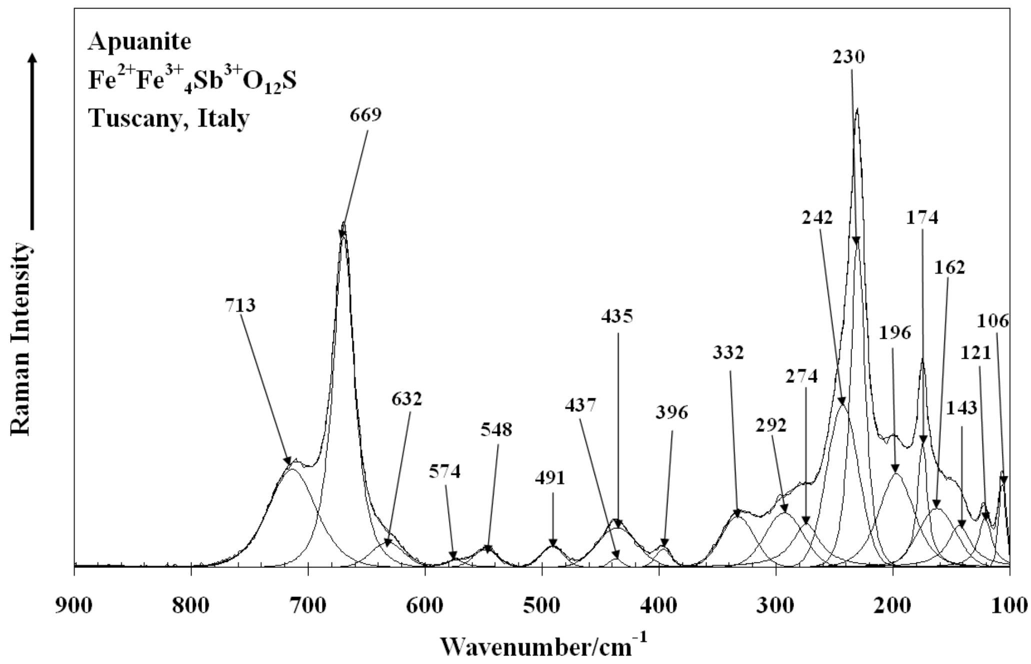

Fig. 6.7 – Peak-fitted Raman spectrum of apuanite in the 900 – 100 cm^{-1} region

6.4.3.5 *Raman Spectrum of Trippkeite*

To our knowledge trippkeite had not been studied previously by Raman spectroscopy. The non-oriented Raman spectrum of synthetic trippkeite (Fig. 6.8) is characterised by a medium band at 780 cm^{-1} and strong bands at 370 and 134 cm^{-1}. Peakfitting reveals a shoulder to the 780 cm^{-1} band at 810 cm^{-1}, and a second component to both strong bands at 367 and 139 cm^{-1}. The general appearance of the spectrum is similar to the spectrum of schafarzikite except that the bands are shifted to higher wavenumbers, as expected owing to the lighter As atom. Thus the relevant AsO_3 peaks lie above ~ 300 cm^{-1}. The fact that the crystals are small and aggregated made the isolation and manipulation of a single crystal difficult and thus oriented Raman experiments were incomplete. However the A_{1g} and B_{1g} bands were able to be assigned tentatively by examining the CC and AA/BB spectra, which were readily obtained due to the position of the crystal. The CC spectrum was obtained by aligning the plane of the laser parallel to the longest axis of the crystal, and the AA/BB spectrum by aligning the laser parallel to the axis at right angle to the longest axis. The medium band at 780 cm^{-1} is of A_{1g} symmetry, as well as the weak band at 496 cm^{-1} and the strong band at 371 cm^{-1}. The schafarzikite counterparts of the above bands are 667, 465, and 295 cm^{-1}. Those belonging to B_{1g} symmetry include the bands at 657, 539, and 421 cm^{-1} (525, 478, and 352 cm^{-1} in schafarzikite). It is observed that the order of the band symmetries in trippkeite match that of schafarzikite. The partial symmetry assignment of the bands in the trippkeite spectrum is presented in Table 6.2.

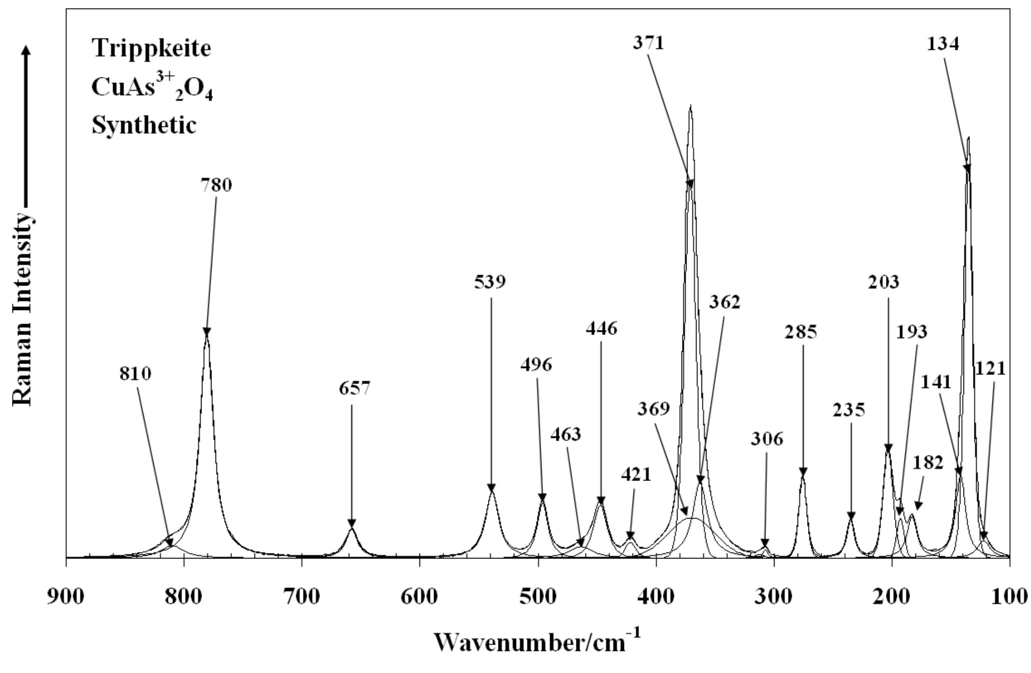

Fig. 6.8 – Peak-fitted Raman spectrum of trippkeite in the 900 – 100 cm^{-1} region

6.5 DISCUSSION

Out of the 35 allowable Raman modes of schafarzikite, 22 modes were observed consisting of $4A_{1g} + 5B_{1g} + 5B_{2g} + 4E_g$. Two types of Sb-O stretches can be expected in schafarzikite-like structures corresponding to terminal and bridging O atoms. The symmetry of SbO_3 is reduced from the ideal trigonal pyramid (C_{3v}) symmetry to C_s. Under C_{3v} symmetry the two Sb-O stretching modes have A_1 symmetry and E symmetry. On a C_s site A_1 modes translate to A' and E modes split to A' and A''. Sb and the terminal $O_{(2)}$ atoms are located on C_s sites, so theoretically the terminal Sb-O stretch should have A' symmetry and the bridging Sb-O stretches should give two components (A' and A''). Correlating this to a D_{4h} crystal system means that each A' vibration will have A_{1g}, B_{1g} and B_{2g} components in the Raman spectrum (A_{2g} is inactive; $2E_u$ modes are expected in the IR spectrum), and each A'' vibration will only have $2E_g$ components in the Raman spectrum (A_{1u}, B_{1u}, and B_{2u} are inactive; A_{2u} is expected in the IR spectrum). The splitting pattern is summarised in Table 6.3. If the factor group analysis of the ideal molecule applies to this particular case, the terminal Sb-O stretch should give rise to A_{1g}, B_{1g} and B_{2g} components whereas the bridging Sb-O stretch should give rise to A_{1g}, B_{1g}, B_{2g}, and $2E_g$ components.

In the Sb-O stretching region of schafarzikite the following modes are observed: 708 (B_{1g}), 667 (A_{1g}), 616 (B_{2g}), 557 (E_g), 525 (B_{1g}) and 465 cm^{-1} (A_{1g}). Symmetry considerations lead to the conclusion that one of the A_{1g} bands can be apportioned to the terminal Sb-O stretch and the other to the bridging Sb-O stretch. The same applies to the two B_{1g} bands.

A band near 700 cm^{-1} was observed by Hirschle and Röhr [11] in Sb^{3+} compounds with the $[Sb_2O_5]^{4-}$ units possessing two terminal O and one bridging O atoms, but not observed in compounds with infinite O_2-Sb-O_2 chains with no terminal O atoms. By analogy it seems likely that of the two A_{1g} and B_{1g} candidates for the terminal O stretch, the strong band at 667 cm^{-1} and the shoulder at 709 cm^{-1} are the more probable. Further supporting this assignment is the observation of bands near 700 and 650 cm^{-1} by Hirschle and Röhr [11] in Sb^{3+} compounds with the $[Sb_2O_5]^{4-}$ units (possessing two terminal O and one bridging O atoms), but not observed in compounds with infinite $O_{(2)}$-Sb-$O_{(2)}$ chains with no terminal O atoms.

Hirschle and Röhr [11] also described a band near 615 cm^{-1} in both types of compounds mentioned above, thus the shoulder at 616 cm^{-1} (B_{2g}) of scharfarzikite is assigned to a stretch of the bridging O unit. The relatively low wavenumber position of the E_g mode at 557 cm^{-1}, the B_{1g} mode at 525 cm^{-1}, and the A_{1g} mode at 465 cm^{-1} suggests that they are associated with bridging Sb-O.

As mentioned above theoretically there should be another B_{2g} and E_g bands, the former corresponding to stretches of the terminal Sb-O and the latter to those of bridging Sb-O. The E_g component may be too weak to be observed, or may be accidentally degenerate. The maximum number of five B_{2g} bands has been observed but there is a possibility of one or more of these being combination modes which may justify the expectation of one more B_{2g} band corresponding to a terminal Sb-O stretch.

The observation that terminal Sb-O stretch occurs at a higher wavenumber fits in well with the shorter terminal Sb-O bond length (1.917 Å) compared to the bridging Sb-O bond length (1.987 Å). Bands around 300 cm^{-1} have been previously assigned [11] to Sb-O deformations, thus the strong band at 295 cm^{-1} in schafarzikite is assigned likewise. The weak broad bands at 1388 and 1031 cm^{-1} are probably due to the combinations 667 + 708 cm^{-1} and 557 + 478 cm^{-1}, respectively. The partial band assignment are summarised in Table 6.2.

The spectrum of apuanite has some common features with the spectrum of schafarzikite, including the intense band around 660 cm^{-1} with two shoulders on either side. Using the same considerations applied to schafarzikite, bands in the region of 632 – 491 cm^{-1} are assigned to vibrations of the bridging Sb-O units, and the bands at 669 and 713 cm^{-1} are assigned to vibrations of the terminal Sb-O. A point of difference between the two spectra is the added intensity of the higher wavenumber shoulder compared to that observed in the spectra of other ASb_2O_4 compounds. As mentioned in the structural data, every third Sb is substituted by Fe causing each Sb to have three types of bonds: terminal Sb-O, bridging Sb-O-Sb, and Sb-O-Fe. The added intensity of the shoulder may be explained by the similar bond lengths of terminal Sb-O (1.975 Å) to Sb-O-Fe (1.964 Å), which causes the vibration of the latter to occur in the same region.

Schafarzikite		Trippkeite		Assignment
Band Position (cm^{-1})	Symmetry	Band Position (cm^{-1})	Symmetry	
709	B_{1g}	810	?	Sb(As)-O terminal
668	A_{1g}	780	A_{1g}	
617	B_{2g}			Sb(As)-O bridging
558	E_g			
526	B_{1g}	657	B_{1g}	
		539	B_{1g}	
465	A_{1g}	496	A_{1g}	
403	E_g			
353	B_{1g}	421	B_{1g}	Sb(As)-O deformation
345	B_{2g}			
295	A_{1g}	371	A_{1g}	
249	B_{2g}			
219	B_{1g}			
208	B_{2g}			Lattice modes
186	?			
159	A_{1g}			
132	E_g			
119	B_{2g}			
107	B_{1g}			

Table 6.2 – Peak positions, symmetry and assignment of the oriented single crystal spectra of schafarzikite and trippkeite

The spectra assignments of trippkeite are informed by the previous work by Röhr who conducted a Raman study on some analogous As^{3+} compounds [4], and a theoretical study by Tossell [18]. Rohr observed a band above 800 cm^{-1} observed in compounds of the formula $AAsO_2$ (A = Na, K and Rb) where the AsO_3 units are interconnected (each unit possessing one terminal O and two bridging O atoms). These bands were assigned to the vibration of terminal O. A theoretical study by Tossell [18] presented calculated wavenumbers of the dimeric molecules $As_2O(OH)_4$ and $[As_2O_5]^{4-}$, and assigned the terminal As-O stretches to bands in the 847 – 707 cm^{-1} region, and the bridging As-O stretches to bands in the 699 – 496 cm^{-1} region.

Therefore the bands at 780 and 810 cm^{-1} in trippkeite are assigned to stretches of terminal O atoms and stretches of the bridging O atoms are assigned to bands at 657 and 496 cm^{-1}. The rest of the assignments are listed in Table 6.2.

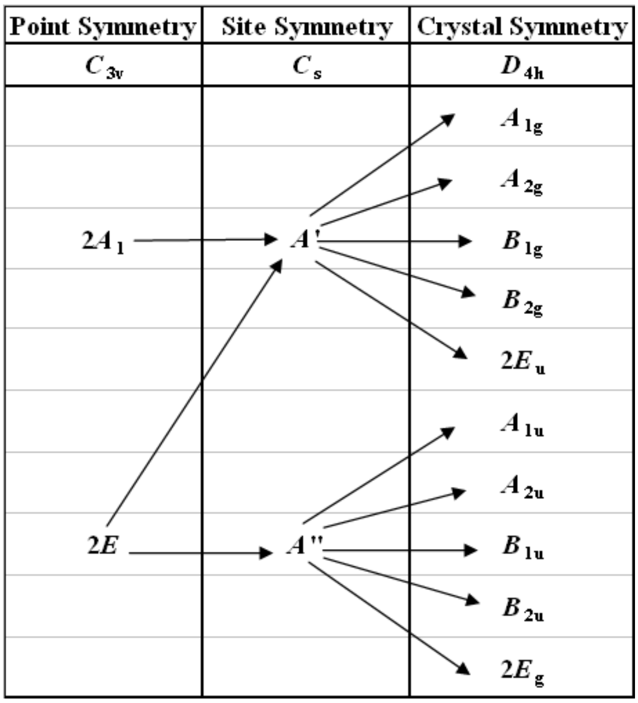

Table 6.3 – Factor group analysis of the SbO_3 group in schafarzikite

6.6 CONCLUSION

The spectra of the antimonite compounds are characterised by a strong band in the region 660 – 680 cm^{-1}, with shoulders on either side, and a band of medium to strong intensity near 300 cm^{-1}. Spectral comparison between the antimonite compounds in this study and those in prior literature shows that the strong band near 660 cm^{-1} corresponds to a stretch of the terminal Sb-O bond, whereas the shoulder at the lower wavenumber correspond to stretches of the bridging Sb-O bonds. Furthermore the bands in the region

616 – 450 cm^{-1} are also assigned to various vibrations of the bridging Sb-O units based on their symmetry modes. Bands around 300 cm^{-1} have also been assigned as Sb-O bends. The assignment above is confirmed by the shorter terminal Sb-O bond compared to bridging ones. The spectrum of trippkeite is dominated by a medium band at 780 cm^{-1} with a high wavenumber shoulder and a strong band at 370 cm^{-1} and has a similar general appearance to that of schafarzikite except that the bands are shifted to higher wavenumbers, as expected of the lighter As atom. Factor group analysis determined there should be $5A_{1g} + 7B_{1g} + 5B_{2g} + 9E_g$ in the Raman spectrum and in this study $5A_{1g} + 4B_{1g} + 5B_{2g} + 4E_g$ were observed. Good separation between different symmetry modes is observed.

Chapter 7

Single crystal Raman spectroscopy of natural brandholzite $Mg[Sb(OH)_6]_2 \cdot 6H_2O$, bottinoite $Ni[Sb(OH)_6]_2 \cdot 6H_2O$ and the polycrystalline Raman spectrum of mopungite $Na[Sb(OH)_6]$

7.1 INTRODUCTION

As part of a larger study of antimony bearing minerals [87,88] a preliminary investigation was previously published of the Raman spectrum of brandholzite [89], a mineral with the chemical formula of $Mg[Sb(OH)_6]_2.6H_2O$, which had been recently discovered in the oxidation zone of a body of stibnite in the Brandholz-Goldkronach area of Germany [44,90]. Since the earlier work a brandholzite crystal suitable for a single crystal study was obtained, which has facilitated the assignment of the various modes according to symmetry. Additionally a crystal of bottinoite $Ni[Sb(OH)_6]_2.6H_2O$ was also acquired, a mineral isostructural with brandholzite [90,92], suitable for single crystal work.

Both minerals belong to the trigonal space group C_3 (P_3) and Z = 6, with the crystallographic parameters a = 16.119, c = 9.868 Å (Brandholzite, M = Mg), and a = 16.026, c = 9.795 Å (Bottinoite, M = Ni). Brandholzite occurs as colourless plates whereas bottinoite is pale blue in colour; both have a vitreous appearance. Brandholzite and bottinoite are isotypic, containing isolated $[M(H_2O)_6]^{2+}$ and $[Sb(OH)_6]^-$ octahedra. The structure consists of two different alternating layers stacked along c axis; one contains only the $[Sb(OH)_6]^-$ octahedra, the other contains both $[M(H_2O)_6]^{2+}$ and $[Sb(OH)_6]^-$ octahedra in a ratio of 2:1. The $[Sb(OH)_6]^-$ hydroxyls form external hydrogen bonds that bind the layers together and the aqua ligands of the $[Mg(H_2O)_6]^{2+}$ form both inter and intra layer hydrogen bonds.

The vibrational spectra of minerals of this type can be largely understood in terms of the internal modes of the two ions involved, for brandholzite and bottinoite these are the more or less independent vibrations of coordination octahedra of $[M(H_2O)_6]^{2+}$ and $[Sb(OH)_6]^-$. To aid the task of teasing out the relative contribution of each ion to the spectra, density field theory (DFT) was applied to the isolated ions and the IR and Raman spectrum calculated. In addition a third mineral, mopungite, the sodium salt of $[Sb(OH)_6]^-$, was investigated. Mopungite comprises of hydrogen bonded layers of $[Sb(OH)_6]^-$ octahedra linked within the layer by Na^+ ions. Although Siebert reported infrared spectra of $Na[Sb(OH)_6]$ in an earlier study of synthetic hydrated antimonates and metaantimonates [34], the Raman spectrum of mopungite has not been previously published. This paper presents the single crystal data for the minerals brandholzite and bottinoite and makes band assignments according to symmetry and type. Although a single crystal of mopungite was not available for this study the non-aligned Raman spectrum is reported here and used to support the assignments made with consideration of the DFT calculations of the theoretical spectra and current literature.

7.2 EXPERIMENTAL

7.2.1 Minerals

Crystals of brandholzite originated from Krížnica mine, the Pernek deposit, the Malé Karpaty Mountains, western Slovakia, Slovak Republic and were kindly supplied by the National Museum, Prague. Crystals of bottinoite and mopungite were supplied by The Mineralogical Research Company.

Bottinoite originated from Ramsbeck Mine, Dornberg, Sauerland, Germany and mopungite from Le Cetine Mine, Siena Province, Tuscany, Italy.

7.2.2 Raman Microscopy

A single crystal of each mineral was selected and placed on the corner of a perfect cube, aligned parallel to the sides of the cube using a very fine needle. The *a* and *b* axis are not readily identifiable in the specimen under study. Fortunately it is not necessary to separate *a* from *b* in order to classify the modes according to their symmetry, either *a* or *b* or a mixed *ab* axis will suffice. This mixed *ab* axis will be referred to as the *a* axis for convenience and is accessed by placing the crystal flat under the microscope. Optically, brandholzite and bottinoite are uniaxial with a very small difference in the two refractive indices in each crystal (0.001 for brandholzite and 0.005 for bottinoite). The optical axis is parallel to the *z* axis so birefringence is not an issue in any case. By placing the crystal on its side and aligning the polarisation plane of the laser perpendicular to the crystal plate and the analyser parallel, the CC (*A*) spectrum can be measured. Rotating the plane of the laser gives the CA spectrum

7.2.3 DFT Calculations

Calculations were performed using the Gaussian 03 program [72] and the GaussView3.0 (Gaussian, Inc.,Wallingford, CT) front end, running on an SGI Origin 3000 supercomputer. The wavenumbers of the fundamental modes were calculated using density field theory (DFT) with B3-LYP method and a 6-31G(d) basis set for Mg, H and O atoms and Lanl2dz with diffuse functions of Check et al., [93] for Sb. No scaling factor was applied. Raman intensities were calculated from the Gaussian activities based on 633 nm excitation.

7.3 DESCRIPTION OF CRYSTAL STRUCTURE

Brandholzite and bottinoite belong to the trigonal space group C_3 and Z = 6, with the crystallographic parameters a = 16.119, c = 9.868 Å (Brandholzite, M = Mg), and a = 16.026, c = 9.795 Å (Bottinoite, M = Ni). Their structures comprise nearly regularly shaped, isolated $[M(H_2O)_6]^{2+}$ and $[Sb(OH)_6]^-$ octahedra arranged in two alternating layers stacked successively along the c axis. One layer contains only antimony; the second layer comprises Mg and Sb octahedra in a ratio of 2:1. The Sb hydroxyls form external hydrogen bonds that bind the layers together and the aqua ligands of the Mg form both inter and intra layer hydrogen bonds.

Mopungite belongs to the tetragonal space group C_{4h} and Z = 4, a = 8.029, c = 7.894 Å. Its structure was first given by Schrewelius [65] and refined by Asai [43]. The $[Sb(OH)_6]^-$ octahedra are also nearly regular with the sodium ions found in the interstices. All OH groups are involved in hydrogen bonding extending throughout the whole crystal.

7.4 RESULTS

7.4.1 Raman Microscopy

7.4.1.1 *Factor Group Analysis*

The unit cell (C_3) of brandholzite and bottinoite is the primitive unit cell containing six formula units. Six of the 12 Sb octahedra in the Bravais cell populate C_3 sites, the same point group symmetry as the crystal. The six remaining Sb^{5+} ions and two Mg^{2+} ions occupy general sites. This makes for very a complicated factor group analysis. The prediction of 269*A* + 269*E* modes provides little insight into band assignments. Although six of the Sb sites have higher symmetry, the fact that the Sb octahedra all have similar bond lengths and angles [44] means the bands are strongly overlapped. Although not occupying such a multiplicity of sites (just two) a similar argument can be made for the $[M(H_2O)]^{2+}$ ions.

Mopungite belongs to the tetragonal space group C_{4h} and Z = 4, *a* = 8.029, *c* = 7.894 Å. Its structure was first given by Schrewelius [65] and refined by Asai [43]. The primitive cell of mopungite contains four formula units, giving 165 modes in total comprising $18A_g + 18B_g + 18E_g$ Raman active modes, $23A_u + 23E_u$ IR active modes and $24B_u$ inactive modes. Single crystal experiments of mopungite were not attempted due to the polycrystalline nature of the sample.

Although the predicted multitude of low symmetry modes renders the FGA approach of limited value in terms of assigning the spectrum, it should never-the-less be possible to assign a symmetry species to many of the

Raman active modes by examining the single crystal spectra. The form of the polarisability tensor for C_3 crystals dictates that only *A* modes are active in the CC spectrum, both *A* and *E* modes are active in the AA spectra; and that *E* modes only are active in the cross polarised AC spectra. Figs. 7.4 – 7.7 show the single crystal Raman data of brandholzite and bottinoite. Modes observed only in the CC and/or AA spectra have been labelled *A*, while modes observed only to occur in the AC spectra and the AA spectra have been labelled *E*. Good mode separation was observed in both brandholzite and bottinoite with most modes showing the same orientation in both minerals as to be expected since they are homologous. The symmetry assignments have been given in Table 7.1.

7.4.1.2 *Raman Spectra*

Synthetic crystals of $Mg[Sb(OH)_6]_2.6H_2O$, $Ni[Sb(OH)_6]_2.6H_2O$, and $Na[Sb(OH)_6]$ have been subjected to infrared spectroscopy in the past and published by Balicheva and Roi [37]. Franck has also published infrared spectra of $Na[Sb(OH)_6]$ along with other hexahydroxyantimonates [36]. No Raman study, however, has been attempted on any of the above minerals or their synthetic analogues, except for our preliminary study of brandholzite [89].

The non-aligned Raman spectra of the three minerals are shown together for comparison purposes in Fig. 7.1. Calculated band positions and intensities for isolated $[Sb(OH)_6]^-$ and $[Mg(H_2O)_6]^{2+}$ ions are also shown in Fig. 7.1, second from bottom and bottom respectively, in bar graph style where the height of the bar indicates the calculated band intensity. Calculated wavenumbers for the OH stretching modes are overestimated owing to the lack of hydrogen bonding in the isolated ion model. The peak positions for the $[Sb(OH)_6]^-$ ion (Fig. 7.1D) below 1600 cm^{-1} correspond reasonably well with spectrum of mopungite (Fig. 7.1C). Contributions from the $[M(H_2O)_6]^{2+}$ ion in the spectra of brandholzite (Fig. 7.1A) and bottinoite (Fig. 7.1B) can be distinguished by comparing the two spectra with mopungite. These differences are discussed in later sections. Suffice to say for now that the theoretical spectrum of $[Mg(H_2O)_6]^{2+}$ poorly correlates with these observed differences, probably due to the fact that interlinking hydrogen bonds were not modelled in the DFT calculations and the predominance of H_2O bands in the spectral contribution from the Mg octahedron. The Raman spectra are shown in further detail in Figs. 7.2 and 7.3.

7.5 DISCUSSION

7.5.1 OH stretching

The OH region of the three minerals follow roughly the same contour but the relative intensity of mopungite is significantly lower (Fig. 7.1). This indicates that the OH regions of brandholzite and bottinoite are dominated by the relatively strong H_2O modes of the $[M(H_2O)]^{2+}$ ions, despite the 2:1 ratio in favour of the $[Sb(OH)_6]^-$ octahedra. According to Balicheva and Roi [37], IR bands above 3400 cm^{-1} are attributable to H_2O ligands involved in hydrogen bonding with adjacent H_2O ligands, whereas those at lower wavenumbers correspond to the H_2O ligands involved in stronger hydrogen bonding with the OH group of Sb-OH. Thus bands occurring at 3550 cm^{-1} in brandholzite and 3510 cm^{-1} in bottinoite, which are absent in the mopungite spectrum, can be associated with the interactions between $[M(H_2O)_6]^{2+}$ ions. Accordingly, the intense broad band at 3337 cm^{-1} in brandholzite and 3368 cm^{-1} in bottinoite can be associated with the $[M(H_2O)_6]^{2+}$ ion with stronger $[Sb(OH)_6]^-$ interactions. The sharp band at 3423 cm^{-1} on the high wavenumber side of the OH profile in mopungite appears to be matched by bands of similar appearance at 3466 cm^{-1} in brandholzite and 3458 cm^{-1} in bottinoite. Therefore these bands most likely arise from vibrations of the $[Sb(OH)_6]^-$ moiety.

DFT calculations suggest the totally symmetric OH stretch occurs at the highest wavenumber in that ion. In the oriented crystals (Fig. 7.4) this mode showed *E* symmetry and so is tentatively assigned to the out of phase mode of the Sb-OH symmetric stretch. The band at 3055 cm^{-1} in mopungite may either be a result of stronger hydrogen bonding between the SbOH-HOSb groups across the layers of the dioctahedral minerals or it could be shifted to lower wavenumbers due to the effect of the interstitial Na^+ ion.

Brandholzite		Bottinoite		Assignment
Band Position(cm^{-1})	Symmetry	Band Position(cm^{-1})	Symmetry	
105	*E*	105	*E*	Lattice modes
114	*E*	115	*E*	
122	*E*	125	*E*	
130	*A*	146	*E*	
140	*A*			
190	*A*			
207	*A*	207	*E*	
		229	*E*	
233	*A*	236	*A*	
252	*A*	255	*A*	
282	*A*	282	*A*	Sb-O deformations
		286	*A*	
299	*A*	299	*E*	
		303	*A*	
317	*E*	318	*E*	M-O stretch
332	*A*	337	*A*	Sb-O deformations
347	*E*	350	*E*	
355	*A*	361	*A*	
502	*E*	501	*E*	
525	*E*	516	*E*	Sb-O stretches
576	*A*	576	*A*	
604	*A*	600	*A*	
618	*A*	618	*A*	
630	*A*	630	*A*	
729	*A*	735	*A*	
1058	*A*	1045	*A*	OH in-plane deformation
1078	*E*	1081	*E*	
1163	*A*	1164	*A*	
1340	*A*			Combination band (617 + 729 cm^{-1})
1644	*E*			H_2O deformation
3180	*A*			OH stretches
3228	*A*	3223	*A*	
3305	*A*	3291	*A*	
3354	*E*	3345	*E*	
3400	*A*	3393	*A*	H_2O stretch
3467	*E*	3458	*E*	OH stretch
3550	*E*	3511	*E*	H_2O stretch

Table 7.1 – Peak positions, symmetry and assignment of the oriented single crystal spectra of brandholzite and bottinoite

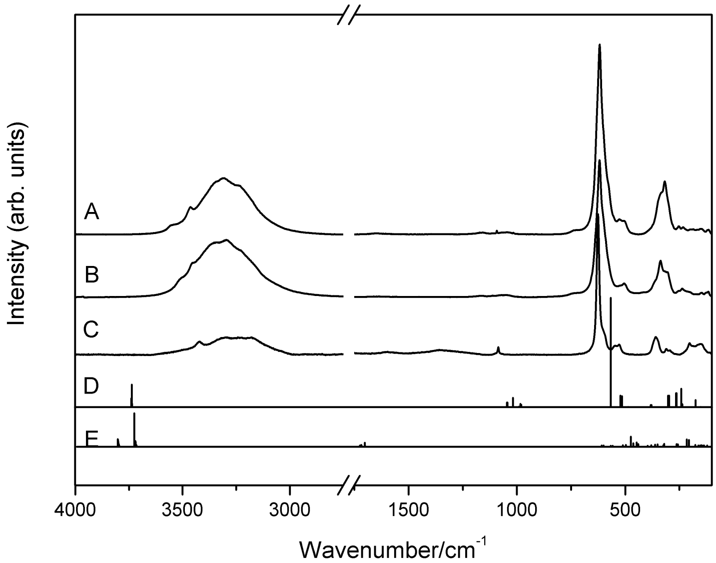

Fig. 7.1 – Non aligned Raman spectra of brandholzite (A), bottinoite (B), and mopungite (C), and calculated spectra of isolated $[Sb(OH)_6]^-$ (D) and $[Mg(H_2O)_6]^{2+}$ (E)

7.5.2 OH deformation

Brandholzite shows weak bands around 1644 (*E*) (Fig. 7.5), assigned to δ(H_2O), and at 1340 cm^{-1} (*A*), assigned to a combination band (617 + 729 cm^{-1}). The δ(H_2O) band was too weak to be observed in the bottinoite spectrum. The in-plane OH deformation bands δ(OH) are predicted to occur near 1000 cm^{-1} according to the DFT calculations and these are observed at 1058 (*A*), 1078 (*E*), and 1163 cm^{-1} (*A*) in brandholzite and 1045 (*A*), 1081 (*E*), and 1164 cm^{-1} (*A*) in bottinoite. The weak but sharp band at 1086 cm^{-1} in the spectrum of mopungite (Fig. 7.1C) is due to the symmetric stretch of some carbonate contamination which also accounts for some weak broad bands near 1385 cm^{-1}. The δ(OH) of mopungite was not observed directly due to the interference of the contaminant bands and the overall weakness of the spectrum. A weak band of *A* symmetry is observed near 730 cm^{-1} in the spectra of brandholzite and bottinoite. A band in this position in the IR spectrum was assigned to non-planar OH deformations, γ(OH), by Balicheva and Roi [37], who thought it arose from interaction of OH groups belonging to neighbouring octahedra. In the theoretical spectrum of $[Sb(OH)_6]^-$, γ(OH) is predicted to occur some 400 cm^{-1} lower, at approximately 300 cm^{-1}. Although the DFT calculation are of an isolated $[Sb(OH)_6]^-$ octahedron it is difficult to justify such a large shift to accord with the Balicheva and Roi assignment. Also it is interesting to note that the 730 cm^{-1} band is not seen in the mopungite Raman spectrum, which implies it originates from the $[M(H_2O)]^{2+}$ moiety, though its presence may be masked by noise from fluorescence and the overall weakness of that spectrum.

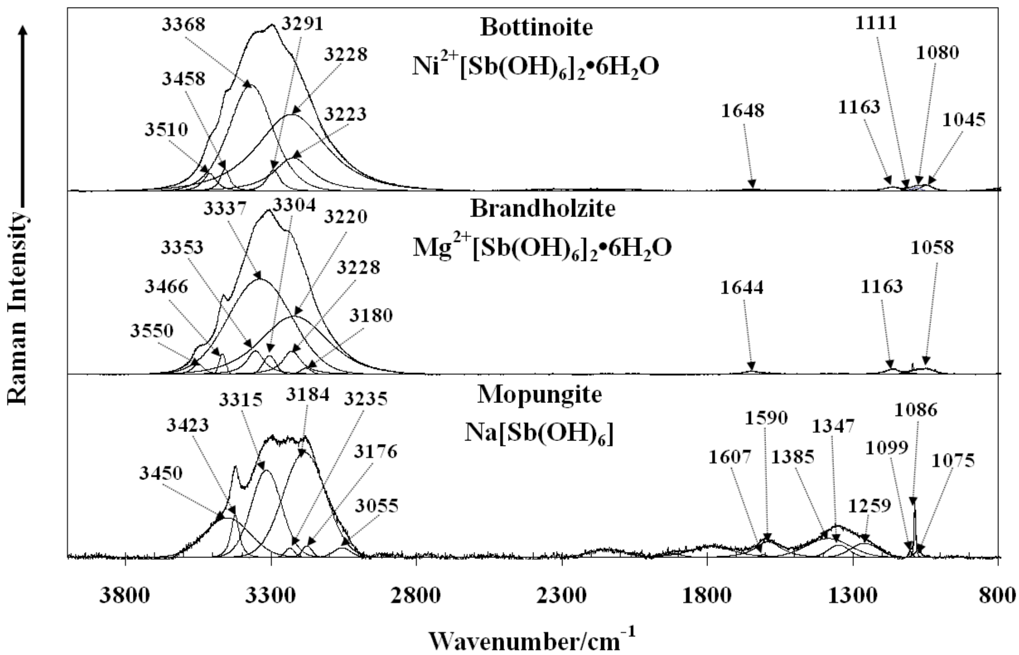

Fig. 7.2 – Bandfitted spectra of brandholzite, bottinoite, and mopungite in the 3800 – 800 cm^{-1}region

7.5.3 SbO stretching

The 800 – 400 cm^{-1} spectral region of the two di-octahedral minerals are virtually identical and there are also many parallels between these spectra and that of mopungite. In addition the theoretical band positions are in broad agreement with experimental values in this region. The predominant band is a broad peak centred at 617 cm^{-1} (brandholzite) and 618 cm^{-1} (bottinoite). Peak fitting reveals that there are four components present at 630, 617, 604, and 576 cm^{-1}, in brandholzite and at 630, 618, 599, and 575 cm^{-1} in bottinoite (Fig. 7.3). Towards the lower wavenumbers of this region there are two weak broad bands (525 and 502 cm^{-1} for brandholzite, and 516 and 501 cm^{-1} for bottinoite). The 680 – 500 cm^{-1} region has been associated with stretches of the Sb-O octahedra [36] and this is confirmed by the DFT calculations of the $[Sb(OH)_6]^-$ ion. Treating the Sb-O octahedra as a pseudo O_h group gives 3 stretching vibrations, the so-called $\upsilon_1(A_{1g})$, $\upsilon_2(E_g)$ and $\upsilon_3(F_{1u})$ modes. Six of the 12 Sb octahedra in the Bravais cell populate C_3 sites, the same point group symmetry as the crystal. For these moieties FGA predicts that A_{1g} modes transform to A symmetry; E_g to E, and the F_{1u} modes split into $A + E$ modes. Two further non-equivalent Sb octahedra are centred on general sites and so for these moieties there is a potential for each of the three stretching modes to split into A and E modes. It seems reasonable to assign the most intense band (approx 617 cm^{-1}) to υ_1. DFT calculations suggest that $\upsilon_2(E_g)$ of the Sb-O octahedra occurs as much as 50 cm^{-1} to lower wavenumber from υ_1. Thus the bands at 576 and 525 cm^{-1} are candidates for this assignment. However inspection of Fig. 7.6 reveals that only the 525 cm^{-1} band is of the correct symmetry species (E). The theoretical wavenumber for $\upsilon_3(F_{1u})$ is just to the high wavenumber side of υ_1. The band at 630 cm^{-1} is therefore assigned as the *A* symmetry manifestation of this mode (Fig. 7.6), which can be denoted as in-phase Sb-O antisymmetric stretch.

A similar picture can be painted for mopungite, where the Sb atom occupies a C_i site in a C_{4h} crystal. In this instance, FGA predicts $\upsilon_1(A_{1g})$ splits into A_g + B_g + E_g modes, all Raman active, $\upsilon_2(E_g)$ gives rise to six Raman active bands ($2A_g + 2B_g + 2E_g$) and $\upsilon_3(F_{1u})$ potentially gives rise to six IR active bands ($3A_u + 3B_u$ (IA) + $3E_u$). Although it was not possible to conduct a single crystal study of mopungite some inferences can be made by comparing mopungite with the brandholzite and bottinoite above. The dominant band at 625 cm^{-1} is most probably the υ_1 mode. This is slightly higher than found in bottinoite or brandholzite. The bands at 526 cm^{-1}, and possibly the band at 546 cm^{-1}, are manifestations of υ_2. The υ_3 of Sb-O is not predicted to occur in the Raman spectrum of mopungite but distortions to the octahedron may be giving rise to some intensity near 650 cm^{-1}.

Although there are many parallels, there are also some significant differences in this spectral region between mopungite and the other two minerals. The profile of the strong Sb-O stretch is considerably narrower in mopungite. Band fitting data suggests that the extra band width is due to a broad band centred at 604 cm^{-1} (brandholzite). DFT calculations for the $[M(H_2O)_6]^{2+}$ ion do not predict bands in this region so it seems likely that this is the Sb-O symmetric stretch of the Sb-O on general sites. The band near 501 cm^{-1} in both brandholzite and bottinoite is absent in mopungite, suggesting it is a band of the $[M(H_2O)_6]^{2+}$ moiety.

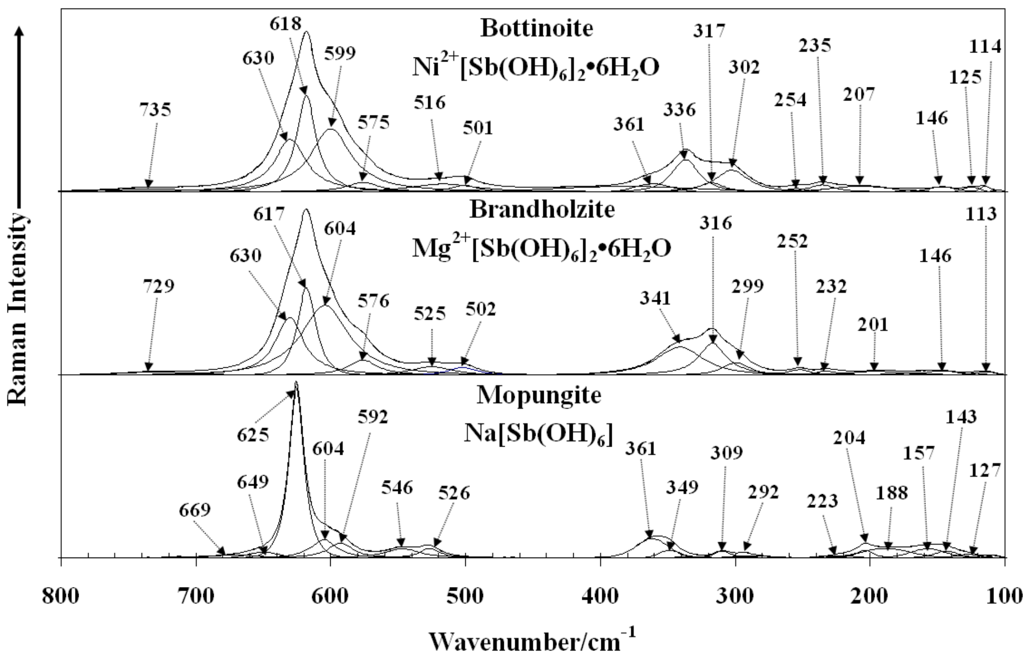

Fig. 7.3 – Bandfitted spectra of brandholzite, bottinoite, and mopungite in the 800 – 100 cm^{-1}region

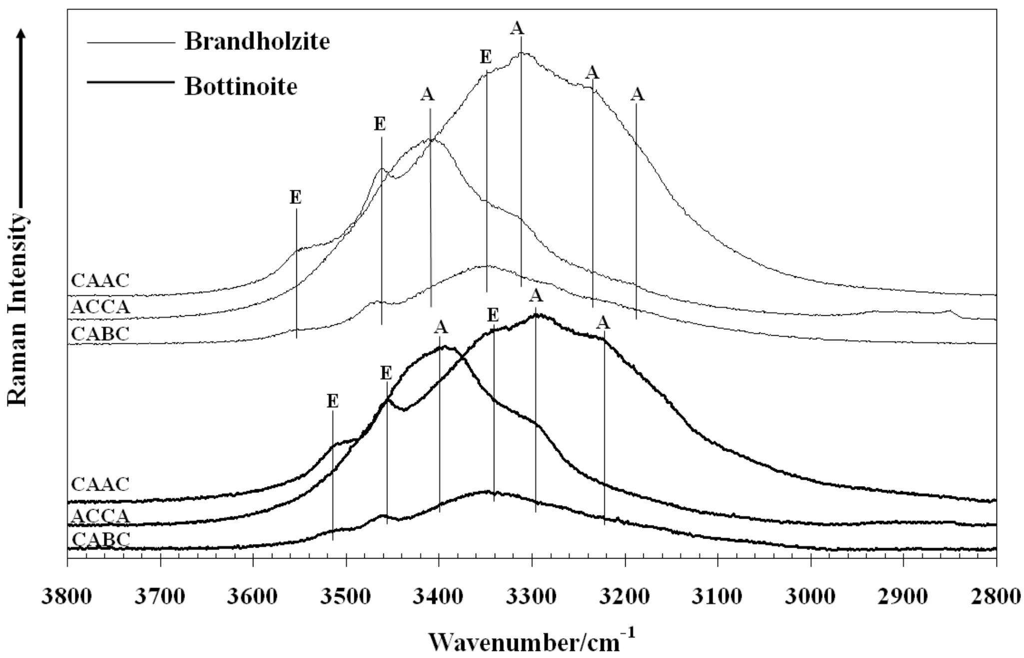

Fig. 7.4 – Oriented single crystal spectra of brandholzite and bottinoite in the OH stretch region

7.5.4 Low wavenumber region

The theoretical spectrum of $[Sb(OH)_6]^-$ shows a number of bands around 300 cm^{-1} due to γ(OH), discussed briefly above, and also Sb-O deformations or δ(SbO) which include $\upsilon_4(F_{1u})$ and $\upsilon_5(F_{2g})$ modes of the Sb-O octahedra. Each of these modes splits into A + E modes. In light of the DFT calculations it seems likely that γ(OH) also contributes here. The band at 315 cm^{-1} in brandholzite and bottinoite is entirely absent in mopungite which suggests that the $[M(H_2O)]^{2+}$ modes contribute significantly to that band. The possibility of multiple moieties contributing to bands in this area complicates assignment of regions to a certain moiety. However, with the exception of the band at 315 cm^{-1}, the three minerals appear to have bands in common in the region of ~360 – 290 cm^{-1} (Figs. 7.3 and 7.7). Therefore this region was assigned to the Sb-O deformations, agreeing with the assignment made by Franck [36] of the IR spectrum.

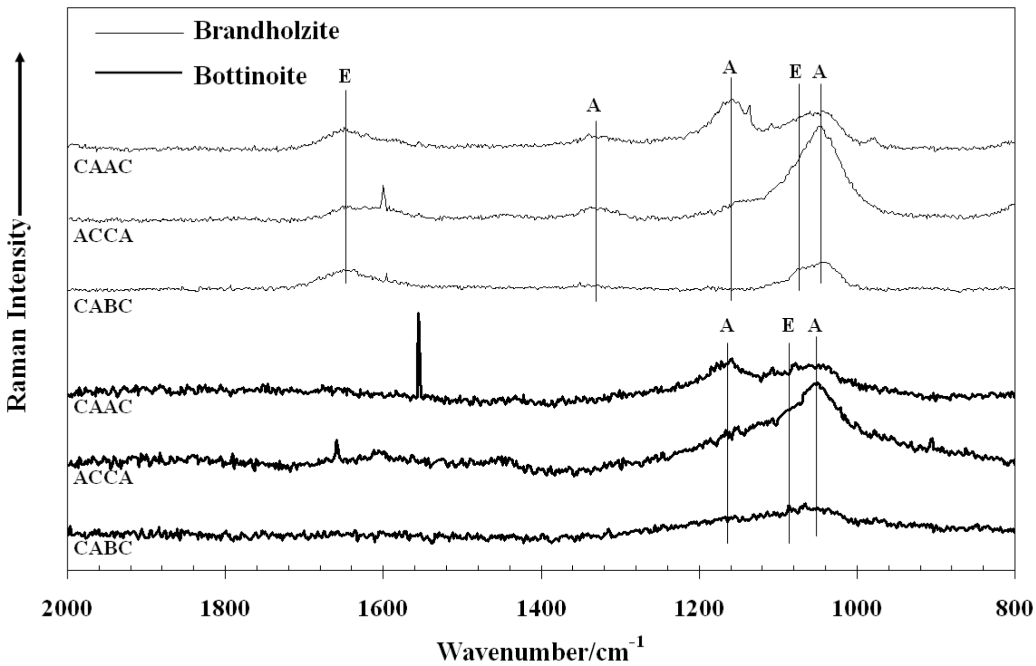

Fig. 7.5 – Oriented single crystal spectra of brandholzite and bottinoite in the OH deformation region

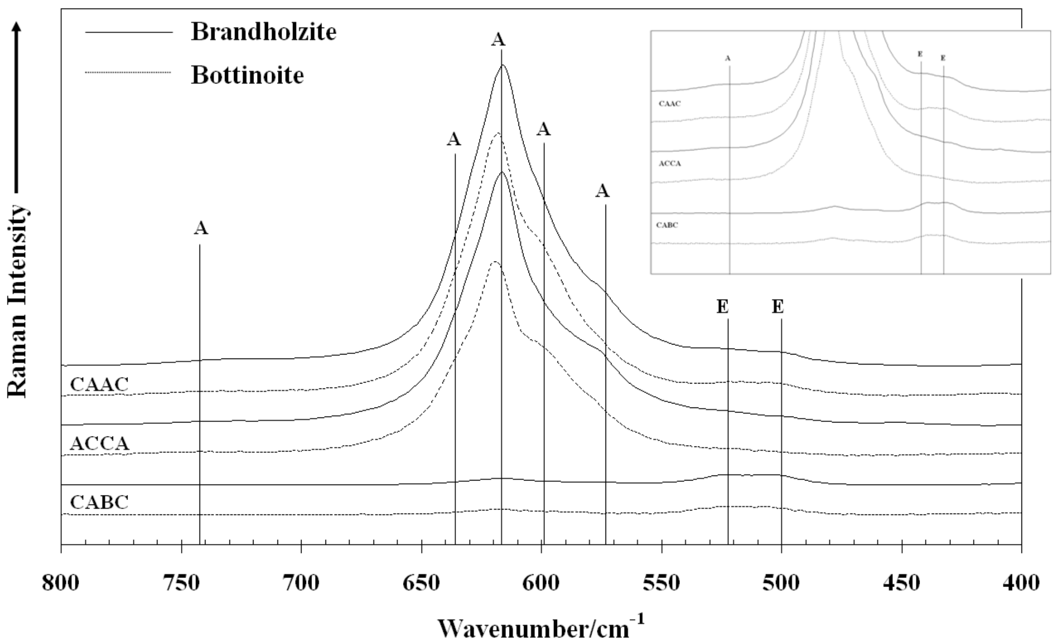

Fig. 7.6 – Oriented single crystal spectra of brandholzite and bottinoite in the SbO stretch region

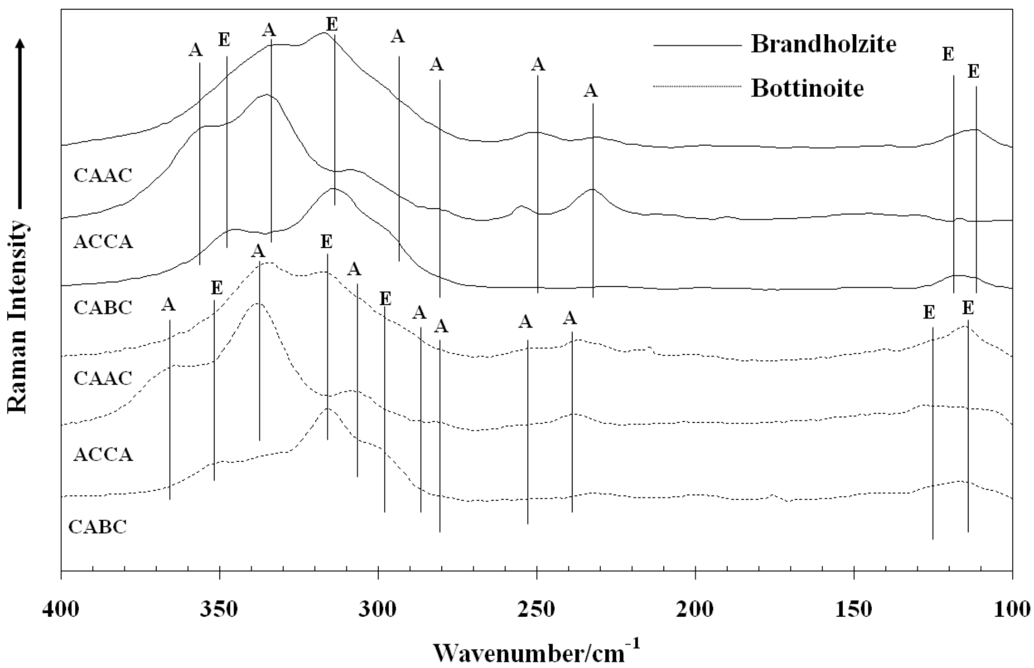

Fig. 7.7 – Oriented single crystal spectra of brandholzite and bottinoite in the low wavenumber region

7.6 CONCLUSIONS

The Raman spectra of brandholzite and bottinoite, and the non-aligned Raman spectrum of mopungite, are dominated by the Sb-O symmetric stretch near 620 cm^{-1} and show many similarities despite mopungite lacking the $[M(H_2O)_6]^{2+}$ ion of the other two minerals. Major differences were noted in the OH stretching region which had greater relative intensity and the presence δH_2O near 1620 cm^{-1} as would be expected by the additional presence of the $[M(H_2O)_6]^{2+}$ ion. The Sb-O symmetric stretch showed a broader profile in the di-octahedra minerals owing to the multitude of non-equivalent sites that are occupied by the $[Sb(OH)_6]^-$ ion. Density field theory calculations pertaining to the free $[Mg(H_2O)_6]^{2+}$ ion were of limited use due to the dominance of OH modes in the spectrum and the lack of hydrogen bonding in the free ion model. However the calculated spectrum of the $[Sb(OH)_6]^-$ ion showed reasonable agreement and proved a useful aid in assignments. The single crystal data spectra showed good mode separation and enable the majority of the bands to be assigned a symmetry species of *A* or *E*.

Chapter 8

Conclusions and Future Work

8.1 CONCLUSION SUMMARY

A number of natural arsenite, antimonite, and hydrated antimonate minerals were studied mainly by single crystal Raman spectroscopy. Synthetic analogues of the mineral and/or compounds isostructural or related to the mineral were also prepared and characterised using IR and Raman spectroscopy, XRD and SEM. Computational calculations were utilised to aid the task of band assignments where possible.

Noticeably the assignment of specific modes is simpler when performed on an isolated arsenite ion such as the case in finnemanite. This is caused by greater suitability of computational methods to isolated ions compared to polymeric ions, which significantly aids band assignment, coupled with the higher symmetry of the arsenite ion in finnemanite (C_s) which allows arsenite vibrations to be more easily distinguished from vibrations of other moieties present in the mineral. Computational methods only facilitated band assignment to an extent in the case of the isolated $[As_2O_5]^{4-}$ ion found in paulmooreite because its symmetry is lowered to C_1 from the calculated ideal symmetry of C_{2v} in which the ion is at an energy minimum. The low site symmetry converts all vibrational modes to *A* modes and thus the experimental Raman spectrum only reflects the crystal symmetry. This necessitated spectral comparison between paulmooreite and other lead arsenites to determine the contribution of terminal and bridging oxygen vibrations. Meta-arsenite and antimonite minerals such as leiteite, trippkeite and schafarzikite were not modelled due to the polymeric nature of the arsenite/antimonite ion. Instead their spectra were compared to minerals with similar building blocks; leiteite was compared to claudetite and schafarzikite and trippkeite were compared to synthetic zinc, manganese, and nickel antimonites.

The structure of finnemanite ($Pb_5(AsO_3)_3Cl$) consists of isolated AsO_3^{3-} pyramids and its Raman spectrum shows $10A_g + 5E_{1g} + 4E_{2g}$ modes out of the possible $10A_g + 7E_{1g} + 11E_{2g}$. Fundamental modes of AsO_3 were assigned to bands at 734 cm^{-1} (A_g - υ_1), 727 (A_g) and 640 cm^{-1} (E_{1g} – υ_3), 375 (A_g) and 358 cm^{-1} (E_{2g} – υ_2), and 247 (A_g) and 207 cm^{-1} (E_{1g} – υ_4).

Paulmooreite ($Pb_2As_2O_5$) consists of dimeric $As_2O_5^{4-}$ units, and shows $11A_g$ and $16B_g$ modes out of the predicted $27A_g$ and $27B_g$. Spectral comparison with synthetic lead arsenites and the calculated Raman spectrum were utilised to aid assignments. Bands at 850 – 700 cm^{-1} correspond to terminal As-O vibrations, whereas stretches and deformations of the bridging As-O occur in 660 – 480 cm^{-1} and 460 – 240 cm^{-1} respectively.

Leiteite ($ZnAs_2O_4$) consists of polymeric AsO_2 chains. In the Raman spectrum $13A_g$ and $8B_g$ modes were observed out of the predicted $21A_g$ and $21B_g$. Bands at 650 – 450 and 380 – 250 cm^{-1} region were assigned to stretches and deformations of bridging As-O-As units respectively, and those in the 850 – 650 cm^{-1} region were assigned to terminal As-O vibrations.

The structure of schafarzikite ($FeSb_2O_4$) and trippkeite consist of polymeric SbO_2 and AsO_2 chains, respectively, however they are not isostructural to leiteite. In the Raman spectrum of schafarzikite $5A_{1g} + 4B_{1g} + 5B_{2g} + 4E_g$ modes were observed out of the predicted $5A_{1g} + 7B_{1g} + 5B_{2g} + 9E_g$. Bands at 708 ($A_{1g}$) and 667 cm^{-1} (A_{1g}) were assigned to terminal Sb-O vibrations, and a group of bands at 616 – 465 cm^{-1} was assigned to various vibrations of the bridging unit. Antimonite deformations were assigned to bands at 352 – 295 cm^{-1}. The corresponding vibrations of trippkeite were 810 and 780 cm^{-1} (terminal stretches), 657 – 496 cm^{-1} (bridging stretches), and 421 – 371 cm^{-1} (deformation).

Spectral calculations of the isolated $[M(H_2O)_6]^{2+}$ and $[Sb(OH)_6]^-$ ions coupled with spectral comparison with mopungite significantly assisted band assignment to the different moieties present in brandholzite and bottinoite, which otherwise would have been complicated by the predicted multitude of low symmetry modes by factor group analysis. The Raman spectra of brandholzite ($Mg[Sb(OH)_6]_2$•$6H_2O$) and bottinoite ($Ni[Sb(OH)_6]_2$•$6H_2O$), and the non-aligned Raman spectrum of mopungite ($Na[Sb(OH)_6]$), are dominated by antimonate symmetric stretches at 630 – 515 cm^{-1} and show many similarities. Antimonate deformations were assigned to bands at 365 – 330 cm^{-1} and 305 – 280 cm^{-1}. Major differences were noted in the OH stretching region which had greater relative intensity in brandholzite and bottionite, and the presence δH_2O near 1620 cm^{-1} as would be expected by the additional presence of the $[M(H_2O)_6]^{+2}$ ion.

A summary of band assignments of each mineral type is presented in Tables 8.1 and 8.2.

Mineral Type	Mineral Name	Raman Wavenumbers (cm^{-1})			
		ν_1	ν_3	ν_2	ν_4
Ortho-arsenite	Finnemanite	734	727, 634	375, 358	247, 207
Pyro-arsenite	Paulmooreite	850 - 700	660 - 480	460 - 240	
Meta-arsenite	Leiteite	850 - 650	650 - 450	380 - 250	
	Trippkeite	810 - 780	657 - 496	421 - 371	
Meta-antimonite	Schafarzikite	708 - 667	616 - 465	352 - 295	

Table 8.1 – Raman wavenumbers of the stretching (ν_1 and ν_3) and deformation (ν_2 and ν_4) modes of the arsenite and antimonite minerals analysed in this study

Mineral Name	Raman Wavenumbers (cm^{-1})			
	ν_1	ν_2	ν_3	ν_4, ν_5
Brandholzite	617	525	630	355 - 282
Bottinoite	618	516	630	361 - 282
Mopungite	625	526, 546	650	361 - 292

Table 8.2 – Raman wavenumbers of the stretching (ν_1-ν_3) and deformation modes (ν_4 and ν_5) of the Sb-O moiety in hydrated antimonate minerals

8.2 DISCUSSION OF FUTURE WORK

Since this study concentrated on natural arsenite and antimonite minerals, future work could possibly involve the analysis of vibrational spectra of ^{18}O

enriched synthetic minerals to further confirm the contributions of terminal and bridging oxygen atoms.

Other possible future work towards the same aim may be the implementation of DFT to calculate the spectra of a series of compounds representing various polymeric arsenite and antimonite species. The number of arsenite or antimonite units in a polymer would differ from one species to another in an effort to determine the effects these changes bring to the vibrational spectra.

It may also be of interest to find other arsenite and antimonite minerals suitable for single crystal study in order to compare and contrast their spectra with the minerals of this study. If no natural specimens are available, further investigation could be conducted into the synthesis of novel minerals by incorporating metal cations into arsenite and antimonite systems, and into their structures and vibrational spectra.

APPENDICES

Acid and normal antimonites and arsenites with miscellaneous formulae				
Mineral Name	**Chemical Composition**	**Crystal System**	**Space Group**	**Z**
Reinerite	$Zn_3(AsO_3)_2$	Orthorhombic	Pbam	4
Versiliaite	$Fe_2Fe_4Sb_6O_{16}S$	Orthorhombic	Pbam	1
Stibivanite	Sb_2VO_5	Orthorhombic	C2/c	4
Schneiderhöhnite	$Fe^{2+}Fe_3{}^{3+}[As_5O_{13}]$	Triclinic	$P\bar{1}$	2
Fetiasite	$(Fe^{3+}, Fe^{2+}, Ti)_3[O_2\|As_2O_5]$	Monoclinic	$P2_1/m$	2
Ludlockite	$PbFe_4{}^{3+}As_{10}{}^{3+}O_{22}$	Triclinic	$P\bar{1}$	4
Trigonite	$Pb_3Mn^{2+}\{HAsO_3\|(AsO_3)_2]$	Monoclinic	Pn	2
Rouseite	$Pb_2Mn^{2+}[AsO_3]2{\cdot}2H_2O$	Triclinic	P1, $P\bar{1}$	1
Asbecasite	$Ca_3(Ti,Sn^{4+})Be_2[(AsO_3)_3\|SiO_4]_2$	Trigonal	P3c	2
Cafarsite	$Ca_8(Ti,Fe,Fe,Mn)_{6-7}(AsO_3)_{12}{\cdot}4H_2O$	Isometric	Pn3	4
Trippkeite	$Cu[As_2O_4]$	Tetragonal	$P4_1/mbc$	4
Schafarzikite	$Fe^{2+}Sb_2{}^{3+}O_4$	Tetragonal	$P\ 4_1/mbc$	4
Leiteite	$Zn[As_2O_4]$	Monoclinic	$P2_1/c$	4
Paulmooreite	$Pb_2[As_2O_5]$	Monoclinic	$P2_1$	4
Apuanite	$Fe^{2+}Fe_4{}^{3+}Sb_4{}^{3+}O_{12}S$	Tetragonal	$P\ 4_1/mbc$	4

Chadwickite	$(UO_2)H(AsO_3)$	Tetragonal	-	14
Basic or halogen-containing antimonites and arsenites with the formula $(AB)_m(XO_3)_pZ_q$				
Mineral Name	**Chemical Composition**	**Crystal System**	**Space Group**	**Z**
Finnemanite	$Pb_5[Cl\|AsO_3)_3]$	Hexagonal	$P6_3$	2
Nanlingite	$CaMg_4[F_2\|AsO_3]_2$	Trigonal	R3m, $R\bar{3}m$	12
Stenhuggarite	$CaFeSbO(AsO_3)_2$	Tetragonal	$I4_1$	16
Freedite	$Pb_{15}(Cu,Fe^{2+})_3[O_7\|Cl_{10}\|(AsO_3)_4]$	Monoclinic	C2/m	4
Magnussonite	$Mn_{10}As_6O_{18}(OH,Cl)_2$	Isometric	I a3d	16
Nealite	$Pb_4Fe^{2+}[Cl_2\|AsO_3]_2\cdot 2H_2O$	Triclinic	$P\bar{1}$	1
UM1984-09-AsO:ClHMn	$Mn_{10}As_6O_{18}(OH)Cl$	Tetragonal	$I4_1/acd$	-
Basic or halogen-containing antimonites and arsenites with miscellaneous formulae				
Mineral Name	**Chemical Composition**	**Crystal System**	**Space Group**	**Z**
Ecdemite	$Pb_6[As_2O_7\|Cl_4]$	Tetragonal	Unk	8
Heliophyllite	$Pb_3AsO_{4-n}Cl_{2n+1}$	Orthorhombic	Unk	8
Tomichite	$(V,Fe)_4Ti_3AsO_{13}OH$	Monoclinic	A2/m	2
Derbylite	$(Fe,Fe,Ti)_7SbO_{13}(OH)$	Monoclinic	$P2_1/m$	2
Hemloite	$(As,Sb)_2(Ti,V,Fe,Al)_{12}O_{23}(OH)$	Triclinic	$P\bar{1}$	2
Gebhardite	$Pb_8[O\|Cl_6\|(As_2O_5)_2]$	Monoclinic	$P2_1/c$	4

Manganarsite	$Mn_3[(OH)_4\|As_2O_4]$	Trigonal	$P3_1 2$	4
Armagite	$Mn^{2+}_{26}[CO_3\|(HAsO_3)_4\|(AsO_3)_{14}]$	Trigonal	$P\bar{3}$	1
Dixenite	$CuMn_{14}^{2+}Fe^{2+}[(OH)_6\|(AsO_3)_5\|AsO_4\|(SiO_4)_2]$	Trigonal	R 3	3
Seelite	$Mg(UO_2)(AsO_3)_{0.7}(AsO_4)_{0.3}.7H_2O$	Monoclinic	C 2/m	3
Graeserite	$(Fe^{3+},Ti)_4Ti_3AsO_{13}(OH)$	Monoclinic	A2/m	2
Arakiite	$(Zn,Mn^{2+})(Mn^{2+},Mg)_{12}(Fe^{3+},Al)_2(AsO_3)(AsO_4)_2(OH)_{23}$	Monoclinic	Cc	4
Antimony hydroxides and oxides containing hydroxyl with $(OH)_3$ or $(OH)_6$ groups				
Mineral Name	**Chemical Composition**	**Crystal System**	**Space Group**	**Z**
Mopungite	$NaSb(OH)_6$	Tetragonal	$P4_1/n$	4
Brandholzite	$Mg[Sb(OH)_6]_2•6H_2O$	Trigonal	P3	6
Bottinoite	$Ni[Sb(OH)_6]_2•6H_2O$	Trigonal	P3	6

Appendix 1 – Details of arsenite, antimonite, and hydroxyantimonate minerals sorted by new Dana classification

Solid As_4O_6				Gas-phase As_4O_6	Calculated	
IR [16]	**Raman [16]**	**IR [46]**	**Raman [17]**	**Raman [47]**	**IR [39]**	**Raman (gas-phase) [39]**
845 (medium, shoulder)	830					
800 (very strong)	785	808	783		810	
	556		561	556		575
490 (weak, shoulder)	492			492	493	493
480 (strong)		482	473			
349 (very strong)	381	346	372	381	391	372
270 (medium)	253	258	269	253	258	

Appendix 2 – IR and Raman band positions for arsenolite

Solid senarmontite		Solid valentinite		Gaseous Sb_4O_6	Calculated senarmontite		Calculated valentinite	
IR [56]	**Raman [47][55]**	**IR [56]**	**Raman [55]**	**IR [58]**	**IR [56]**	**Raman [56]**	**IR [56]**	**Raman [56]**
				785				
740	717	740			765			
675			690				672	
							663	663
			602				600 – 550	600 – 550
			502					
		585			574		560 – 501	
		540						
		488					519 – 489	519 – 489
	452	455	449		465		460 – 450	460 – 450
				415	409			
	376					394		
	354						344	
			294	292				316 – 320
	256		269		282	280		
			223					
	193		194					
			140	175	179	179	188	
	121					126		
			103			109		
	87							163 – 84
			71					

Appendix 3 – IR and Raman band positions for valentinite, senarmontite, and gaseous Sb_4O_6

$MnSb_2O_4$		$NiSb_2O_4$	
Raman	**IR**	**Raman**	**IR**
			720
670		685	650
620	647	638	620
		585	
547	569	535	
527			
474	495	486	500
465			
		421	
399	385		400
350		360	360
345	340		
292		309	
255	250	244	260
221			220
215			
189		189	
156		157	
		132	
124		119	
105			
		67	
52		56	
47			

Appendix 4 – IR and Raman band positions for synthetic $MnSb_2O_4$ and $NiSb_2O_4$

REFERENCES

[1] Greenwood, N. N., Earnshaw, A. (1997) *Chemistry of the Elements*, Pergamon, Oxford,UK

[2] Smith, J.D. (1973) *The Chemistry of Arsenic, Antimony, and Bismuth*, Pergamon, Oxford, UK

[3] Parkes, G.D. (1958) *Mellor's Modern Inorganic Chemistry,* Longmans, Green and Co., Bristol, UK

[4] Emmerling, F. and Röhr, C. (2003) Die neuen oxoarsenate(III) $AAsO_2$ (A = Na, K, Rb) und $Cs_3As_5O_9$. Darstellung, kristallstrukturen und Raman-spektren. *Z. Naturforsch.*, 58B: 620 – 626

[5] Pertlik, F. (1988) The single chain arsenites $Pb(AsO_2)Cl$ and $Pb_2(AsO_2)_3Cl$. Preparation and structure investigation. *Z. Kristallographie*, 184: 191 – 201

[6] Xiao, F., Zheng, Y., Wang, Y., Jian, H., Li, C., Xu, W. and Ma, Y. (2008) Preparation of copper arsenite and its application in purification of copper electrolyte. *Trans. Nonferrous Met. Soc. China*, 18: 474 – 479

[7] Pertlik, F. (1977) Zur synthese von kristallen von $CuAs_2O_4$ (trippkeit) und $Cu_2As_3O_6CH_3COO$ (eine komponente des farbpigments Schweinfurter Grün). *Z. anorg. Allg. Chem.*, 436: 201 – 206

[8] Curtin, L. P. (1927) Experiments in wood preservation. II – Arsenites of copper and zinc. *Industrial and Engineering Chemistry*, 19(9): 993 – 999

[9] Avery, S. (1906) The constitutionof Paris Green and its homologues. *J. Am. Chem. Soc.*, 28: 1155 – 1164

[10] Subramanian, A., Vasudevan, T., Gnagadharan, R. and Raghavan, M. (2003) Solid state synthesis of lithium meta arsenate. *US Patent Application 20030185745*

[11] Hirschle, C. and Röhr, C. (2000) Alkalimetall-oxoantimonate: synthesen, kristallstrukturen und schwingungsspektren von $ASbO_2$ (A = K, Rb), $A_4Sb_2O_5$ (A = K, Rb, Cs) und Cs_3SbO_4. *Z. Anorg. Allg. Chem.*, 626: 1305 – 1312

[12] Stair, P. C., Xiong, G., Sullivan, V. S., Zajac, G. W., Trail, S. S., Kaduk, J. A., Golab, J. T. and Brazdil, J. F. (2005) Effect of titanium substitution on the

structure of $VSbO_4$ catalysts for propane ammoxidation. *J. Catalysis*, 230: 317 – 326

[13] Dorhout, P. K., So, W., LaCour, A. and Aliev, V. O. (2004) Synthesis and characterization of a new quarternary lanthanum oxythioantimonite: $La_6Sb_4O_{12}S_3$. *J. Alloys and Compounds*, 374: 234 – 239

[14] Albrecht-Schmitt, T. E., Sykora, R. E., King, J. E. and Illies, A. J. (2004) Hydrothermal synthesis, structure, and catalytic properties of $UO_2Sb_2O_4$. *J. Solid State Chem.*, 177: 1717 – 1722

[15] Chater, R., Gavarri, J. R. and Genet, F. (1986) Composes isomorphes $MeX_2O_4E_2$. I. Etude vibrationelle de $MnSb_2O_4$ entre 4 et 300 K: champ de force et tenseur élastique. *J. Solid State Chem.*, 63: 295 – 307

[16] Szymanski, H. A., Marabella, L., Hoke, J. and Harter, J. (1968) Infrared and Raman studies of arsenic compounds. *App. Spectrosc.*, 22(4): 297 – 304

[17] Loehr, T. M. and Plane, R. A. (1968) Raman spectra and structures of arsenious acid and arsenites in aqueous solution. *Inorg. Chem.*, 7(9): 1708 – 1714

[18] Tossell, J. A. (1997) Theoretical studies on arsenic oxide and hydroxide species in minerals and in aqueous solution. *Geochim. et Cosmochim. Acta*, 61(8): 1613 – 1623

[19] Tossell, J. A. and Zimmermann, M. D. (2008) Calculation of the structures, stabilities, and vibrational spectra of arsenites, thioarsenites and thioarsenates in aqueous solution. *Geochim. et Cosmochim. Acta*, 72: 5232 – 5242

[20] Wood, S. A., Tait, C. D. and Janecky, D. R. (2002) A Raman spectroscopic study of arsenite and thioarsenite species in aqueous solution at 25° C. *Geochem. Trans.*, 3(4): 31 – 39

[21] Gout, R., Pokrovski, G., Schott, J. and Zwick, A. (1997) Raman spectroscopic study of arsenic speciation in aqueous solutions up to 275° C. *J. Raman. Spectrosc.*, 28: 725 – 730

[22] Pokrovski, G., Gout, R., Schott, J., Zotov, A. and Harrichoury, J. (1996) Thermodynamic properties and stoichiometry of As(III) hydroxide complexes at hydrothermal conditions. *Geochim. et Cosmochim. Acta*, 60(5): 737 – 749

[23] Ghose, S., Boving, P., LaChappele, W. A. and Wan, C. (1977) Reinerite, $Zn_3(AsO_3)_2$: an arsenite with a novel type of zinc-tetrahedral double chain. *Amer. Min.*, 62: 1129 – 1134

[24] Pertlik, F. and Effenberger, H. (1979) Die Kristallstruktur des Finnemanits, $Pb_5Cl(AsO_3)_3$, mit einem Vergleich zum Strukturtyp des Chloroapatits, $Ca_5Cl(PO_4)_3$. *Tschermaks Min. Petr. Mitt.*, 26: 95 – 107

[25] Dunn, P. J., Peacor, D. R. and Darko Sturman, B. (1979) Paulmooreite, a new lead arsenite mineral from Langban, Sweden. *Amer. Min.*, 64: 352 – 354

[26] Ondrus, P., Skala, R., Cisarova, I., Veselovsky, F., Fryda, J. and Cejka, J. (2002) Description and crystal structure of vajdakite, $[(Mo^{6+}O_2)_2(H_2O)_2As^{3+}{}_2O_5].H_2O$ – A new mineral from Jachymov, Czech Republic. *Amer. Min.*, 87: 983 – 990

[27] Ghose, S., Sen Gupta, P. K. and Schlemper, E. O. (1987) Leiteite, $ZnAs_2O_4$: A novel type of tetrahedral layer structure with arsenite chains. *Amer. Min.*, 72: 629 – 632

[28] Pertlik, F. (1975) Verfeinerung der Kristallstruktur von synthetischem Trippkeit, $CuAs_2O_4$. *Tschermaks Min. Petr. Mitt.*, 22: 211 - 217

[29] Mellini, M. and Merlino, S. (1979) Versiliaite and apuanite: derivative s tructures related to schafarzikite. *Amer. Min.*, 64: 1235 – 1242

[30] Farmer, V. C. (1974) *The Infrared Spectra of Minerals*, Mineralogical Society, London, UK

[31] Husson, E., Repelin, Y. and Brusset, H. (1979) Spectres de vibration et calcul du champ de force des antimoniates et des tantalates de structure trirutile. *Spectrochim. Acta*, 35A: 1177 – 1187

[32] White, W. B., (1967) Application of IR spectroscopy to order-disorder problems in simple ionic solids. *Mater. Res. Bull.*, 2: 381 – 394

[33] Baran, E. J. and Botto, I. L. (1981) Espectro vibracional del $NaSbO_3$. *Anales Asoc. Quim. Argentina*, 69: 283 – 291

[34] Siebert, H. (1959) Ultrarotspektren von tellursäuren, telluraten und antimonaten. *Z. Anorg. Allg. Chem.*, 301: 161 – 170

[35] Vandenborre, M. T., Husson, E. and Fourquet, J. L. (1982) Spectres vibrationnels et champ de force de divers composes de formule $A_2B_2O_7$ et $A_2B_2O_6$ de structure pyrochlore. *Spectrochim. Acta*, 38A(9): 997 – 1003

[36] Franck, R. (1973) Spectres d'absorption infrarouge de quelques hydroxyantimoniates. *Rev. Chim. Miner.*, 10(6): 795 – 810

[37] Balicheva, T. G. and Roi, N. I. (1971) IR spectra and structure of several crystalline hexahydroxyantimonates and their deuteron analogs. J. Struct. Chem., 12(3): 415 – 422

[38] Norman, N. C. (1998) *Chemistry of Arsenic, Antimony, and Bismuth*, Blackie, London, UK

[39] Jensen, J. O., Gilliam, S. J., Banerjee, A., Zeroka, D., Kirkby, S. J. and Merrow, C. N. (2003) A theoretical study of As_4O_6: vibrational analysis, infrared and Raman spectra. *Theochem.*, 664 – 665: 145 – 146

[40] Stranski, I. N., Plieth, K. and Zoll, I. (1958) The solution, solubility, and transitions of arsenolite and claudetite in water and aqueous solutions. *Zeit. Electrochem.*, 62: 366 – 372

[41] Menary, J. W. (1958) The crystal structure of sodium polymetaarsenite $(NaAsO_2)_x$. *Acta. Cryst.*, 11: 742 – 743

[42] Lee, C. and Harrison, W. T. A. (2004) The catena-arsenite chain anion, $[AsO_2]_n^{n-}$: $(H_3NCH_2CH_2NH_3)0.5[AsO_2]$ and $NaAsO_2$ (revisited) *Acta Cryst. Section C*, 60: 215 – 218

[43] Asai, T. (1975) Refinement of the crystal structure of sodium hexahydroxoantimonate(V), $NaSb(OH)_6$. *Bull. Chem. Soc. Jpn.*, 48(10): 2677 - 2679

[44] Friedrich, A., Wildner, M., Tillmanns, E. and Merz, P. L. (2000) Crystal chemistry of the new mineral brandholzite, $Mg(H_2O)_6[Sb(OH)_6]_2$, and of the synthetic analogues $M^{2+}(H_2O)_6[Sb(OH)_6]_2$ (M^{2+}=Mg, Co). *Amer. Min.*, 85: 593 – 599

[45] Wang, A., Han, J., Guo, L., Yu, J. and Zeng, P. (1994) Database of standard Raman spectra of minerals and related inorganic crystals. *App. Spectrosc.*, 48(8): 959 – 968

[46] Lezal, D. and Konak, K. (1995) The characterization of the infrared absorption spectra of the vitreous, cubic and monoclinic modification of As_2O_3. *J. Non-Crystal. Solids*, 192 – 193: 187 – 190

[47] Beattie, I. R., Livingston, K. M. S., Ozin, G. A. and Reynolds, D. J. (1970) Single-crystal Raman spectra of arsenolite (As_4O_6) and senarmontite (Sb_4O_6). The gas-phase Raman spectra of P_4O_6, P_4O_{10}, and As_4O_6. *J. Chem. Soc.*, A: 449 – 451

[48] Gilliam, S. J., Merrow, C. N., Kirkby, S. J., Jensen, J. O., Zeroka, D. and Banerjee, A. (2003) Raman spectroscopy of arsenolite: crystalline cubic As_4O_6. *J. Solid State Chem*, 173: 54

[49] Brumbach, S. B. and Rosenblatt, G. M. (1972) In-cavity laser Raman spectroscopy of vapors at elevated temperatures. As_4 and As_4O_6. *J. Chem. Phys.*, 56: 3110 – 3117

[50] Grzechnik, A. (1999) Compressibility and vibrational modes in solid As_4O_6. *J. Solid State Chem.*, 144: 416 – 422

[51] Flynn, E. J., Solin, S. A. and Papatheodorou, G. N. (1976) Vibrational excitations of As_2O_3. II. Crystalline phases. Phys. Rev. B, 13(4): 1752 – 1758

[52] Mercier, R. and Sourisseau, C. (1978) Spectres de vibration et calcul du champ de force de la Claudetite I, $(As_2O_3)_n$. *Spectrochim. Acta*, 34A: 337 – 342

[53] Akinfiev, N. N., Zotov, A. and Nikonorov, A. (1993) Thermodynamic analysis of equilibria arsenic(III)-sulfur(II)-and oxygen-hydrogen. *Geochem. Int.*, 29: 109 – 121

[54] Kloprogge, J. T. and Frost, R. L. (1999) Raman microscopy study of cafarsite. *App. Spectrosc.*, 53(7): 874 – 88

[55] Cody, C. A., DiCarlo, L. and Darlington, R. K. (1979) Vibrational and thermal study of antimony oxides. *Inorg. Chem.*, 18(6): 1572 – 1576

[56] Mestl, G., Ruiz, P., Delmon, B. and Knözinger, H. (1994) Sb_2O_3/Sb_2O_4 in reducing/oxidizing environments: an in situ Raman spectroscopic study. *J. Phys. Chem.*, 98: 11276 – 11282

[57] Voit, E. I., Panasenko, A. E. and Zemnukhova, L. A. (2009) Vibrational spectroscopic and quantum chemical study of antimony(III) oxide. *J .Struct.l Chem.*, 50(1): 60 – 66

[58] Konings, R. J. M., Booij, A. S. and Cordfunke, E. H. P. (1993) The infrared spectrum of gaseous antimony oxide (Sb_4O_6). *Chem. Phys. Lett.*, 210(4-6): 380 – 383

[59] Sourisseau, C. and Mercier, R. (1978) Vibrational spectra and calculation of the force field of arsenolite, senarmontite, and phosphorus oxide (P_4O_6). *Spectrochim. Acta A*, 34A(2): 173 – 178

[60] Gilliam, S. J., Jensen, J. O., Banerjee, A., Zeroka, D., Kirkby, S. J. and Merrow, C. N. (2004) *Spectrochim. Acta A.*, 60: 425 – 434

[61] Zotov, A. V., Shikina, N. D. and Akinfiev, N. N. (2003) Thermodynamic properties of the Sb(III) hydroxide complex $Sb(OH)_{3(aq)}$ at hydrothermal conditions. *Geochim. et Cosmochim. Acta*, 67(10): 1821 – 1836

[62] Casas, J. M., Crisóstomo, G. and Cifuentes, L. (2004) Antimony solubility and speciation in aqueous sulphuric acid solutions at 298 K. *The Canadian Journal of Chemical Engineering*, 82: 175 – 183

[63] Tossell, J. A. (1994) The speciation of antimony in sulfidic solutions: a theoretical study. *Geochim. et Cosmochim. Acta*, 58(23): 5093 – 5104

[64] Sejkora, J., Ozdin, D., Vitalos, J., Tucek, P., Cejka, J. and Duda, R. (2007) Schafarzikite from the type locality Pernek (Malé Karpaty mountains, Slovak Republic) revisited. *Eur. J. Mineral*, 19: 419 – 427

[65] Schrewelius, N. (1938) Röntgenuntersuchung der Verbindungen $NaSb(OH)_6$, $NaSbF_6$, $NaSbO_3$ und gleichartiger Stoffe. *Z. Anorg. Allg. Chem.*, 238: 241 – 254

[66] Bhatnagar, C. S. and Govind, K. (1966) Electrometric studies on the formation of alkali arsenites. *Z. Naturforschg.*, 21B: 190 – 191

[67] Pertlik, F. and Schnorrer, G. (1993) A re-appraisal of the chemical formula of nealite, $Pb_4Fe(AsO_3)_2Cl_4.2H_2O$, on the basis of a crystal structure determination. *Mineralogy and Petrology*, 48: 193 – 200

[68] Giuseppetti, G., Mazzi, F. and Tadini, C. (1993) The crystal structure of nealite: $Pb_4Fe(AsO_3)_2Cl_4.2H_2O$. *Neues Jahrbuch fur Mineralogie*, 1993: 278 – 288

[69] Baikie, T., Ferraris, C., Klooster, W. T., Madhavi, S., Pramana, S. S., Pring, A., Schmidt, G. and White, T. J. (2008) Crystal chemistry of mimetite, $Pb_{10}(AsO_4)6Cl_{1.}48O_{0.26}$, and finnemanite, $Pb_{10}(AsO_3)_6Cl_2$. *Acta Cryst.*, B64: 34 – 41

[70] Levitt, S. R. and Condrate, R. A. (1970) The vibrational spectra of lead apatites. *Amer. Min.*, 55: 1562 – 1575

[71] Adams, D. M. and Gardner, I. R. (1974) Single-crystal vibrational spectra of apatite, vanadinite, and mimetite. *J. Chem. Soc. Dalton*, 14: 1505 – 1509

[72] Frisch M. J. , et al. (2004) *Gaussian 03, Revision C.02*, Gaussian, Inc., Wallingford, CT

[73] Nakamoto, K. (1997) *Infrared and Raman spectra of inorganic and coordination compounds. Part A: Theory and applications in inorganic chemistry*. John Wiley & Sons, Inc. Publications, New Jersey, USA

[74] Ross, S. D. (1972) *Inorganic infrared and Raman spectra*. McGraw Hill publisher, London, UK

[75] Araki, T., Moore, P. B. and Brunton, G. D. (1980) Type crystal structure of paulmooreite, $Pb_2[As_2O_5]$: dimeric arsenite groups. *Amer. Min.*, 65: 340 – 345

[76] Klaska, R. and Gebert, W. (1982) Polytypie und struktur von gebhardit – $Pb_8OCl_6(As_2O_5)_2$. *Z. Kristallographie*. 159: 75 – 76

[77] Dinterer, F., Effenberger, H., Kugler, A., Pertlik, F., Spindler, P. and Wildner, M. (1988) Structure of lead (II) arsenate (III). *Acta Cryst.*, C44: 2043 – 2045

[78] Cejka, J., Bahfenne, S., Frost, R. L. and Sejkora, J. (2010) Raman spectroscopic study of the arsenite mineral vajdakite $[(Mo^{6+}O_2)_2(H_2O)_2As^{3+}{}_2O_5].H_2O$. *J. Raman Spectrosc.*, 41(1): 74 – 77

[79] Fischer, R. and Pertlik, F. (1975) Verfeinuring der Kristallstruktur des Schafarzikits $FeSb_2O_4$. *Tschermaks Min. Petr. Mitt. 22:* 236-241

[80] Curtin, L. P. (1933) *US Patent Application 1924065*

[81] Klein, C., Hurlbut Jr, C. S. (1993) *Manual of Mineralogy*. John Wiley & Sons, Inc. Toronto, Canada

[82] Cesbron, F. P., Erd, R. C., Czamansik, G. K., and Vachey, H. (1977) *Mineralogical Record, Tsumeb issue*: 95 – 97

[83] Lucovsky, G. and Galeener, F. L. (1980) Local structure and vibrational spectra of v-As_2O_3. *J. Non-Cryst. Solids*, 37: 53 – 70

[84] Zemann, J. (1951) Formel und Kristallstruktur des Schafarzikits. *Tschermaks Min. Petr. Mitt.*, 2: 166 – 175.

[85] Zemann, J. (1951) Formel und Kristallstruktur des Trippkeits. *Tschermaks Min. Petr. Mitt.*, 2: 417 – 423.

[86] Mellini, M., Merlino, S. and Orlandi, P. (1979) Versiliaite and apuanite, two new mi nerals from the Apuan Alps, Italy. *Amer. Min.*, 64: 1230 – 1234.

[87] Bahfenne, S. and Frost, R. L. (2010) Raman spectroscopic study of the antimonate mineral romeite. *Spectrochim. Acta.*, A75: 637 – 639

[88] Bahfenne, S.and Frost, *R. L.* (2009) Vibrational spectroscopic study of the antimonate mineral bindheimite $Pb_2Sb_2O_6(O,OH)$. *Spectrochim. Acta.* , A74: 100 – 103

[89] Frost, R. L., Bahfenne, S. and Keeffe, E. J. (2009) Raman spectroscopic study of the antimonate mineral $Mg[Sb_2(OH)_{12}].6H_2O$. *J. Raman Spectrosc.*, 40: 1907 – 1910

[90] Friedrich, A., Mazzi, F., Wildner, M. and Ekkehart, T. (2003) Isotypism of $Co(H_2O)_6[Sb(OH)_6]_2$ with brandholzite and bottinoite. *Amer. Min.*, 88: 462 – 463

[91] Bonazzi, P. and Mazzi, F. (1996) Bottinoite, $Ni(H_2O)_6[Sb(OH)_6]_2$; crystal structure, twinning, and hydrogen-bond model. *Amer. Min.*, 81:1494 – 1500

[92] Bonazzi, P., Menchetti, S., Caneschi, A. and Magnelli, S. (1992) Bottinoite , a new mineral from the Bottino mine, Alpi Apuane, Italy. *Amer. Min.*, 77*:* 1301 - 1304

[93] Check, C.E., Faust, T. O., Bailey, J. M., Wright, B. J., Gilbert, T. M. and Sunderlin, L. S. (2001) *J. Phys. Chem. A*, 105: 8111 – 8116